Bosons de Tonks et Girardeau dans un anneau à une dimension

Christoph Schenke

UNIVERSITÉ DE GRENOBLE

THÈSE

Pour obtenir le grade de

DOCTEUR DE L'UNIVERSITÉ DE GRENOBLE

Spécialité : **Physique Théorique**

Arrêté ministériel : 7 Août 2006

Présentée par

Christoph SCHENKE

Thèse dirigée par **Frank W. J. Hekking**
et codirigée par **Anna Minguzzi**

préparée au sein du **Laboratoire de Physique et Modélisation des Milieux Condensés**
dans **l'École Doctorale de Physique**

Bosons de Tonks et Girardeau dans un anneau à une dimension

Thèse soutenue publiquement le **29 Octobre 2012**,
devant le jury composé de :

Mr. Alain Joye
Professeur, Université Joseph Fourier, Grenoble, Président
Mr. Hrvoje Buljan
Professeur, Université de Zagreb, Croatie, Rapporteur
Mr. Vincent Lorent
Professeur, Université Paris XIII, Paris, Rapporteur
Mme. Roberta Citro
Docteur, Université de Salerne, Italie, Examinatrice
Mr. Frank W. J. Hekking
Professeur, Université Joseph Fourier, Grenoble, Directeur de thèse
Mme. Anna Minguzzi
Docteur, LPMMC/CNRS, Grenoble, Co-Directeur de thèse

Contents

I Introduction

In order to exactly determine the orientation of objects, such as airplanes or ships, etc., reliable navigational systems are needed. These systems make use of very accurate measurements of the precession of the concerned object, carried out by so-called gyroscopes. The first gyroscope was invented by the german physicist and mathematician Johann Gottlieb Friedrich von Bohnenberger in the year 1817 and was further developed by Léon Foucault in 1852 who finally gave it the name gyroscope. The first gyroscopes were comprised of a quickly spinning wheel framed in two rings. The spinning wheel's axis was mounted in the inner ring and the inner ring is mounted on an outer ring which is mounted in the gyroscope frame, see Fig.I.1 a). Given this set-up the outer ring was free to rotate around its own axis, the inner ring was free to rotate around two axes (its own axis and the axis of the outer ring which is perpendicular to it) and the central (spinning) wheel could rotate around all three axes, having thus all rotational degrees of freedom. By the conservation of angular momentum (of the central wheel) in the inertial system an applied force on the gyroscope can be measured by the resulting perpendicular rotation (angle α in Fig.I.1 a)). Once rotated perpendicular there will be a constant force due to the earth's gravitational field leading to precession, see Fig.I.1 a). Nowadays high-precision measurement devices of rotation make use of ring lasers or fiber optics where, in contrast to their mechanical counterparts, no moving parts are involved in the measurement process. A typical set-up is the Sagnac geometry [1] where counterpropagating photons on a ring are superimposed, see Fig.I.1 b). Upon rotation of the whole instrument, photons originating from the different paths pick up different phases that can be seen in the interference pattern of the superposition. The displacement of the interference pattern due to the relative phase ϕ_{Sag} is proportional to the angular frequency of the rotation and may directly be related to the force applied on the gyroscope. Since the measurement of this relative phase is based on the detection of discrete photon packages (one input port interferometer) the sensitivity is limited by shot noise and scales $1/\sqrt{N}$ where N is the number of measured photons[2].

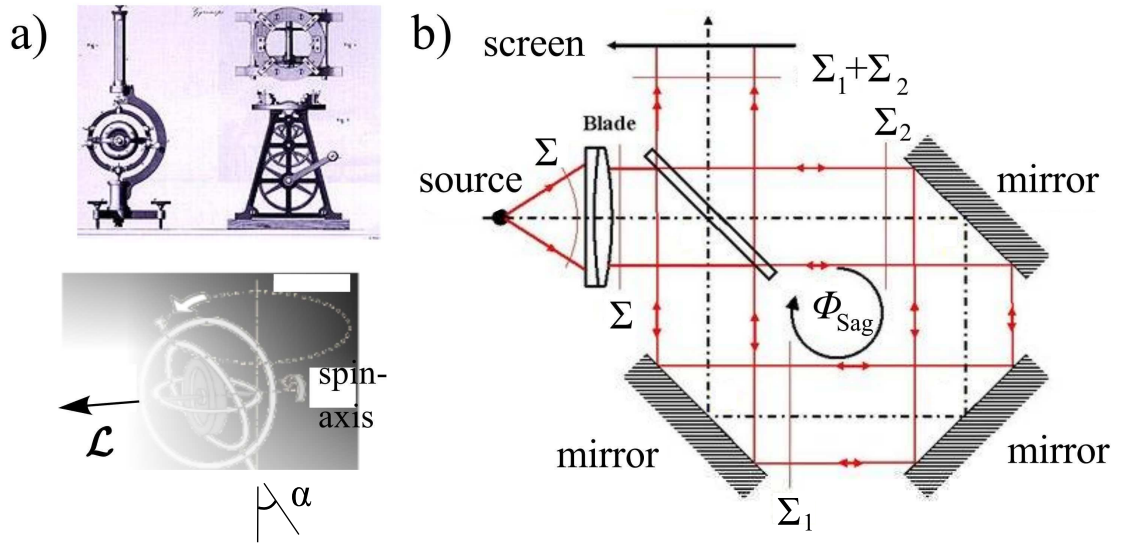

Figure I.1: a) Drawing of the Foucault gyroscope found at the web page of the German museum [3] and a schematic drawing explaining the working mechanism of the gyroscope. From [4]. b) Schematic drawing of the Sagnac geometry. From [5].

The prospect of high-precision measurement devices that can go beyond the shot noise limit, set-ups making use of entangled particles have raised increasing attention in recent years. The exploitation of entangled or squeezed states of particles (correlated two-input port interferometer) allows to reach the ultimate sensitivity, i.e. the quantum mechanically possible sensitivity, limited by the Heisenberg uncertainty relation only, for the relative phase, the so-called Heisenberg limit which scales like $1/N$, see chapter V. This thesis can be seen as one of the building blocks for a Sagnac interferometer using massive particles, i.e. ultra cold atoms. As analyzed in Ref. [6], the use of atoms instead of photons is favorable since the phase signal that is measured is proportional to the mass m of the measured particles,

$$\phi_{Sag} = \frac{2Am\Omega_g}{\hbar} \ ,$$

where A is the gyroscope area and Ω_g the angular velocity about the center of the gyroscope. This mass-enhancement factor can be seen in table 1 of Ref. [2].
One very promising proposition for the realization of such a "next generation" gyroscope is a one-dimensional (1D) strongly correlated atomic gas confined to a ring geometry. Creating a superposition of rotating and non-rotating states via a moving barrier potential along the ring circumference the interferometer will allow for ultra pre-

cise measurements, only limited by the Heisenberg limit while profiting from the mass enhancement factor. Additionally, due to the strong interactions between the particles, this set-up will be very robust against one of the dominating decoherence processes, i.e. two- and three-body losses which are always problematic when dealing with entangled atoms. As will be detailed in Sec.II.3.2, experimental progress in recent years has made the creation of the Tonks-Girardeau (TG) gas of impenetrable bosons (infinitely strong interactions between the particles) in a 1D trap possible [7, 8]. More recently, the possibility to set a three dimensional Bose Einstein condensate on a toroidal trap into rotation has been demonstrated [9], see Sec.II.3.1. In view of this recent progress the realization of the 1D TG gas on a ring trap, seems to be within reach. The case of infinitely strong interactions between the particles has the further advantage that they are described by an exactly solvable Hamiltonian. Thus it allows for the calculation of all observables of interest and therefore is not only of interest regarding technical applications but also allows to answer fundamental questions of quantum physics such as, e.g. 1D superfluidity. This thesis is aimed to answer many of these questions and contributes to the understanding of the physics of strongly interacting 1D quantum gases. Hence it can be seen as one of the necessary steps for the construction of a high precision gyroscope.

This thesis is organized as follows. The **second chapter** provides a general introduction to the physics of 1D ultracold atomic gases. The basic features of 1D non-interacting bosons under the influence of rotation are explained and a connection to Bloch's theory is made. We introduce the reader to the peculiarities of one dimension and point out the differences between weak and strong interactions. Two standard methods used to describe the strongly interacting regime, the Lieb-Liniger model and the Bose-Fermi mapping, are explained in detail. In addition we provide an overview of state of the art experiments concerning bosons confined either in 1D or on ring traps (both features together have not yet been realized). Finally we review some related theoretical works, treating interacting bosons confined to a 1D ring under the influence of rotation, hence providing the direct context of our own work.

In the **third chapter** we present the system, represented by its Hamiltonian, for our theoretical investigation. It is described by bosons confined to a 1D ring under the influence of a rotating delta-barrier potential. Two regimes of interaction strength are treated: a) the non-interacting case of the ideal Bose gas and b) the strongly interacting regime of impenetrable bosons (Tonks-Girardeau limit). We provide both an exact

solution and a perturbative solution (in the weak barrier limit) for the dynamical evolution for a sudden set into motion of the barrier potential (out-of-equilibrium drive). Moreover, we check the validity of the delta-barrier model employed for the calculations by comparing the results to those obtained for a more realistic square-barrier potential.
In the **fourth chapter** we investigate the superfluid properties of the TG gas and the ideal Bose gas, respectively. We consider both an adiabatic switching-on of the barrier motion and the out-of-equilibrium drive. In order to make quantitative statements about the superfluid behavior we calculate the time averaged integrated particle current induced by the rotating barrier and its fluctuations. We find that typically the fluctuations are smaller than the average current (for non-zero current), yielding a large signal to noise ratio. We find a superfluid response of the bosons below a critical velocity, in agreement with the value found for the weakly interacting Bose gas [10]. In order to further investigate the superfluid properties of the ideal Bose gas/TG gas we calculate the drag force acting on the barrier. The study of the drag force quantifies dynamical, complementary, aspects of superfluidity and confirms the critical velocity found by investigating the spatially integrated time-averaged particle current.
In the **fifth chapter** we investigate the dynamical properties of the TG gas upon applying the out-of-equilibrium drive. We calculate the time-dependent spatially integrated particle current. We find that at specific times, the state of the system is a macroscopic superposition of two current states with velocity components zero and twice the barrier velocity. In order to study the nature of the superposition state and its degree of entanglement we calculate the one-body density matrix which gives access to the momentum distribution and Wigner quasiprobability distribution function. It is found that the two components of the superposition can be described in terms of two Fermi spheres of the mapped Fermi gas. Finally, we simulate the time-of-flight signal, the standard probe used in experiments which allows to detect this strongly entangled many particle state.
In the **sixth chapter** we summarize our findings and provide an outlook towards open questions and perspectives. Most of the results presented in this thesis have been published in the following works

List of publications

- C. Schenke, A. Minguzzi and F. W. J. Hekking, *Nonadiabatic creation of macroscopic superpositions with strongly correlated one-dimensional bosons in a ring trap*, Phys. Rev. A **84** 053636 (2011)
- C. Schenke, A. Minguzzi and F. W. J. Hekking, *Probing superfluidity of a mesoscopic Tonks-Girardeau gas*, Phys. Rev. A **85** 053627 (2012)

Résumé de la Thèse

Cette thèse comprend une analyse d'un système de N bosons de masse m, à une dimension (1D). Vue des efforts expérimentaux récents et de la perspective d'étudier plusieurs effets quantiques intéressants, nous choisissons une géométrie circulaire avec une circonférence L. Un potentiel extérieur dépendant du temps nous permet d'introduire un mécanisme qui change l'état du moment angulaire des bosons. Ce potentiel est de la forme d'une fonction delta de Dirac qui se déplace le long de l'anneau à une vitesse v et la force de ce potentiel vaut U_0: $U_{ext}(x_l, t) = U_0\delta(x_l - vt)$. Il peut être vu comme une barrière qui met les bosons en rotation. Les interactions entre les bosons sont des interactions de contact avec une force qui vaut g_{1D}, décrites dans le modèle de Lieb et Liniger [11]. Puisque le potentiel extérieur ne garde pas la symétrie de translation de L'Hamiltonien du système

$$\mathcal{H}_B = \sum_{l=1}^{N} \left[-\frac{\hbar^2}{2m}\frac{\partial^2}{\partial x_l^2} + U_{ext}(x_l, t) + g_{1D}\sum_{j<l}\delta(x_j - x_l) \right] , \tag{1.0.1}$$

l'équation de Schrödinger n'est pas résoluble de manière exacte en utilisant un Ansatz de Bethe. Cependant, dans les limites des bosons libres ($g_{1D} = 0$) et des bosons impénétrables de Tonks et Girardeau ($g_{1D} = \infty$) des méthodes alternatives existent pour trouver une solution exacte. Le but de cette thèse est de résoudre l'équation de Schrödinger avec l'Hamiltonien (1.0.1) dans ces cas limites. La solution nous permet d'accéder aux observables intéressantes concernant les propriétés superfluides des bosons libres et du gaz de Tonks. De plus, nous étudions la nature de l'état quantique du gaz de Tonks. La thèse est construit de manière suivante.

Dans le **deuxième chapitre**, nous présentons le cadre de notre analyse du gaz de Bose à une dimension. Nous expliquons l'effet de rotation, représenté par un flux de Coriolis pénétrant l'anneau, et nous soulignons son équivalence avec le potentiel vecteur $\mathbf{A}$, avec le champs magnétique $\mathbf{B} = \nabla \times \mathbf{A}$, dans le modèle d'Aharonov et Bohm. Après avoir expliqué le comportement particulier des bosons à une dimension (l'absence d'ordre à longue porté non-diagonal dans la matrice densité et la longueur de diffusion effective), nous nous focalisons sur les modèles exactement résolubles de Lieb et Liniger [11, 12] et de Girardeau [13, 14]. Ensuite nous présentons l'état de l'art et les progrès récents des groupes expérimentaux concernant les régimes d'interaction entre les particules [7, 8] et la géométrie des pièges [15, 16, 17, 18] contenant le gaz de Bose, à 1D et 3D. Enfin, nous présentons des résultats théoriques obtenus concernant le spectre des bosons 1D

dans un anneau sous l'effet de rotation externe [19, 20, 21, 22] ainsi que l'état quantique du système [23, 24, 25].

Dans le **troisième chapitre**, nous présentons notre solution exacte de l'équation de Schrödinger pour l'Hamiltonien (1.0.1). Dans le cas des bosons libres la fonction d'onde de plusieurs particules est le produit des fonctions d'ondes d'une seule particule. Donc il faut résoudre l'équation de Schrödinger pour une seule particule. Dans le cas des bosons fortement corrélés, il existe une solution exacte qui est le 'Fermi-Bose mapping' trouvée en 1960 par M.D. Girardeau [13] et qui permet d'écrire la fonction d'onde utilisant la fonction d'onde des fermions libres

$$\Psi_{TG}(x_1, ...x_N, t) = \mathcal{A}(x_1, ...x_N)(1/\sqrt{N!}) \det[\psi_l(x_m, t)] \ . \qquad (1.0.2)$$

Puisque la fonction d'onde doit être symétrique il faut symétriser la déterminant de Slater par la fonction $\mathcal{A}(x_1, ...x_N) = \prod_{j<\ell} \mathrm{sign}(x_j - x_\ell)$. Comme dans le cas des bosons libres nous avons réduit le problème de N-corps à un problème d'une seule particule. Nous imposions des conditions aux limites périodiques pour la fonction d'onde. Nous imposions également comme condition initiale, que la barrière soit au repos à $t = 0$. Nous présentons la fonction d'onde du système et le spectre, en résolvant une équation transcendantale. On observe un spectre quadratique pour les particules avec un moment angulaire fixe. Nous obtenons donc une structure de bandes avec l'impulsion ($q = mv/\hbar$) de la barrière qui joue la rôle du pseudo moment dans un cristal. Le changement du moment angulaire est assuré par la barrière qui lève la dégénérance aux points de croisements entre les différentes paraboles. L'ouverture des anti-croisements est déterminée par la valeur de la barrière U_0. Dans le cas d'un potentiel extérieure faible, $mU_0L/\hbar^2 \lesssim 1$, nous effectuons une analyse perturbative. Ensuite, nous comparons la structure de bandes en fonction de la forme du potentiel extérieure (potentiel en forme de fonction Delta ou potentiel rectangulaire) et nous discutons les déviations observées.

Dans le **quatrième chapitre**, nous discutons les propriétés superfluides des bosons libres et du gaz de Tonks. Nous donnons une brève introduction sur les propriétés superfluides du gaz de Bose 1D [26, 27, 10, 28, 29, 30, 31, 32, 33]. Nous effectuons une analyse du courant des particules, de ses fluctuations et de la force de traînée. Nous trouvons un comportement superfluide en-dessous d'une vitesse critique de la barrière qui est égale à $v_c = \hbar\pi/(mL)$. Le courant et ses fluctuations sont fortement dépendants de la dynamique de la barrière. À $t = 0$, la barrière est mise en rotation, soit de

manière adiabatique, soit instantanément. Dans le cas d'un mouvement adiabatique, le comportement du courant en fonction de la vitesse de la barrière a une forme en marches d'escalier. Pour des valeurs spéciales de la vitesse v telle que $v = (2n+1)\hbar\pi/(mL)$, avec n un entier naturel, un quantum de moment angulaire entre dans le système bosonique, par conséquent le courant augmente d'un quantum de $N\hbar\pi/(mL^2)$. Dans le cas d'une barrière hors équilibre (barrière mise en rotation instantanément), on observe un comportement différent. Le courant est égal à zéro excepté pour des valeurs spéciales de la vitesse $v = n\hbar\pi/(mL)$, où on observe un courant piqué. Puisque la force de traînée est seulement définie pour la barrière hors-équilibre, le comportement de la force ressemble beaucoup au comportement du courant hors équilibre. Pour une vitesse de la barrière $v = n\hbar\pi/(mL)$, on observe une oscillation de la force avec le temps. La période d'oscillation est donnée par la fréquence des anti-croisements dans le spectre.
Dans le **cinquième chapitre**, nous discutons de la dynamique du système ainsi que de la nature de son état quantique. On donne une brève introduction à la physique des superpositions macroscopiques, ses possibles applications dans les mesures de haute précision [34] et dans l'information quantique [35] ainsi que aux progrès expérimentaux [36, 37, 38]. Dans le but d'une application expérimentale de notre système nous nous focalisons sur le gaz de Tonks et sur la barrière hors-équilibre. Nous étudions les oscillations de Rabi, observées entre les états correspondant aux anti-croisements du spectre. Dans les analyses de la distribution des impulsions, de la fonction de Wigner et des images "temps de vol" pour une vitesse de la barrière $v = n\hbar\pi/(mL)$, on trouve que l'état du système est une superposition macroscopique de deux sphères de Fermi, l'une centrée autour de l'impulsion égale à zéro et l'autre autour de l'impulsion égale à $2q$, avec $q = mv/\hbar$. Cet état est un état fortement corrélé, non-classique car la fonction de Wigner atteint des valeurs négatives. Le fait que l'état n'est pas seulement un mélange statistique de deux états avec une impulsion différente peut ainsi être vu dans les images de temps de vol.
Dans le **sixième chapitre**, on donne un résumé de la thèse et on explique les questions ouvertes pour le futur.

List of important symbols

$\mathcal{A}(x_1, ...x_N)$	Tonks Girardeau mapping function
a_{3D}	3D s-wave scattering length
a_{1D}	effective 1D scattering length
$a_\perp$	is the radial oscillator length
$\alpha_q^{(j)}$	expansion coefficient for the plane waves
c_{jl}	$\langle\phi_{j,q}\|e^{-iqx}\|\phi_l^{(0)}\rangle$
$C_2(x, y, t)$	particle current-current correltation function
$\Delta E_q^{(l)}$	energy level splitting between the $l$the and the $l+1$th particle
ΔI	particle current fluctuations
$E_{l,q}$	single-particle energy of the lth particle
$E_\perp$	transverse excitation energy
$E_{id}^{(0)}$	ground state energy of the ideal Bose gas
$E_{TG}^{(0)}$	ground state energy of the TG gas
$f_W(X, k, t)$	Wigner quasiprobability distribution function
F_{ij}	$\langle\phi_{i,q}\|\partial_x\|\phi_{j,q}\rangle$
$\mathcal{F}_{ij}$	$\langle\phi_{i,q}\|\partial_x^2\|\phi_{j,q}\rangle$
F_{drag}	drag force
g_{3D}	3D interaction strength
g_{1D}	effective 1D interaction strength
$g\ (= g_{1D})$	Lieb Liniger contact interaction strength
$\gamma = gmL/(\hbar^2 N)$	dimensionless Lieb Liniger interaction strength
$\mathcal{H}_B$	many-body Hamiltonian
$\mathcal{H}_{LL}$	Lieb-Liniger Hamiltonian
$\hbar$	Planck constant
I	time averaged spatially integrated particle current
$j(x, t)$	particle current density
$J_0(x)$	first spherical Bessel function

K	Luttinger parameter
k_l	particle momentum vector of the lth state
$k_l^{(s)}$	particle momentum vector in the case of a square barrier
$k_l^{(2)}$	particle momentum vector in the barrier region
$k_F = N\pi/L$	Fermi momentum vector
$\kappa(\gamma)$	pseudo Fermi momentum
L	ring circumference
$\mathcal{L}$	total angular momentum
ℓ	square barrier length
λL	dimensionless barrier strength
$\lambda^{(s)}\ell L$	dimensionless square barrier strength
m	particle mass
N	particle number
N_0	number of condensed particles
$\mathcal{N}_j$	Normalization constant for the jth orbital
$n_B(k,t)$	particle momentum distribution
n_k	particle number distribution
$n_{TOF}(k)$	Time of flight signal
$n(x,t)$	time dependent longitudinal density
Ω	barrier angular velocity
ω_0	average frequency of the characteristic oscillations
$\omega_\perp$	frequency of the 2D transverse harmonic confinement
ω_x	frequency of the longitudinal confinement
$\hat{p}_l$	1D momentum operator acting on the lth particle
Φ_0	Coriolis flux quantum
$\phi_l^{(0)}$	initial single-particle orbital
$\phi_{j,q}(x)$	single-particle orbital
$\phi_{j,q}^{(s)}(x)$	single-particle orbital for the square barrier
$\phi_{j,q}^{(pert)}(x)$	perturbative single-particle orbital

$\Psi_B(x_1...x_N,t)$	bosonic many-body wavefunction
$\Psi_{id}(x_1...x_N,t)$	bosonic many-body wavefunction for the ideal Bose gas
$\Psi_{TG}(x_1...x_N,t)$	bosonic many-body wavefunction for the Tonks-Girardeau gas
$\psi(x,t)$	single-particle wavefunction
$\psi_l(x,t)$	single-particle wavefunction of a particle in the lth state
q	barrier momentum vector
q_c	critical barrier momentum vector
R	ring radius
r	relative particle coordinate
ρ_0	average particle density
$\rho_B(t)$	full density matrix
$\rho_B(x,y,t)$	one-body density matrix
τ	average Rabi oscillation time
t	time
$t_0 = mL^2/(\hbar\pi)$	natural timescale
u_s	velocity of sound
$\mathcal{U}_1$	first unitary transformation (spatial translation)
$\mathcal{U}_2$	second unitary transformation (momentum shift)
$U_{ext}(x,t)$	external driving potential
$U_{barr}(x)$	square barrier potential
U_0	barrier strength
$U_0^{(s)}$	square barrier strength
v	barrier velocity
v_c	critical barrier velocity
x	single-particle coordinate
X	center of mass coordinate

II The one dimensional Bose gas

This first chapter aimed at providing a brief introduction and the necessary background on 1D Bose gases in order to set the stage for our research and hence the content of this thesis. We outline both the theoretical and experimental framework for the research field showing its timeliness. Making a link with the most recent works we emphasize the need for further investigation in order to complete the physical understanding of strongly interacting ultracold bosonic gases rotating on a ring trap.
In particular we introduce the principle of rotation, making a link with Bloch's theorem. We provide the reader with the textbook description of one-dimensional bosons and introduce standard language. On the theoretical side two standard models are presented that describe interacting bosons, i.e. the Lieb-Liniger model for arbitrary interactions [11, 12] and the Bose-Fermi mapping for the impenetrable boson limit [13]. On the experimental side, 1D ring traps are not yet accessible. Hence we describe the state of the art experiments on a) strongly interacting bosons in 1D and b) 3D ring traps. Finally we present the most recent theoretical works concerning interacing 1D bosons confined to a toroidal geometry.

II.1 The ideal Bose gas under rotation on a ring trap

Before considering a more complicated Hamiltonian including interactions between the particles we want to study the problem of N noninteracting (ideal) bosons confined to a 1D ring geometry of circumference L under the influence of rotation. This toy model displays already several features of the interacting model and can be understood in a very intuitive way. The corresponding single-particle Hamiltonian reads

$$\mathcal{H}_B = \frac{1}{2m}\sum_{l=1}^{N}\left(\hat{p}_l - mv\right)^2 \ , \tag{2.1.1}$$

where $\hat{p}_l = -i\hbar\partial_{x_l}$ is the 1D momentum operator and x is the particle coordinate along the ring circumference. The tangential velocity of the rotation, $v = \Omega R$, is given in terms of the angular frequency Ω and the ring radius $R = L/2\pi$. Following the formal analogy to the electro-magnetic equivalent, this velocity field corresponds to a Coriolis flux $\Phi = Lv$ entering the ring. The rotation acts as an artificial gauge-field on neutral particles in a similar fashion as the vector potential **A** of the electro-magnetic field acts on charged particles on a loop threaded by a magnetic flux $\Phi_B = S_A B$ in the Aharonov-Bohm effect [39], with $\mathbf{B} = \nabla \times \mathbf{A}$ and S_A being the surface area of the loop.

As a starting point we consider the special case of $v = 0$, i.e. the artificial gauge field $m\mathbf{v}$ is absent. The many-body wave function of the bosons has a product form where each boson is described by the same single-particle wave function

$$\Psi_{id}(x_1, ..., x_N, t) = \prod_{l=1}^{N} \psi(x_l, t) \ . \tag{2.1.2}$$

The many-body wave function has to fulfill periodic boundary conditions (PBCs) for each particle $l = 1...N$, i.e. $\Psi_{id}(x_1, ..., x_l, ..., x_N, t) = \Psi_{id}(x_1, ..., x_l + L, ..., x_N, t)$. Consequently, the single-particle wave functions $\psi(x, t)$ have to fulfill PBCs. In the absence of an external potential the solution of the Schrödinger equation yields plane waves $\psi_j(x, t) = 1/\sqrt{L}\exp(i(k_j x - \epsilon_j t/\hbar))$. The wave vectors are given by $k_j = 2\pi(j-1)/L$, the momentum per particle by $\hbar k_j$ and $\epsilon_j = \hbar^2 k_j^2/2m$ is the energy per particle. Since all particles are located in the lowest orbital $j = 1$ it is possible to drop the index j in k_j and ϵ_j.

Coming back to the Hamiltonian in Eq.(2.1.1) with nonzero velocity, its form suggests to perform a gauge transformation which shifts the momentum by mv. This is achieved by the application of the unitary transformation $\mathcal{U} = \exp(imvx/\hbar)$. Once this transformation acts on the wave function $\psi(x) \longrightarrow \mathcal{U}\psi(x)$, the PBCs translate into twisted boundary conditions (TBCs)

$$\psi(x + L, t) = e^{imvL/\hbar}\psi(x, t) \ , \tag{2.1.3}$$

which means that a phase factor is added to the wave functions upon a full rotation. This is in full analogy with the Aharonov-Bohm effect. A quick inspection of the single-particle wave function in Eq.(2.1.3) reveals that it also obeys Bloch's theorem by construction, with $q = mv/\hbar$ playing the role of the quasi-momentum in a solid.

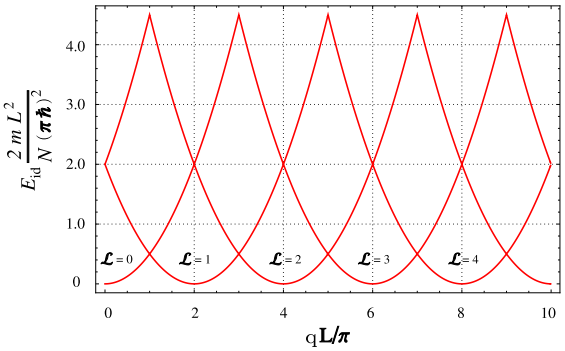

Figure II.1: Bandstructure for ideal bosons on a ring of circumference L under the influence of an artificial gauge field. The energy is given in units of $N(\pi\hbar)^2/(2mL^2)$ and the crystal momentum in units of π/L. A repeated pattern of parabolas is obtained corresponding to different states of given angular momentum $\mathcal{L}$, indicated in the figure.

Therefore, it can already be anticipated that the energy level dispersion of the free Bose gas under the influence of such an artificial gauge field is in close analogy to the bandstructure for Bloch electrons in a crystal. It depends parametrically on the quasi-momentum q of the artificial gauge field and is periodic with period $q_0 = 2\pi/L$, corresponding to a quantum of the Coriolis flux $\Phi_0 = 2\pi\hbar/m$. The single particle wave function for each boson may thus be written in the form of Bloch wave functions, i.e. $\psi_{j,q}(x)$, with band index j and quasimomentum q. For ideal bosons all particles are in the lowest band, hence $j = 1$.
Figure II.1 shows the energy dependence of the ideal Bose gas on the quasi-momentum of the artificial gauge field. A repeated pattern of parabolas is obtained, where each parabola represents a state of fixed total angular momentum. At half-integer values of the momentum ratio q/q_0, with $q_0 = 2\pi/L$, a real level crossing occurs. In principle these points allow for a change of angular momentum. However, without a mechanism that breaks translational invariance and opens gaps between the branches the total angular momentum is conserved.

II.2 Theoretical models for Bosons in one dimension

In this section we focus on the theoretical approaches to describe interacting 1D bosons. In dilute cold atomic gases interactions between particles are due to two-body collisions and at low temperatures are well described by a contact potential of the form $U(\vec{r}) = g_{3D}\delta(\vec{r})$, with the three-dimensional (3D) interaction strength $g_{3D} = 4\pi\hbar^2 a_{3D}/m$,

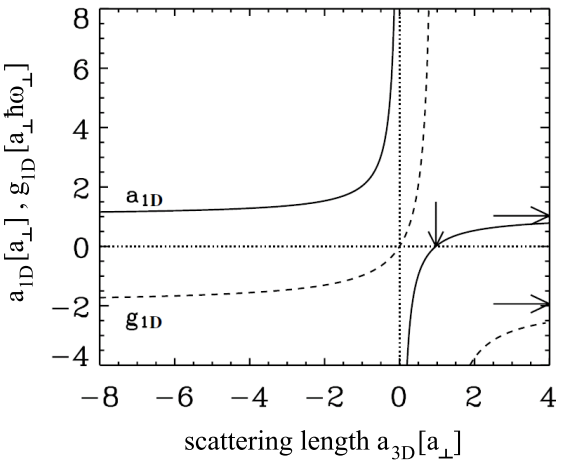

Figure II.2: The 1D scattering length a_{1D} and the 1D effective interaction strength g_{1D} as a function of the 3D s-wave scattering length a_{3D} in units of the transverse oscillator length $a_\perp$ and the radial oscillator frequency $\omega_\perp$. [41].

parameterized by the 3D s-wave scattering length a_{3D}. In 1998 Olshanii [40] showed that for atoms in the presence of a tight two-dimensional (2D) harmonic confinement potential (in x and y direction) of frequency $\omega_\perp$ the effective 1D scattering length (in z direction) reads

$$a_{1D} = -\frac{a_\perp^2}{a_{3D}}\left(1 - C\frac{a_{3D}}{a_\perp}\right) , \tag{2.2.1}$$

where $a_\perp = \sqrt{\hbar/(m\omega_\perp)}$ is the radial oscillator length and $C = 1.4603...$ is a numerical factor. The effective 1D interaction strength then reads

$$g_{1D} = \frac{g_{3D}}{\pi a_\perp^2}\left(1 - C\frac{a_{3D}}{a_\perp}\right)^{-1} . \tag{2.2.2}$$

The dependence of g_{1D} and a_{1D} on the 3D s-wave scattering length shown in Fig.II.2. The dependence of the interaction strength on the radial trapping frequency in Eq.(2.2.2) is denoted as confinement-induced resonance. Therefore, interactions between the bosons are tunable by the transverse confinement alone. This is an additional tuning parameter with respect to the 3D case where the magnitude and sign of the 3D scattering length can be tuned by applying an external magnetic field (Feshbach resonances). Depending on the value of the 1D interaction strength g_{1D} between the bosons there are specific solutions available. In absence of external confinement an exact solution of the many-body wave function was derived by Lieb and Liniger [11, 12] in 1963. This milestone result will be discussed in Sec.II.2.3. For weak interactions, mean field (MF) theory, i.e. the Gross-Pitaevskii equation (GPE) [42, 43] is commonly used to

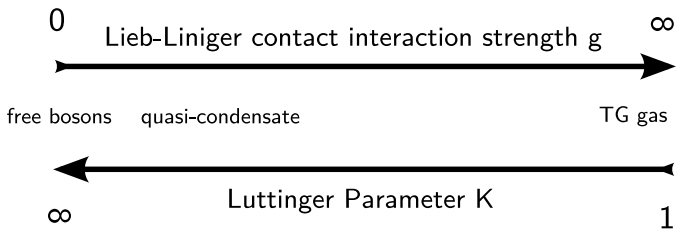

Figure II.3: The 1D interaction strength between the particles is usually labeled by the Lieb-Liniger interaction strength g and the Luttinger parameter K. Since there is no simple relation between the two parameters the figure sketches their relation to each other.

describe ultra cold atomic gases. A very powerful and elegant method is the Luttinger liquid approach [44, 45, 46] if only the low-lying excitations of the energy spectrum are needed. In the case of infinitely strong interactions (TG-limit) between the particles with arbitrary external potential an exact solution exists [13, 14] which will be discussed in Sec.II.2.4. All these models reveal the special character of 1D systems compared to their 3D counterparts, such as the nature of collective excitations and the existence of enhanced quantum fluctuations.

Among the possibilities to characterize the interaction strength in 1D, there are two commonly used parameters in the literature. The interaction strength g_{1D}, entering the Lieb-Liniger model (being in the 1D regime we will denote it by g from now on) The second possibility to describe the 1D interaction strength is the Luttinger parameter K. Their relation to each other is sketched in Fig.II.3.

II.2.1 Quasi-one-dimensionality

Several physical systems display quasi-1D or quasi-2D character, such as, e.g. graphene, carbon nanotubes, quantum dots, etc. Reduced dimensionality is obtained when transverse degrees of freedom are frozen out. For cold atomic gases this is usually done by spatially confining the particles via optical, magnetical or magneto-optical traps as used for the creation of 3D Bose-Einstein condensates [47]. However, in contrast to a 3D Bose-Einstein condensate (BEC) the trapping potential in the transverse direction(s) is chosen to be extremely tight. For a harmonic trapping potential the quasi 1D condition states that all typical energy scales are smaller than the transverse excitation energy $E_\perp = \hbar\omega_\perp$ needed to create the first excited state in the transverse direction, i.e. the particles only occupy the transverse ground state. This reads

$$E_{th}, E_{ex}, \mu \ll E_\perp \ , \tag{2.2.3}$$

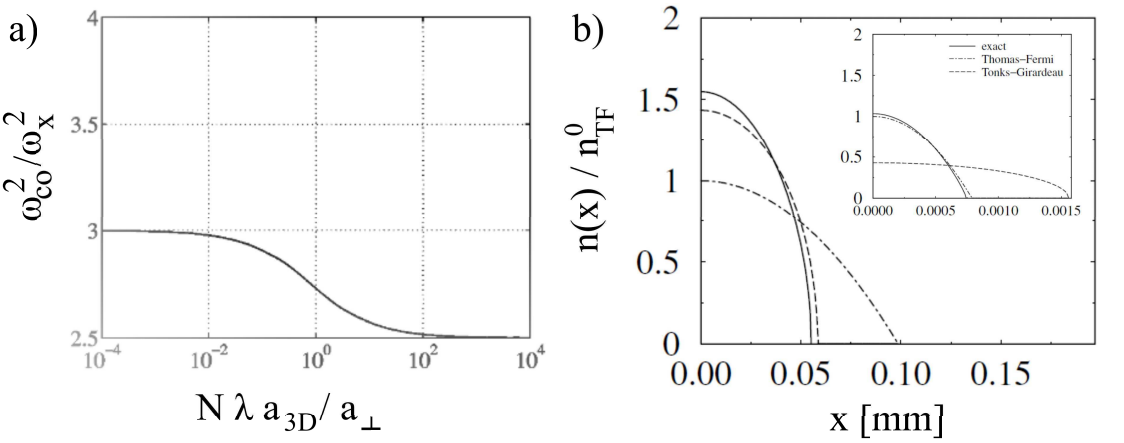

Figure II.4: a) Transition between the 3D and the 1D regime [48]. The frequency of the lowest compressional mode ω_{co} in units of the trapping frequency along the tube axis ω_x is shown as a function of the dimensionless parameter $N\lambda$ with $\lambda = \omega_x/\omega_\perp$. The 3D scattering length is given by a_{3D}. b) The longitudinal density $n(x)$ in units of the $n^0_{TF} = [(9/64)N^2(m\omega_x/\hbar)^2|a_{1D}|]^{1/3}$ as a function of the position x along the tube axis. The main panel shows the strongly interacting regime, where the density profile obtained from the Lieb-Liniger model agrees with the predictions of the Tonks-Girardeau solution. Inset: In the limit of weak interactions, i.e. in the Gross-Pitaevskii/Thomas-Fermi regime, a reduced cloud size is observed. From [49].

with $E_{th} = k_B T$ being the thermal energy of the gas, E_{ex} being the excitation energy of the gas in the dimension(s) of interest and μ the chemical potential.

In the specific case of the widely used cigar-shaped trapping geometry, with potential $V = (1/2)\ m\omega_\perp^2(y^2+z^2) + (1/2)\ m\omega_x^2 x^2$, a transition between the 3D gas and the 1D gas is expected for increasing aspect ratio $\omega_\perp/\omega_x$. The dimensionality crossover can be monitored on some observables of experimental interest. Close to the 1D regime the density profiles in the transverse direction acquire the size of the transverse ground state. Under a small periodic variation of the longitudinal confinement the time dependent density can be linearized $n(x,t) = n(x) + \exp(i\omega_{co}t)\delta n(x)$, defining the collective oscillation modes ω_{co}. It was found that the frequency of collective excitations ω_{co} is blue-shifted due to the change of compressibility with aspect ratio $\omega_\perp/\omega_x$ [48], see Fig.II.4 a). Once the 1D regime has been reached, at increasing interaction strength the shape of the longitudinal profile $n(x,t)$ changes from Gross-Pitaevskii to Tonks-Girardeau and its width increases [49], see Fig.II.4 b).

II.2.2 Absence of Bose Einstein condensation and quasi off-diagonal long range order

One of the formal ways to define a BEC is the presence of off-diagonal long-range order. For a uniform system this can be defined in two equivalent ways [50]. (1) The one-body density matrix (OBDM) $\langle \Psi^\dagger(x)\Psi(x')\rangle$ tends to a non-zero value for $|x-x'| \longrightarrow \infty$. (2) The OBDM has an eigenvalue of the order of the particle number N, i.e. there is a number of condensed particles $N_0 \sim N$. In fact, the above definitions present two main characteristics of BEC: first order spatial coherence over the whole length of the system and macroscopic occupation of a single quantum state. The common concept of BEC in 3D has to be rediscussed once dimensions are reduced. Two fundamental inequalities have been derived which ensure that there is no true off-diagonal long-range order in 1D and thus no condensation is found.

In the case of $T > 0$ the Schwarz inequality in Bogoliubov's form which sets a lower bound for the fluctuations of a given operator has been used by Mermin and Wagner [51] and by Hohenberg [52] to study the infrared divergence of the particle distribution n_k function with the result

$$n_k \geq \frac{mk_BT}{k^2}\frac{N_0}{N} - \frac{1}{2}\,, \tag{2.2.4}$$

Clearly $N_0 = 0$ must be demanded due to the characteristic quadratic infrared divergence $1/k^2$ at $k = 0$ upon integration over k. Otherwise, both the condensed number of particles N_0 and the number of non-condensed particles would be of macroscopic order which is in contradiction. This result was obtained under the assumption that the system is at thermal equilibrium. The physical interpretation is that thermal fluctuations of the phase are responsible for the absence of BEC. In the case of $T = 0$ only quantum fluctuations occur and the above described approach needs to be generalized. Starting from the Schwarz inequality, Pitaevskii and Stringari found a way to set an inequality for the particle number distribution connected to the static structure factor $S(k)$ [53] which yields a lower bound for the particle number distribution,

$$n_k \geq \frac{1}{2S(k)}\frac{N_0}{N} - \frac{1}{2}\,. \tag{2.2.5}$$

Since $S(k) \leq \hbar k/(2mu_s)$, with the sound velocity u_s, a linear infrared divergence occurs in the particle number distribution function upon integration over k. Again, both the condensate fraction and the non condensate fraction would be of order unity,

unless there are no condensed particles. Therefore, a homogeneous atomic gas does not show BEC, not even at zero temperature.
However, the phonon-like dispersion which characterizes the 1D homogeneous Bose fluid ensures quasi off-diagonal long range order (QODLRO). This means that the OBDM decays with a power-law

$$\langle \Psi^\dagger(x)\Psi(x')\rangle \longrightarrow \frac{2}{|x-x'|^{1/2K}} \tag{2.2.6}$$

for $|x-x'| \longrightarrow \infty$ where the exponent depends on the interaction strength through the Luttinger exponent K. For weak interactions $K \gg 1$ the OBDM displays a very slow decay since the power is very small. The atomic gas is said to be in a quasi-condensate state, showing a physical behavior close to a real condensate. For very strong interactions in the impenetrable boson limit (Tonks Girardeau) $K = 1$ this power is not small and no "condensate"-related effects are expected. This argument must be reviewed for trapped systems which have a finite size. In this case $|x-x'|$ is bound. For weak interactions and low temperatures phase-coherence is found and properties related to condensation are observable. For strong interactions , however, no BEC occurs, as it has been shown that in the TG limit the largest eigenvalue of the OBDM scales as $\sqrt{N}$ [54], as we shall see in Sec.II.2.4 below.
The above discussion illustrates the need of a precise understanding of the experimentally relevant case of a finite, trapped system. In the case of a ring trap of small size, for example, important mesoscopic effects occur, as it will be discussed in chapter IV.

II.2.3 The Lieb-Liniger model

Despite the fact that quantum mechanics is a well established theory, for only few Hamiltonians the Schrödinger equation is known to be exactly solvable and suitable to real physical many-body problems at the same time. In general, approximations are needed in order to obtain a solution for such demanding problems and thus the search for more precise approximate solutions has been a major axis of scientific investigation for several decades. Various techniques have been developed, allowing to describe the problem almost exactly in some limits. However, there are still islands of exact solvability. These special cases are not only interesting for their beauty and mathematical rigor but they are also very important in order to prove the validity of the above mentioned approximations. One of these examples is the Lieb-Liniger model [11, 12] for a

1D many-body problem with a contact interaction potential between the particles. Its Hamiltonian reads

$$\mathcal{H}_{LL} = -\frac{\hbar^2}{2m}\sum_{l=1}^{N}\frac{\partial^2}{\partial x_l^2} + g\sum_{j<l=1}^{N}\delta(x_l - x_j)\ , \tag{2.2.7}$$

where g is the particle interaction strength. Starting from a Bethe Ansatz the wave function for the first coordinate sector $x_1 \leq x_2 \leq ... \leq x_N$ reads

$$\Psi_B(x_1...x_N) = \sum_{\mathcal{P}} a(\mathcal{P})\exp(i\sum_{j=1}^{N} k_{\mathcal{P}(j)}x_j)\ , \tag{2.2.8}$$

where $\mathcal{P}$ describes all possible permutations of momenta $\{k_1...k_N\}$ and the coefficients $a(\mathcal{P})$ are determined by the possible two-body collisions. In other coordinate sectors the wave function is obtained from the bosonic symmetry under particle exchange. If the particle position is distinct for all N particles then Eq.(2.2.8) is a linear combination of plane waves because the contact interaction potential in Hamiltonian (2.2.7) does not contribute. However, upon a collision between two particles the contact term gives a contribution while the conservation of momentum in the subsystem of the two particles must be obeyed. Imposing cusp conditions and PBCs on the wave function, the pseudo momenta of the particles are determined through the equation

$$\delta_j \equiv (k_{j+1} - k_j)L = \sum_{s=1}^{N}(\theta_{sj} - \theta_{s,j+1}) + 2\pi n_j \quad \text{for} \quad j = 1...N-1 \tag{2.2.9}$$

$$\theta_{sj} = -2\tan\left[\frac{\hbar^2(k_s - k_j)}{gm}\right]^{-1}\ , \tag{2.2.10}$$

where $n_j \geq 1$ is an integer referring to the particle index j. The ground state is readily built upon the choice $n_j = 1\ \forall\ j$ since it minimizes the δ_j's and thus the states lie closest in k-space. This corresponds to filling up a pseudo-Fermi sea of Fermi momentum κ. The states are symmetrically distributed between $-\kappa...\kappa$ yielding zero total momentum, where $\kappa = \kappa(\gamma)$ is a function of the dimensionless parameter $\gamma = mgL/(\hbar^2 N)$ which describes the interaction strength between the particles.

Taking the thermodynamic limit for large systems, i.e. $N, L \to \infty$ while keeping the the particle density N/L constant, the ground state energy of the Lieb-Liniger gas $e(\gamma)$ is a continuous function of γ. For $\gamma = 0$ the ground state energy of the free Bose gas is obtained while for $\gamma \to \infty$ it conicides with the energy of the TG gas. The calculation needs to be done numerically and the result is plotted in Fig.II.5 a). A

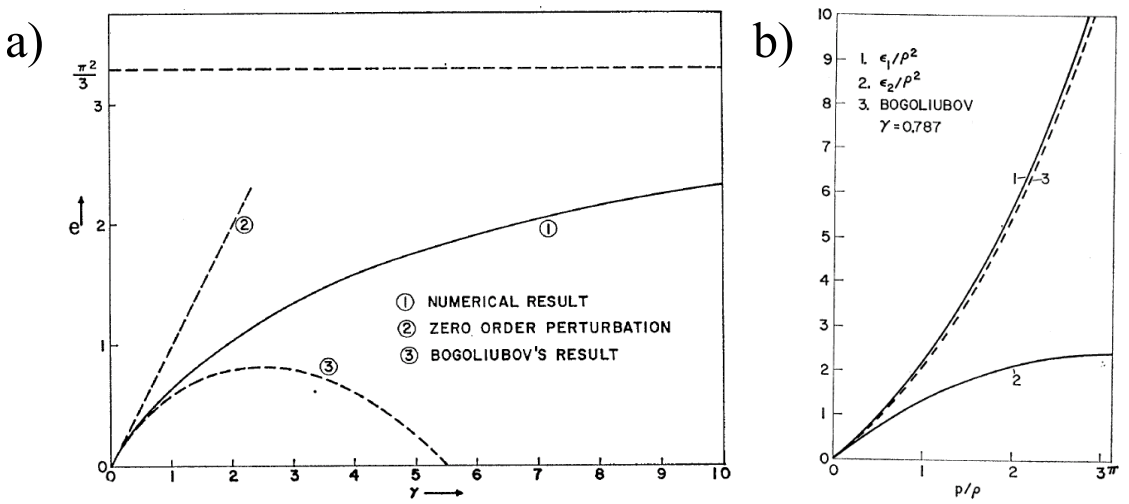

Figure II.5: a) The Lieb-Liniger ground state energy $e(\gamma)$ as a function of the dimensionless parameter $\gamma = mgL/(\hbar^2 N)$, taken from [11]. The exact result of the Lieb-Liniger calculation is compared with a zero order perturbative analysis and the Bogoliubov perturbation theory for small γ. Up to $\gamma = 2$ the Bogoliubov's perturbative calculation yields good results for the ground state energy. The dashed horizontal line gives the exact result in the TG limit for $\gamma \to \infty$. Surprisingly, γ is as large as 37 in order to be in only 10% vicinity of the TG ground state energy. b) The Lieb I and II excitation modes taken from [12]. The excitation energy $\epsilon_{1,2}$ is given as a function of the total momentum p in units of $\rho = N/L$ for a fixed value of $\gamma = 0.787$. The dashed line is the result of Bogoliubov's perturbative analysis.

very important observation is the singularity of $e(\gamma)$ at $\gamma = 0$. Therefore, perturbation theory can at best be asymptotic in the limit of small γ. Physically this means that an interacting system, no matter how weak the interactions between the particles are, is fundamentally different from the non-interacting system.

The excitation spectrum of the Lieb-Liniger model was obtained by E. Lieb [12] and is shown in Fig.II.5 b). The simplest excitation is obtained when one of the above mentioned n_j's is not unity but two. This increases the corresponding δ_j by 2π while the other δ_j's are shifted slightly. The result is a many-body state carrying a non-zero total momentum. Lieb found two types of possible excitations that he labeled type I and type II. The type I excitations are the so-called elementary excitations and coincide with Bogoliubov's excitation spectrum at weak interactions. These "particle excitations" are created by taking a particle with momentum $|k_p| = \kappa$ from the pseudo-Fermi sea and adding a particle with momentum $|k_p| > \kappa$. The type II excitations are obtained by removing a particle, or creating a hole, of momentum $0 < |k_h| < \kappa$ from the ground state and adding a particle with momentum $|k_p| = \kappa + 2\pi/L$. The latter case has no equivalent in Bogoliubov's perturbative analysis. It has been shown that

the Lieb II excitations can be identified with the appearance of dark solitons states [55]. It can be seen that the total momentum p created by the excitation is unlimited for the type I excitations $-\infty < p < \infty$ whereas for the type II excitations it is limited $-N\pi/L \leq p \leq N\pi/L$ showing their different character. However, it should be mentioned that any type II excitation may be thought of as a multiple type I excitation. For the first particle/hole excitation this becomes obvious since they are identical.

II.2.4 The Tonks-Girardeau gas

In section II.2.3 the exact solution for a 1D Bose gas interacting via a contact potential of strength g was derived from a Bethe Ansatz. Interestingly, the Bethe Ansatz solution conicides with a second exact solution to the problem provided by the Bose-Fermi mapping theorem in the impenetrable-boson (Tonks-Girardeau) limit of infinitely strong interactions $g \to \infty$ between the particles [13]. The real power of this method lies in the fact that it is capable to deal with an arbitrary external potential, added to Hamiltonian (2.2.7), not treatable with the Bethe Ansatz of Lieb and Liniger. This is due to the fact that in the $g \to \infty$ limit there is no length or energy scale associated with interactions which allows to solve inhomogeneous problems. For quantum gases this is a substantial advantage over the Lieb-Liniger model since it permits to calculate the exact many-body wave function in the presence of a trapping potential. The extension to the time-dependent case [14] even allows to access the dynamical properties of the strongly interacting Bose gas, again not accessible with the Bethe Ansatz solution. The starting point for the solution is the fact that the infinite delta-interaction potential requires the wave function to vanish upon contact of two particles. The same holds for fermions due to the Pauli exclusion principle. Girardeau's path-breaking idea was that the Pauli principle can model the effect of the interaction between the bosons. Therefore, the bosonic many-body wave function can be obtained from the many-body wave function of spinless non-interacting fermions

$$\Psi_{TG}(x_1, ...x_N, t) = \mathcal{A}(x_1, ...x_N)(1/\sqrt{N!}) \det[\psi_l(x_m, t)] \ , \qquad (2.2.11)$$

with $\mathcal{A}(x_1, ...x_N) = \Pi_{j<\ell}\mathrm{sign}(x_j - x_\ell)$ being a mapping function. The second term of the wave function is the well-known fermionic Slater determinant. The mapping function restores the symmetry of the bosonic wave function under exchange of two particles as required by bosonic statistics. The mapping function itself is odd, i.e. it

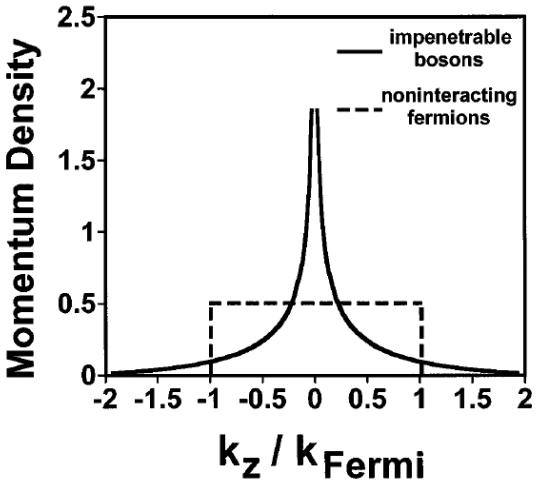

Figure II.6: Schematic momentum distribution for a TG gas and an ideal Fermi gas subjected to a trapping potential. From [40].

changes sign when two particles are exchanged. Since the only difference between the bosonic many-body wave function and the fermionic one is an overall phase in each coordinate sector, the ground state energy of the TG gas is the same as for the free fermions $E = \sum_{l=1}^{N} \hbar^2 k_l^2/2m$. Moreover, all quantities that only depend on the absolute value of the wave function, such as the density profiles or the density correlation function are thus identical for the free Fermi gas and the TG gas. On the other hand the one-body density matrix, the momentum distribution etc. are strongly affected by the phases imposed through the sign-functions in $\mathcal{A}(x_1, ...x_N, t)$. This renders their evaluation more intricate and the results differ substantially from their fermionic counterpart.

In his pioneering work, Girardeau gave an estimation for the momentum distribution $n_B(k) = \int dx \int dy e^{ik(x-y)} \rho_B(x, y)$, defined in terms of the one-body density matrix

$$\rho_B(x, y) = N \int dx_2 ....dx_N \Psi^*_{TG}(x, x_2 ...x_N) \Psi_{TG}(y, x_2 ...x_N) \ , \qquad (2.2.12)$$

which has been investigated in detail both in the absence and in the presence of an external confinement and by several groups. The major features of the momentum distribution of the homogeneous TG gas, a non-singular and in particular continuous behavior close to zero momentum [56] and a $1/\sqrt{k}$ peak at zero momentum [56, 57] prove the absence of BEC for the infinitely large system.

A qualitative comparison between the fermionic momentum distribution and the bosonic one is shown in Fig.II.6. As expected from intuition, in the bosonic case the zero

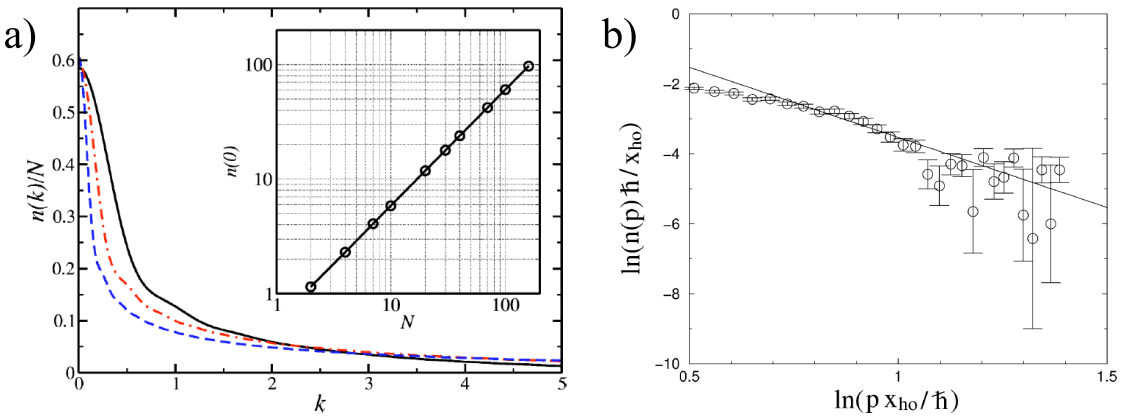

Figure II.7: a) Normalized momentum distribution in units of the particle number N as a function of the momentum k in units of the inverse oscillator length $1/l_{HO}$ for $N = 10$ (full line), $N = 40$ (dashed-dotted line) and $N = 160$ (dashed line) of bosons. The inset shows that the zero momentum peak scales with the particle number N. From [58]. b) Logarithmic momentum distribution $\ln n(p)$ in units of $l_{HO}/\hbar$ as a function of the logarithmic momentum p in units of $\hbar/l_{HO}$. The numerical data from the Monte Carlo simulation are compared with the predicted k^{-4} power law. From [59].

momentum states are more occupied than high momentum states, however, at the same time very high momentum states still have a non-zero occupation probability. This is in contrast to the free Fermi gas where the occupation probability is uniform and equal to 1 for momenta $0 < k < k_F$, k_F being the Fermi-momentum, and zero otherwise. In the case of harmonic confinement, i.e. when the single particle wave functions read

$$\psi_l(x,t) = \frac{1}{\sqrt{2^l\, l!\, l_{HO}\, \sqrt{\pi}}}\; e^{-iE_l^{(HO)}t/\hbar}\; \mathcal{H}_l(x/l_{HO})\; e^{-x^2/2\,l_{HO}^2}\;, \qquad (2.2.13)$$

where $E_l^{(HO)} = \hbar\omega(l+1/2)$ is the energy of the harmonic oscillator, $l_{HO} = \sqrt{\hbar/m\omega}$ the oscillator length and $\mathcal{H}_l(x)$ are the Hermite polynomials, Forrester and co-workers [54] calculated the occupancy of the two lowest natural orbitals of the one-body density matrix starting from the Ansatz $N_{0,1} = aN^p + b + cN^{-x}$ and fitting their numerical data by variation of x and p. For $2 \leq N \leq 30$ they found that the occupancy of the lowest orbital is given by $N_0 = 1.43\sqrt{N} - 0.56 + 0.12N^{-2/3}$ and for the second lowest orbital $N_1 = 0.67\sqrt{N} - 0.56 + 0.12N^{-4/3}$. The same leading $\sqrt{N}$ behavior was found in Ref. [58] from an analysis of the momentum distribution for particle numbers up to $N = 160$, see Fig.II.7 a).

An analysis of the high momentum states has been carried out by Minguzzi and co-workers [59]. They found that the momentum distribution decays as $n_B(k) \propto 1/k^4$

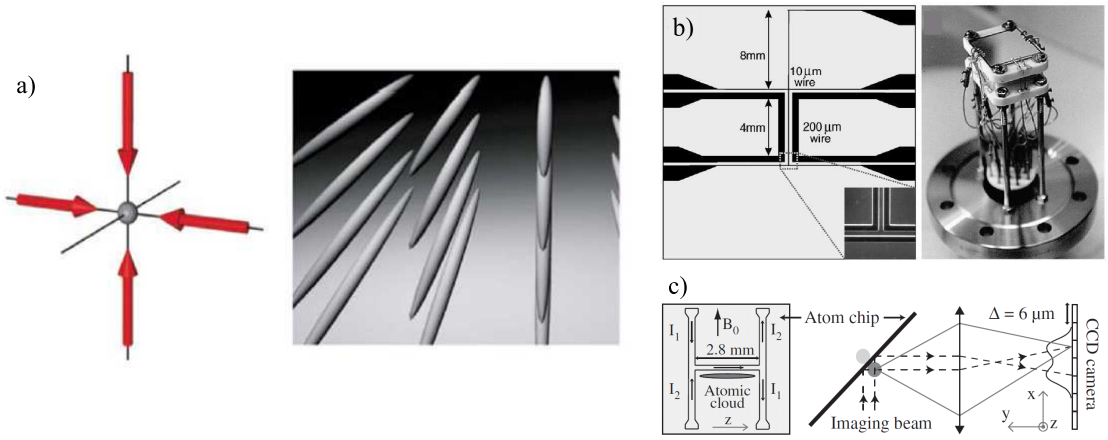

Figure II.8: a) Optical lattices created by superimposing orthogonal standing waves resulting in an array of 1D tubes. From [60]. b) and c) Magnetically trapped atoms on a chip. b) Schematics plus electron microscope image of the chip and photography of the whole experimental set-up. From [61]. c) Schematics of the atom chip and the imaging system. From [62].

for $k \to \infty$, see Fig.II.7 b). This means that the bosonic momentum distribution has indeed very long tails and is by no means comparable to its fermionic counterpart.

II.3 Experimental realization of one-dimensional geometries

The first big milestone for atom trapping and cooling was the creation of a BEC [63, 64] in a 3D magneto-optical trap in 1995, resulting in the Nobel prize for C. E. Wieman, E. A. Cornell and W. Ketterle in 2001. Their experiments were quickly followed by lower dimensional geometries of different shape and atom trapping is still a rapidly evolving field of research. The experimental realization of 1D systems of ultracold atoms is most commonly realized using two possible schemes. (i) Atom trapping in 2D optical lattices. In this first case, atoms are trapped in the minima of a periodic potential. This conservative potential is proportional to the intensity of a stationary light wave far detuned with respect to an optical transition [60]. If the lattice is applied in two orthogonal directions it gives rise to a sequence of quasi 1D tubes as illustrated in Fig.II.8 a). (ii) Atom trapping on a microchip. In this latter case atoms are trapped by

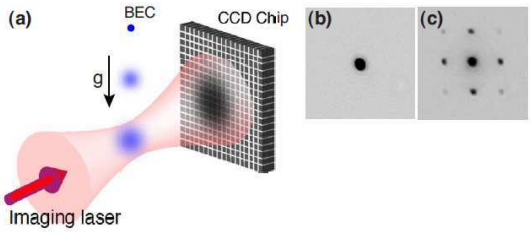

Figure II.9: Absorption imaging. a) Schematic set-up for imaging after TOF. b) Absorption image of a BEC released from a harmonic trap. c) Absorption image of a BEC released from an optical lattice. From [60]

the magnetic field resulting from a current flowing in the wires of the microchip. This is illustrated in Fig.II.8 b) and c).

Once the atoms are trapped and cooled down, specialized imaging techniques are needed in order to extract information about the physical observables of interest of the gas. In cold atomic gases only optical diagnostics can be used since the size of "contact probes" ($\sim 10^{13}$ atoms for a $10\mu m$ probe) is much bigger than the samples themselves ($\sim 10^2 - 10^7$ atoms) and would thus equilibrate the sample with the probe rather than the probe with the sample, i.e. the contact would heat up the probe. However, there is a vast variety of different optical methods used to probe cold atomic gases, both absorptive and dispersive imaging, see Ref. [65]. A major imaging technique that needs to be pointed out is the time-of-flight (TOF) measurement, illustrated in Fig.II.9. In the TOF measurement the confining potential is switched off at a given time, hence releasing the gas from the trap. This process of switching off the trapping potential can either be adiabatic or sudden. Here, we only consider the sudden switch. Due to the sudden release from the trap the gas still contains information about its initially correlated state. It expands freely due to its internal momentum and after a characteristic time t_{TOF}, the density profile of the atomic cloud is measured via absorption imaging techniques. The spatial density distribution of the cloud imaged by a CCD camera can be related to its initial momentum distribution via

$$\langle \hat{n}(\vec{x}) \rangle_{TOF} \propto \langle \hat{n}(\vec{k}) \rangle_{trap} \ , \tag{2.3.1}$$

where $\vec{k}$ (momentum of the gas in the trap) and $\vec{x}$ (position of the atoms after TOF) are related by the ballistic expansion condition $\vec{k} = m\vec{x}/\hbar t_{TOF}$ [60]. However, relation (2.3.1) only holds if there are no interactions between the particles during the time of expansion. In a similar fashion higher correlation functions, such as the density-density

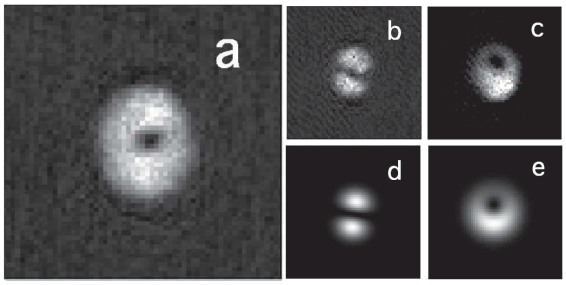

Figure II.10: a) Absorption image of a cloud containing one quantum of orbital angular momentum. b) Interference pattern between left (one quantum of orbital angular momentum) and right (one quanta of orbital angular momentum in the other direction) rotating clouds. c) Interference pattern between a non-rotating and a rotating cloud, showing a displaced hole. d) Calculated interference pattern between left and right rotating clouds. e) Calculated interference pattern between a non-rotating and a rotating cloud. From [9]

correlation function, can be measured.

II.3.1 Bosons on a ring traps in experiments

Among the various geometries mentioned at the beginning of this chapter there exists the possibility to create BECs confined to a 3D ring trap, e.g. [15, 16, 17, 18]. The topology of the ring geometry is particular since it allows for the investigation of many interesting physical observables, such as flow stability and superpositions of rotating an non-rotating states. Furthermore, in its limit of a very tight transverse confinement it is the most promising candidate to experimentally probe the peculiar aspects of 1D superfluidity.

The first storage ring for neutral atoms was reported in 2001 [66], where a multiple loading of the ring with atoms was achieved.

The first stable and smooth (uniform potential along the waveguide) circular waveguide for ultracold atoms was reached in 2005 [15]. Realizing a ring of diameter $1.2-3.0mm$, it was possible to set the condensate into motion by tilting the ring plane.

Rings of larger diameters and small heating effects have been reported at the same time [67]. By combining magnetic and optical fields, rings of high flexibility have been proposed which principally allow to reach the tightness needed for lower dimensional systems [68].

Another possibility to set a condenstate into motion has been put forward by the NIST group [9, 69]. It is based on transferring angular momentum to the condensate by means of an optical potential of Laguerre-Gauss form. The efficient transfer of angular

momentum to the condensate was demonstrated both by interferometric means, as is shown in Fig.II.10, and by observing a hole in the TOF image. They found that the survival probability of the flow strongly depends on the trapping geometry by changing between the simply connected (BEC in harmonic trap) and the multiply connected geometry (ring trap).

The realization of more flexible geometries have equally been demonstrated which allow to transform a toroidal condensate into a ring lattice and vice versa [70].

Another approach to induce rotation into a toroidal trap was used by Sherlock et al [17]. Starting from a BEC in a magnetically trapped ring geometry Sherlock and co-workers were able to introduce a spatially periodic variation of the trapping potential around the ring circumference. Upon rotation of this periodic potential it was possible to stir the atoms around the ring circumference. Then the circular symmetry was restored leaving moving atoms on a homogeneous ring trap.

In 2011 the NIST group [16] managed to create a quantized, persistent flow of Na-atoms around a multiply connected condensate, allowing for circulation times up to $40s$. In order to quantify the flow stability (under what circumstances does the persistent flow decay) a repulsive blue-detuned laser beam was inserted into the ring after $3s$ of circulation, acting as a barrier for the rotating atoms, see inset in Fig.II.11 a). The flow probability was studied as a function of the barrier height and the chemical potential of the condensate. This critical chemical potential (at which the persistent flow decays) was found to be proportional to the barrier strength, see Fig.II.11 b). Taking into account a locally (in the barrier region) enhanced flow velocity due to condensate depletion a critical flow velocity was found. This critical velocity is in good agreement with the Feynman critical velocity [71], taking into account vortex like excitations.

Very recently it was possible to observe very long-lived metastable superflow states of multiply charged vortices (the charge is equal to the phase winding number) in annular BECs [18]. Due to their metastability these vortices decay, revealing quantized steps in the supercurrent which can be seen in the radius of the cloud size, see Fig.II.11. These steps could be linked to vortex-induced 2π phase slips. At critical flow velocity as expected from Feynman's criterion the persistent current states decay. However, for velocities smaller than the Feynman critical velocity the decay probability is increased for states with lower vortices.

All the above experiments on ring traps are essentially 3D and so far a truly 1D ring does not exist. However, big efforts are made by various experimental groups in order

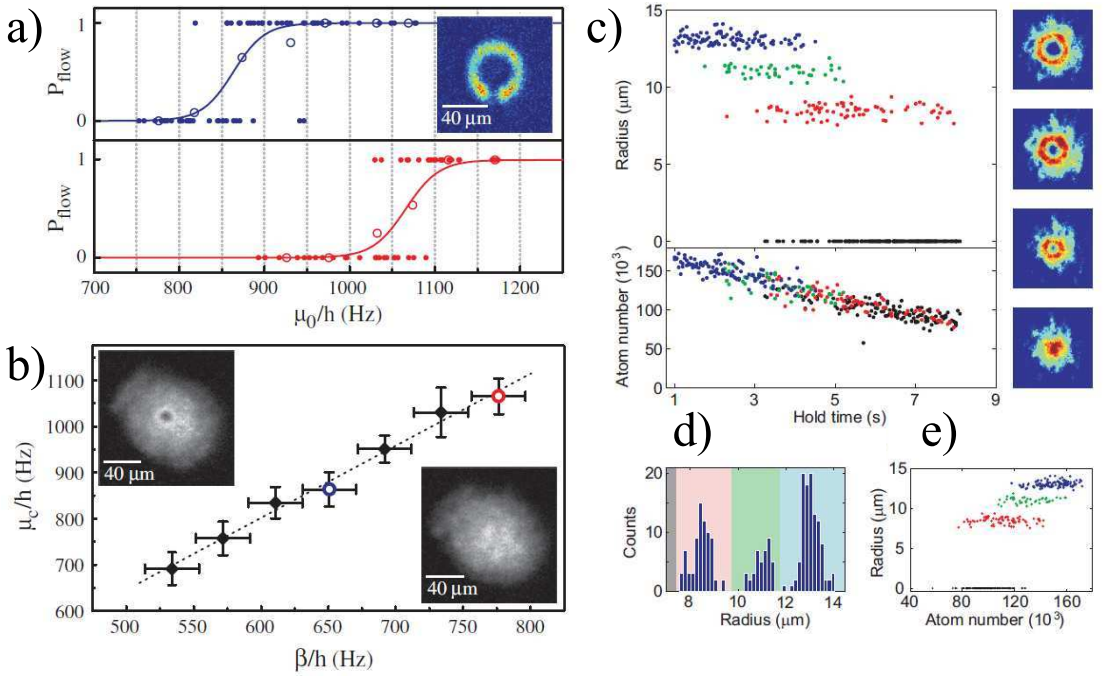

Figure II.11: Left panel: Flow stability as a function of the chemical potential μ_0 in units of h and the barrier strength β in units of the Planck constant h. a) Superflow is obtained when the chemical potential of the atoms is considerably higher than the barrier. The flow survival is displayed as a function of the chemical potential for two barrier heights $\beta/h = 650Hz$ (top panel) and $\beta/h = 780Hz$ (bottom panel). b) The resulting critical chemical potential of the atoms for the breakdown of the superflow as a function of the barrier height. Insets: TOF absorption images showing the presence (top) and absence (bottom) of circulation. From [16]. Right panel: The decay of quantized superflow states from triple charged (blue) to doubly charged (green) to simply charged (red) vortex states to the nonmoving condensate (black) due to phase slips of 2π. c) The radius of the atomic cloud and the number of atoms in the trap as a function of the experimental time. The steps for the radius proof the quantized nature of the superflow states. d) Statistics of the experiment shown in the histogram of the cloud radius. e) Cloud radius as a function of the number of atoms in the trap.

to improve their circular traps to access the 1D regime where interesting new physical phenomena are to be expected.

II.3.2 The Tonks-Girardeau gas in experiments

The strongly interacting Tonks-Girardeau regime, introduced in Sec.II.2.4, was experimentally observed in 2004 by two different groups [7, 8]. Both groups made use of very anisotropic traps in order to obtain quasi 1D tubes. However, they used a different approach to reach the strongly interacting regime.

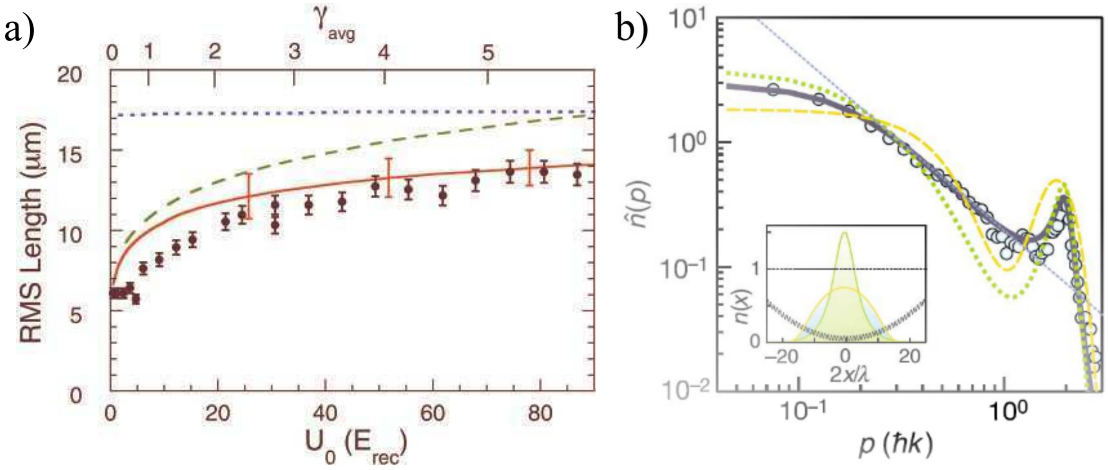

Figure II.12: Experimental observation of the TG gas. a) Increasing the interaction strength g between the particles, the cloud size slowly approaches the predicted value of the TG gas, indicated by the horizontal dotted line. The measured values coincide with the solid curve which represents the expected behavior of the 1D Bose gas theory. The dashed line represents a mean-field calculation. From [7]. b) Momentum distribution of the 1D atomic gas in a optical lattice. The dots represent measured data whereas the lines correspond to the computed momentum distributions. The green dotted line represents ideal bosons, the yellow dashed line represents the ideal Fermi gas and the purple solid line represents the TG gas. Due to the non-uniformity of the TG gas on the lattice, the slope of the linear part in the double logarithmic plot deviates from the expected $1/2$ behavior of the uniform TG gas. From [8].

The Weiss group [7] created a TG gas using a 2D optical lattice (see above), superimposed on a crossed dipole trap. The dipole trap confines the atoms along the tube axis, thus creating an array of almost equal (only differing by particle number) 1D tubes. The average energy per particle and the root mean square full length of the 1D trapped atom cloud were obtained by suddenly turning off the dipole trap and letting the atoms expand ballistically along the tube axis. By changing the lattice trap intensity the dimensionless interaction strength of the Lieb-Liniger model $\gamma = mgL/(\hbar^2 N)$, see Sec.II.2.3, could be tuned and different regimes became accessible. For lattice depths $U_{lat} \geq 20E_r$, with the atom's recoil energy E_r, the total energy of the particles was substantially smaller than in the mean-field prediction whereas the cloud size coincided with the mean-field prediction. This can only be understood if the gas is very dilute and thus contains very few particles per unit length. It is a manifestation of the reduced wave function overlap, which is a clear signature of fermionization. Fig.II.12 a) displays the cloud size and how it slowly converges to its predicted value in the TG regime. However, it should be noted that the maximal $\gamma \backsimeq 5.7$, seen in Fig.II.12 a) is still far

from the TG regime, in agreement with the Lieb-Liniger analysis, see Fig.II.5 a).
In the same year Paredes et al [8] created a TG gas in an optical trap with a periodic confinement along the tube axis. The periodic confinement potential of $V_{pc} = 0 - 18.5E_r$ in axial direction allows to enhance the particle interaction strength by two orders of magnitude, resulting in an effective interaction strength of $\gamma = 0.5 - 500$. In order to avoid a Mott insulating state, the average number of atoms per lattice site was kept smaller than unity. Then the axial momentum distribution of the cloud was probed with the TOF technique, explained above. Comparison of the obtained momentum distribution with numerically calculated curves for a fermionized system make it possible to identify the strongly interacting regime of Tonks and Girardeau. Due to the fact that the TG gas was non-uniform in the lattice, its momentum distribution did not show the characteristic $1/\sqrt{p}$ behavior at small momenta, expected for the uniform TG gas, see Fig.II.12 b). However, with increasing lattice depth the slope of the double logarithmic plot decreased, which is in agreement with what is expected for fermionization. Moreover, its shape was found to differ substantially from the Lorentzian shape expected for a quasi-condensate in the weakly interacting regime.

II.4 Specialized theory

In section II.1 the basic concept of a single particle (ideal bosons) under rotation has been studied. An analogy with the Aharonov-Bohm effect has been pointed out and it was shown that the bosonic single-particle wave function is similar to a Bloch wave function in a crystal. However, in order to be applicable for realistic physical systems the concept needs to be extended by two aspects, missing in Sec.II.1, i.e. particle interactions and a mechanism in order to induce rotation. Including interactions, the effective single-particle problem becomes a many-body problem, described by a more complicated many-body wave function. The spectrum of the interacting problem substantially differs from the one presented in Sec.II.1 and has been analyzed in detail in Refs.[19, 20, 21, 22]. Moreover, in Sec.II.1, it was the additional term mv in Hamiltonian (2.1.1) that accounted for the rotation and no mechanism to induce this rotation was presented. In experiments however, an external driving force as a source of rotation will be needed which will have an influence on the many body wave function of the bosons and hence on the spectrum. In addition, such an external potential

term in the Hamiltonian will allow for the creation of superposition states, so far not accessible [72, 23, 24, 25]. The most obvious effect of the interplay of interactions and the repulsive external potential is the opening of gaps at the true level-crossings in the total energy of Fig.II.1 in section II.1, allowing for a change of angular momentum. It is at these avoided level crossings that interesting physical phenomena will occur.

II.4.1 The combined effect of interactions and rotation

The combined effect of interactions and rotation for bosons on a 1D ring was investigated in a series of publications by Kanamoto et al. [19, 20, 21]. The boundaries of the interaction-rotation control parameter plane over which the system's topological properties change were studied in great detail. As a main result Kanamoto and co-workers introduced the concept of a metastable quantum phase transition (MQPT) occurring at these boundaries. The MQPT is established via the formation of dark soliton trains that bifurcate from the uniform superflow in the weakly interacting regime. In order to obtain a solution for the wave function in this regime one has to solve the nonlinear Gross-Pitaevskii equation (GPE).

$$\left[(-i\frac{\partial}{\partial\theta}-\Omega)^2+g_{1D}N|\psi(\theta)|^2\right]\psi(\theta)=\mu\psi(\theta), \tag{2.4.1}$$

where $\theta = x\ 2\pi/L$ labels the position of the particle on the ring, $\Omega = q\ L/(2\pi)$ is the angular frequency of the rotation and μ the chemical potential. The general solution of Eq.(2.4.1) is given by the condensate wave function (or the order parameter) $\psi(\theta)$ where all the particles are taken to be in the same macroscopic mode. Usually the order parameter is written in terms of density $|\psi(\theta)|$ and phase $\varphi(\theta)$. The concept of BEC is valid due to the fact that the ring is a finite size system and therefore not in contradiction with the absence of BEC in 1D. In the case of $g_{1D} \geq 0$ the condensate wave function is either a plane wave (PW), i.e. it represents a uniform superflow state, or a dark (density suppression) soliton train (ST).

$$\psi_J^{PW}(\theta) = \frac{1}{2\pi}e^{iJ\theta} \tag{2.4.2}$$

$$\psi_{J,j}^{ST}(\theta) = \sqrt{\rho_j(\theta)}e^{i\phi_{J,j}(\theta)}\ , \tag{2.4.3}$$

where $J \in \mathbb{Z}$ is the topological winding number since $\varphi(\theta+2\pi)=\varphi(\theta)+2\pi J$ is required by the single valuedness of the phase. Moreover, $j \in |\mathbb{Z}|$ is the number of density

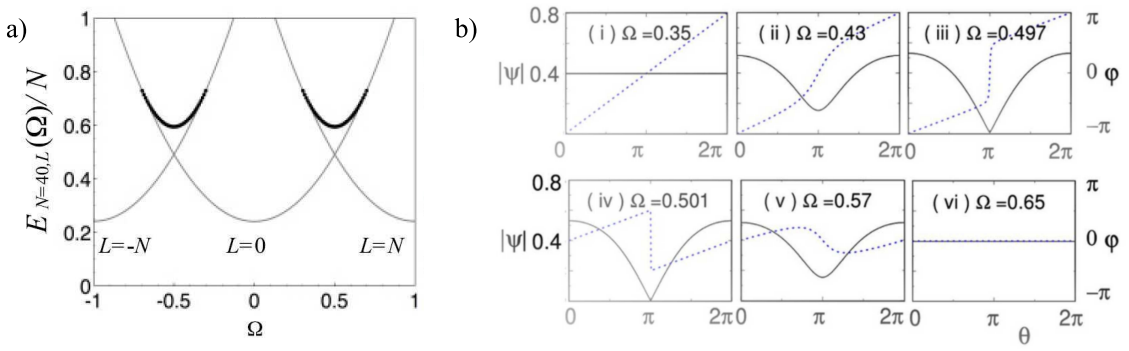

Figure II.13: a) The energy E as a function of the of the angular frequency Ω. The thin curves represent the uniform superflow states with an integral angular momentum $\mathcal{L}_J^{PW}/N = J$ while the soliton (thick curve) with higher energy smoothly connects two uniform superflow states. b) Topological winding and unwinding of the condensate phase. Amplitude $|\psi|$ (solid line) and phase φ (dashed line) of the metastable states of the GPE for $g_{1D}N = 0.6\pi$ (mean-field regime). Uniform superflow with different values of the phase winding (i) $J = 1$ and (vi) $J = 0$ are connected through the soliton solution (ii)-(v). The condensate phase slips at $\Omega = 0.5$. From [22]

notches in the soliton train. The exact derivation of the amplitude $\sqrt{\rho_j(\theta)}$ can be found in Ref. [20]. The soliton solution has a higher energy than the uniform superflow and makes it possible to smoothly connect two uniform superflow solutions with integer angular momentum $\mathcal{L}/N$, $\mathcal{L}$ being the total angular momentum, see Fig.II.13 a). The phase winds exactly at half integer multiples of Ω which correspond to integer multiples of $q = \pi/L$ in section II.1. This bifurcation and the jump of the angular momentum quantum state can be seen in Fig. II.13 b). The angular momentum changes continuously with Ω for the metastable soliton state, whereas it is quantized, $\mathcal{L}_J^{PW}/N = J$ for the plane wave state. Therefore, the interaction and metastability allow for a change of angular momentum which was not possible in the picture of section II.1.

Looking for a correspondence to the dark soliton train for stronger interactions Kanamoto and co-workers studied the problem for arbitrary interaction strength. As it was pointed out in Ref. [55], an identification of the dark soliton trains with the Lieb II excitation mode, see Sec.II.2.3, could be made. It was found that both the dark soliton trains and the Lieb II mode may be described by so-called Yrast states used in nuclear physics [73, 74]. Yrast states are lowest energy states for a given angular momentum. The uniform superflow could then be identified by the center of mass rotation (CMR) states, being a special class of Yrast states with integral angular momentum $\mathcal{L}/N = J$.

The analysis becomes particularly easy in the TG limit. The ground state is obtained

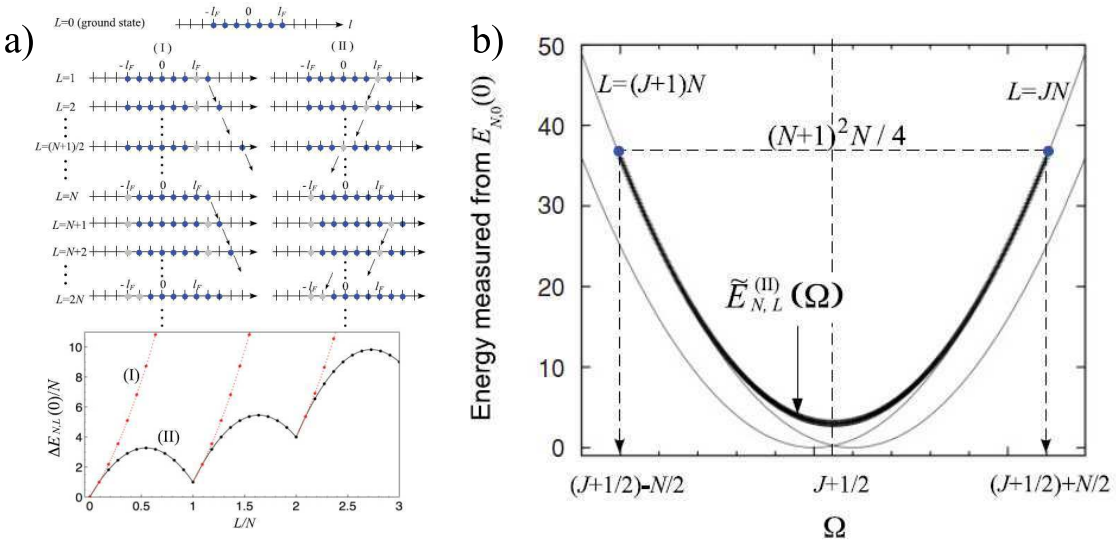

Figure II.14: a) Upper panel: Explanation of the type I and type II excitations. Lower panel: type I and type II excitation energies as a function of $\mathcal{L}/N$. b) Yrast eigenstate spectrum in the TG limit for $N = 11$ particles. The energy is plotted with respect to $E_{N,0}(0)$. The thin curves represent two CMR states with given angular momentum $\mathcal{L} = JN$ and $\mathcal{L} = (J+1)N$, respectively. The bold line that interpolates between the two states of integral angular momentum represents the metastable type II excitations with angular momentum $JN < \mathcal{L} < (J+1)N$. From [21].

by the occupation of the lowest angular momentum states from $l = -l_F ... l_F$, where $l_F = (N-1)/2$ is the Fermi momentum, such that the total angular momentum $\mathcal{L} = 0$, see Fig.II.14 a). The ground state energy is thus given by

$$E_{N,\mathcal{L}=0}(\Omega = 0) = \sum_{-l_F}^{l_F} l^2 = \frac{1}{12} N(N^2 - 1) \ . \tag{2.4.4}$$

The CMR states with angular momentum $\mathcal{L} = JN$ are obtained upon shifting all particles by J quanta of angular momentum, i.e. by occupying the angular momentum states from $l = -l_F + J ... l_F + J$, see again Fig.II.14 a) The energy of of the type II excitation under the effect of the rotation is given by [21]

$$E^{II}_{N,\mathcal{L}}(\Omega) = (N+1)\left[\Omega - \left(J + \frac{1}{2}\right)\right]^2 + \frac{N(N+1)}{4} \ . \tag{2.4.5}$$

Fig.II.14 b) displays both the energy of CMR states with angular momentum $\mathcal{L} = JN$ and $\mathcal{L} = (J+1)N$. The transition between the two CMR states is accomplished by the metastable Lieb II excited state which interpolates between the two branches. The type II branch disappears and merges into the CMR branch at the critical angular frequencies $\Omega^{\mp}_{crit} = (J + 1/2) \mp N/2$.

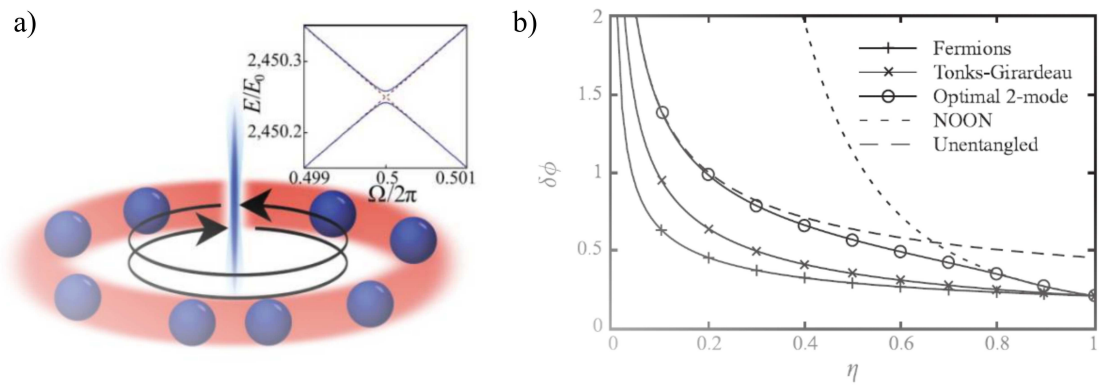

Figure II.15: a) Schematic of the physical system presented in Ref.[23, 25]. Inset: the total energy in units of $E_0 = 2\pi^2\hbar^2/(mL^2)$ of the bosons as a function of the barrier angular velocity Ω for a weak barrier strength. The barrier opens a gap at the true level crossing (dashed line) allowing for a change of the angular momentum state. From [23]. b) Uncertainty of the relative phase $\delta\phi$ depending on the the fraction of particles η not lost due to decoherence processes. The measurement of the phase upon particle loss is most precise for Tonks-Girardeau gas and fermionic atoms whereas the NOON state is sensitive to particle loss. Moreover, particle loss will be more pronounced in the weakly interacting regime such that $\eta \backsimeq 1$ for the TG-gas and free fermions. From [25].

II.4.2 Coupling states through a localized moving barrier potential

The second important ingredient in order to complete the basis of our model is the inclusion of a repulsive external potential, moving around the circumference of the ring trap. Experimentally, this is either realized by a blue detuned laser beam as it was shown in Ref. [16] or it might be done by a rotating optical lattice as it was proposed by [72]. The effect of a moving barrier is an opening of a gap at the level crossings in the spectrum, meaning at half-integer values of Ω, shown in the inset of Fig.II.15 a). The magnitude of the gap depends on the strength of the repulsive barrier. In Ref. [23, 24, 25] Hallwood and co-workers analyzed in detail the barrier as a tunable mechanism in order to change the angular momentum state of the system. With the prospect of realizing a strongly entangled macroscopic superposition of rotating and non-rotating states, they studied the case where the barrier was adiabatically set into motion. At the avoided level crossing $\Omega = 1/2$, an equal superposition of states carrying a total angular momentum $N\hbar$ and states with zero total angular momentum was created

$$|\Psi_B^{\pm}\rangle = \frac{1}{\sqrt{2}}(|\mathcal{L} = N\rangle \pm |\mathcal{L} = 0\rangle) \ . \tag{2.4.6}$$

For weak interactions this superposition is a so-called "NOON"-state, $|\text{NOON}\rangle \propto [(b_0^\dagger)^N + (b_1^\dagger)^N]|vac\rangle$ where all N atoms occupy the same rotating or non-rotating single-particle level, $b_j^\dagger$ being the creation operator of a boson with angular momentum $j\hbar$. As we will show in chapter V, we have found that for strong interactions, each component of the superposition is a Fermi sphere, carrying a total angular momentum of zero and $N\hbar$, respectively.

Ref. [25] proposed a protocol for using this superposition for quantum limited atomic gyroscopes. At a given time an external disturbance will abruptly change the rotation frequency $\Omega \rightarrow 1/2 + \delta\omega$ of the barrier. The system is then allowed to freely evolve for a waiting time $t = t_W$ which establishes a phase difference $\delta\phi = \delta\omega\ t_W$ between the two parts $|\mathcal{L} = N\rangle$ and $|\mathcal{L} = 0\rangle$ of the superposition. This means a mixing between the two states at the avoided level crossing Ψ_B^+ and Ψ_B^- establishes. In order to read out the phase shift $\delta\phi$, the acquired additional rotational frequency $\delta\omega$ needs to be removed such that the barrier moves again at $\Omega = 1/2$. Then the barrier strength is adiabatically ramped down. Once the barrier vanishes, the angular momentum components $|\mathcal{L} = N\rangle$ and $|\mathcal{L} = 0\rangle$ will be detected and the phase shift $\delta\phi$ is measured. The uncertainty for the measurement is limited by the degree of entanglement, i.e. by the Cramer-Rao bound $\delta\phi \geq 1/\sqrt{F_Q}$, F_Q being the quantum Fisher information [75]. In fact, in general it is found that for unentangled particles $F_Q \sim N$, thus recovering shot-noise limit in sensitivity, while $F_Q \sim N^2$ for maximally (usefully) entangled states, yielding Heisenberg limited precision in interferometry [76]. In order to take into account one of the possible decoherence mechanisms, Cooper and co-workers [25] studied the sensitivity of the measurement as a function of particle loss $\eta = N_0/N$, with $N_0 = N - N_{lost}$, for different entangled superposition states, as shown in Fig.II.15 b). It was found that the degree of entanglement for the weakly interacting NOON-state is very sensitive to particle loss whereas free fermions and TG bosons allow for quite robust superpositions, as it can be seen in Fig.II.15 b).

III The system

In this chapter we present the theoretical model studied in this thesis. It consists of interacting bosons confined to a 1D ring under the influence of a rotating external localized potential, taken for simplicity as a delta potential. We use the time-dependent Bose-Fermi mapping to describe the dynamical evolution in the impenetrable-boson (Tonks-Girardeau) limit of infinitely strong interactions between the particles, introduced in Sec.II.2.4. Our solution is compared to the exact solution for the free Bose gas. Our model can be solved exactly for any barrier strength via the solution of a transcendental equation. We gain further insight in the solution by developing a perturbative approach at weak barrier strength. The solution of the many-body wave function allows to access all physical observables of interest. Finally, we discuss the more realistic case of a square barrier potential as an external drive.

III.1 Statement of the problem

We consider N repulsively interacting bosons confined to a 1D ring geometry. The bosons are stirred by a moving repulsive barrier, sketched in Fig.III.1. This barrier is rotating at an angular frequency $\Omega = v/R$, v being the tangential velocity and R the radius of the ring. At $t = 0$ the barrier is supposed to be at rest and localized at position $x = 0$, where $x \in [0, L)$ is the coordinate around the circumference of the ring. At $t = 0^+$ the barrier is set into rotation. In this thesis we consider two possible cases of barrier switching on. The first case is an adiabatic ramping up of the barrier velocity from zero to its final value v. Due to the adiabaticity the system always stays in its ground state. The second case is a sudden quench of the barrier velocity to its final value v. In this latter case the system is brought to a highly excited state which will be studied in detail.

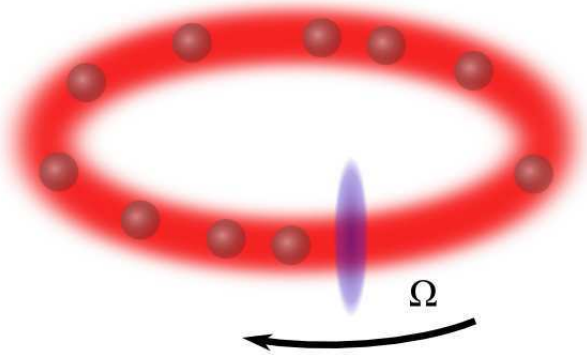

Figure III.1: Sketch of the problem considered: interacting bosons on a 1D ring under the influence of a rotating barrier potential. A ring trap could be created, e.g. by an attractive (red-detuned) laser beam while the barrier could be realized by a repulsive (blue-detuned) laser beam, see Chap. II

III.2 The Hamiltonian

The system is described by the Lieb-Liniger Hamiltonian of Sec.II.2.3 plus the additional time-dependent external potential of the moving barrier,

$$\mathcal{H}_B = \sum_{l=1}^{N} \left[-\frac{\hbar^2}{2m}\frac{\partial^2}{\partial x_l^2} + U_{ext}(x_l,t) + g_{1D}\sum_{j<l}\delta(x_j - x_l) \right] . \tag{3.2.1}$$

The external potential is a contact potential of strength U_0 moving around the circumference of the ring at a constant speed v,

$$U_{ext}(x_l,t) = U_0\delta(x_l - vt) , \tag{3.2.2}$$

and its applicability is discussed in Sec.III.7. Equation (3.2.2) represents the external potential in the stationary regime. In general, there is also a transient regime when the barrier speed is ramped up to its final value v. However, in the two cases discussed in this thesis, i.e. the adiabatic switching on of the barrier motion and the sudden quench. The exact dependence on time of the external potential, i.e. the way the barrier reaches its final velocity, does modify the properties of the system.
In this thesis we are going to solve the time-dependent many-body Schrödinger equation

$$i\hbar\partial_t\Psi_B(x_1,...,x_N,t) = \mathcal{H}_B\Psi_B(x_1,...,x_N,t) . \tag{3.2.3}$$

Due to the presence of an external potential this Schrödinger equation is exactly solvable in only two limits: a) for free bosons, i.e. $g_{1D} = 0$ or b) for the TG gas, i.e. $g_{1D} \longrightarrow \infty$.

In these two limiting cases we calculate the time-dependent wave function of the system allowing us to access the full dynamics of the problem. The study of these limiting cases allows to obtain an estimate for the case of finite interactions between the particles.

III.3 Ideal bosons

In the case of noninteracting bosons all the atoms occupy the same single-particle orbital, see Sec.II.1. The many-body wave function of non-interacting bosons $\Psi_{id}(x_1...x_N,t)$ has a product form

$$\Psi_{id}(x_1...x_N,t)=\prod_{l=1}^{N}\psi_1(x_l,t)\ . \tag{3.3.1}$$

Due to the system's topology, i.e. the ring geometry, we impose periodic boundary conditions for the many-body wave function

$$\Psi_{id}(...x_l...,t)=\Psi_{id}(...x_l+L...,t)\ . \tag{3.3.2}$$

Using Eq. (3.3.1) this implies that each single-particle wave function fulfills PBCs, $\psi_1(x,t)=\psi_1(x+L,t)$. In order that Ψ_{id} satisfies the many-body Schrödinger equation (3.2.3) the single-particle wave function $\psi_1(x,t)$ is chosen to obey the time-dependent single-particle Schrödinger equation

$$i\hbar\partial_t\psi_1(x,t)=\left(-\frac{\hbar^2}{2m}\partial_x^2+U_0\delta(x-vt)\right)\psi_1(x,t)\ . \tag{3.3.3}$$

In order to solve this partial differential equation (second order in space and first order in time), additionally to the boundary condition, an initial condition is needed. As initial condition we choose the ground state of the ideal Bose gas in the presence of a nonmoving barrier localized at $x=0$. This means that at $t=0$ all the particles are in the lowest single-particle orbital $\psi_1(x,0)=\phi_1^{(0)}(x)$ with energy $E_1^{(0)}$.

III.4 The Tonks-Girardeau gas

In the TG regime, corresponding to the impenetrable boson limit $g_{1D}\to\infty$, the interaction potential can be replaced by a cusp condition on the many-body wave function

$$\Psi_{TG}(...x_j=x_\ell...)=0\ . \tag{3.4.1}$$

Moreover, in analogy with ideal bosons in Sec.III.3, the topology of the system demands to impose PBCs for the many-body wave function,

$$\Psi_{TG}(...x_j...) = \Psi_{TG}(...x_j + L...) \tag{3.4.2}$$

for any j. As we have seen in Sec.II.2.4 it is possible to obtain an exact analytical solution for the many-body wave function by mapping the system onto a gas of noninteracting fermions subjected to the same external (time-dependent) potential,

$$\Psi_{TG}(x_1, ...x_N, t) = \mathcal{A}(x_1, ...x_N)(1/\sqrt{N!}) \det[\psi_l(x_m, t)] \tag{3.4.3}$$

with the mapping function

$$\mathcal{A}(x_1, ...x_N) = \prod_{j<\ell} \mathrm{sign}(x_j - x_\ell) \tag{3.4.4}$$

which ensures the bosonic symmetry under exchange of two particles. In each coordinate sector $x_{P(1)} < x_{P(2)} < ... < x_{P(N)}$, where P is a permutation of the set $\{1, 2, ...N\}$, the many-body wave function Eq.(3.4.3) satisfies the required cusp conditions Eq.(3.4.1) and is the unique solution of the many-body time-dependent Schrödinger equation, provided that the orbitals $\psi_l(x, t)$ satisfy the time-dependent single-particle Schrödinger equation

$$i\hbar\partial_t\psi_l(x, t) = \left(-\frac{\hbar^2}{2m}\partial_x^2 + U_0\delta(x - vt)\right)\psi_l(x, t) \ . \tag{3.4.5}$$

In analogy with the ideal Bose gas an initial condition and boundary conditions are needed. Again the single-particle wave function must fulfill PBCs in order to obtain a many-body wave function which obeys PBCs. Moreover, we choose as initial condition for the TG its ground state in the presence of a nonmoving barrier localized at $x = 0$. In the TG limit this corresponds to a Fermi sphere for the mapped Fermi gas built with the orbitals $\psi_l(x, 0) = \phi_l^{(0)}(x)$ for $l = 1...N$, eigenvectors of the stationary Schrödinger equation for a nonmoving barrier, and single-particle energy $E_l^{(0)}$.

III.5 The single-particle Schrödinger equation

In both limiting cases, the ideal bosons in Sec.III.3 and the TG gas in Sec.III.4, the many-body problem has been reduced to a single-particle problem. The single-particle wave

function $\psi_l(x,t)$ must obey the time-dependent single-particle Schrödinger equation (3.4.5), with PBCs and the initial condition

$$\psi_l(x,t=0) = \phi_l^{(0)}(x) \ . \tag{3.5.1}$$

Here, $\phi_l^{(0)}(x)$ is the l-th orbital for a stationary barrier localized at $x=0$. We recall that the particle index is $l=1$ for ideal bosons and $l=1...N$ for the TG gas. In order to find the solution we start by removing the time-dependence from the Hamiltonian by transforming the problem into the co-moving frame. This is done by two unitary transformations

$$\mathcal{U}_1 = e^{-i\hat{p}vt/\hbar} \tag{3.5.2}$$

$$\mathcal{U}_2 = e^{imv\hat{x}/\hbar} \ , \tag{3.5.3}$$

with $\hat{p} = -i\hbar\partial_x$ being the momentum operator and $\hat{x} = x$ being the position operator. Thus $\mathcal{U}_1$ performs a spatial translation by vt and $\mathcal{U}_2$ yields a momentum shift by the barrier momentum $q = mv/\hbar$. The time-dependent state is then obtained as

$$|\psi_l(t)\rangle = \mathcal{U}_1\,\mathcal{U}_2 \sum_j \ c_{jl}\ e^{-i(E_{j,q}-mv^2/2)t/\hbar}|\phi_{j,q}\rangle \ , \tag{3.5.4}$$

such that the solution for the dynamical evolution of the wave function reads

$$\psi_l(x,t) = e^{iqx}e^{-i\hbar q^2 t/2m}\sum_j c_{jl}e^{-iE_{j,q}t/\hbar}\phi_{j,q}(x-vt) \ . \tag{3.5.5}$$

The orbitals $\phi_{j,q}(x)$ and the energies $E_{j,q}$ in Eq. (3.5.5) are obtained from the stationary Schrödinger equation in the frame co-moving with the barrier,

$$\left(-\frac{\hbar^2}{2m}\partial_x^2 + U_0\delta(x)\right)\phi_{j,q} = E_{j,q}\phi_{j,q} \ . \tag{3.5.6}$$

The problem is thus reduced to a time-independent single-particle problem. However, due to the transformation into the co-moving frame the orbitals $\phi_{j,q}(x)$ fulfill twisted boundary conditions (TBCs) instead of PBCs

$$\phi_{j,q}(x+L) = e^{-iqL}\phi_{j,q}(x) \ . \tag{3.5.7}$$

If the barrier is suddenly set into motion, the time-independent overlaps c_{jl} contain the information about the initial condition and are defined as

$$\begin{aligned} c_{jl} &= \langle\phi_{j,q}|e^{-iqx}|\phi_l^{(0)}\rangle \\ &= \int_0^L dx\ e^{-iqx}\ \phi_{j,q}^*(x)\ \phi_l^{(0)}(x) \ . \end{aligned} \tag{3.5.8}$$

If the barrier is adiabatically set into motion the system always stays in the ground manifold and the coefficients read

$$c_{jl} \;=\; \delta_{j,l}\ . \tag{3.5.9}$$

The solution of Eq.(3.5.6), i.e. the orbitals $\phi_{j,q}(x)$, have been obtained in two ways. In Sec.III.5.1 we present an exact solution for arbitrary barrier strength. The orbitals are obtained by expansion with respect to plane waves and the single-particle wave vectors are determined by a transcendental equation which is solved numerically. In this case, the sum in Eq.(3.5.5) is truncated. In Sec.III.5.2 we give the full evolution of the wave function, and specifically the orbitals, perturbatively for weak barrier strengths. In this limit the sum in Eq.(3.5.5) is reduced to two terms and an entirely analytical solution is presented.

III.5.1 The exact solution

The solution of Eq.(3.5.6) is obtained by expansion with respect to plane waves. Together with the TBCs, a proper normalization $\int_{-L/2}^{L/2} dx|\phi_{j,q}(x)| = 1$ for the single-particle orbitals is imposed, together with a cusp condition at the position of the barrier

$$\frac{\partial}{\partial x}\phi^{+}_{j,q}(x)\Big|_0 - \frac{\partial}{\partial x}\phi^{-}_{j,q}(x)\Big|_0 = 2\lambda\phi_{j,q}(0)\ . \tag{3.5.10}$$

Here $\lambda = mU_0/\hbar^2$ is the barrier strength of dimension length^{-1}. Multiplying it by the circumference of the ring L the dimensionless barrier strength λL is the natural parameter to classify the barrier strength. The single-particle orbitals read

$$\phi_{j,q}(x) = \frac{1}{\mathcal{N}_j}\begin{cases} e^{iq\frac{L}{2}}\left(e^{ik_j(x+\frac{L}{2})} + A(k_j,q)\ e^{-ik_j(x+\frac{L}{2})}\right) & x\in[-\frac{L}{2},0) \\ \\ e^{-iq\frac{L}{2}}\left(e^{ik_j(x-\frac{L}{2})} + A(k_j,q)\ e^{-ik_j(x-\frac{L}{2})}\right) & x\in[0,\frac{L}{2}]\ . \end{cases} \tag{3.5.11}$$

The normalization factor

$$\mathcal{N}_j = \sqrt{L(1 + A(k_j,q)^2 + 2A(k_j,q)\sin(k_jL)/k_jL)} \tag{3.5.12}$$

and the amplitude $A(k_j,q) = \sin[(k_j+q)L/2]/\sin[(k_j-q)L/2]$ are functions of the wave vectors k_j given by the solution of the transcendental equation

$$k_j = \lambda\frac{\sin(k_jL)}{\cos(qL)-\cos(k_jL)}\ . \tag{3.5.13}$$

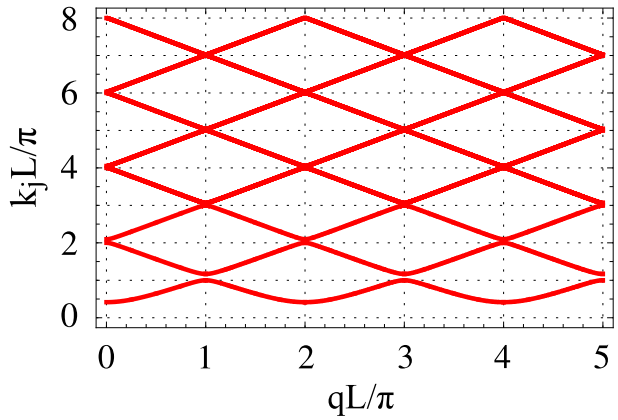

Figure III.2: Single-particle excitation spectrum k_j in units of π/L versus the stirring wave vector (quasi-momentum) q in units of π/L for a barrier strength $\lambda L = 1$. Recalling the description of Sec.II.1, in the absence of the barrier, here the different states of given angular momentum are coupled by the barrier that opens gaps at $q_n = n\pi/L$ and thus allows to change the branch of angular momentum.

The single-particle wave vectors k_j are shown in Fig.III.2 as a function of the barrier momentum q. The corresponding energy eigenvalues $E_j = \hbar^2 k_j^2/2m$ are shown in Fig.III.3. The eigenfunctions $\phi_{j,q}(x)$ in Eq.(3.5.11) form a complete set for $q \neq n\pi/L$, where n is an integer. If $q = n\pi/L$ equation (3.5.11) only yields the spatially even orbitals and the odd orbitals need to be found separately in order to obtain a complete set. This special case is discussed in detail in Appendix A and includes the initial condition, i.e. $n = 0$, where for spatially even orbitals we have

$$\phi_l^{(0)}(x) = \frac{2}{\mathcal{N}_l^{(0)}} \cos[k_l^{(0)}(|x| - L/2)] \tag{3.5.14}$$

with wave vectors fixed by the transcendental equation $k_l^{(0)} \tan(k_l^{(0)} L/2) = mU_0/\hbar^2$ yielding a single-particle energy $E_l^{(0)} = \hbar^2 (k_l^{(0)})^2/2m$. The normalization is given by $\mathcal{N}_l^{(0)} = \sqrt{2L(1 + \sin(k_l^{(0)} L)/k_l^{(0)} L)}$. For odd orbitals we have

$$\phi_l^{(0)}(x) = i(-1)^l \sqrt{\frac{2}{L}} \sin[2\pi l x/L], \tag{3.5.15}$$

with $l = 1, 2, 3...$ integer, and the phase factor in Eq.(3.5.15) has been chosen for consistency with Eq.(3.5.11). A detailed derivation of the orbitals and the single-particle wave vectors can be found in Appendix A. Finally, using Eq.(3.5.11) and respectively Eqs.(3.5.14) and (3.5.15) above, it is possible to find an analytical expression for the

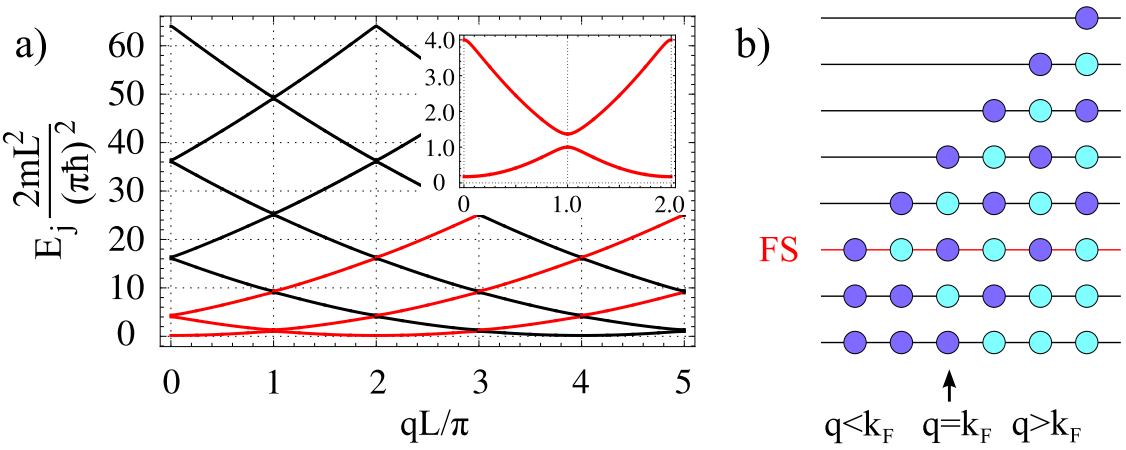

Figure III.3: a) The energy eigenvalues $E_j = \hbar^2 k_j^2/2m$ in units of $(\pi\hbar)^2/(2mL^2)$ as a function of the stirring wave vector q in units of π/L for a barrier strength $\lambda L = 1$. Each parabola represents a state of different angular momentum. The inset shows the first avoided level crossing between the states with zero and one quantum of angular momentum. The red parabolas correspond to the occupied states induced by the out-of-equilibrium drive for the case $N = 3$. b) Schematic of the excited state induced by the out-of-equilibrium drive for $N = 3$ particles. At each avoided level crossing a multiple particle hole excitation is created which at $q = k_F$ leads to a stretched Fermi sphere.

overlap coefficients (3.5.8), which read

$$c^e_{jl} = \frac{L}{\mathcal{N}_j \mathcal{N}^{(0)}_l}\left\{ J_0\left[(k^{(0)}_l - k_j - q)\frac{L}{2}\right] + J_0\left[(k^{(0)}_l + k_j + q)\frac{L}{2}\right] + A_j J_0\left[(k^{(0)}_l + k_j - q)\frac{L}{2}\right] + A_j J_0\left[(k^{(0)}_l - k_j + q)\frac{L}{2}\right]\right\} \quad (3.5.16)$$

for the overlap with an initial even orbital, and

$$c^o_{jl} = \frac{\sqrt{L/2}}{\mathcal{N}_j}\left\{ J_0\left[(\frac{2\pi l}{L} - k_j - q)\frac{L}{2}\right] - J_0\left[(\frac{2\pi l}{L} + k_j + q)\frac{L}{2}\right] + A_j J_0\left[(\frac{2\pi l}{L} + k_j - q)\frac{L}{2}\right] - A_j J_0\left[(\frac{2\pi l}{L} - k_j + q)\frac{L}{2}\right]\right\} \quad (3.5.17)$$

for the overlap with an initial odd orbital, with $J_0(x) = \sin(x)/x$ being the first spherical Bessel function. The creation of highly excited states due to the application of the out-of-equilibrium drive is indicated by the red lines in Fig.III.3a). The schematics Fig.III.3b) reveal that at each avoided level crossing a multiple particle-hole excitation is induced in the system, leading to a stretched Fermi sphere at stirring momenta $q \gtrsim k_F$.

III.5.2 Perturbation theory

In order to develop a qualitative understanding of the behavior of the system under stirring, we study the case of weak barriers, i.e. for a barrier strength $\lambda L \lesssim 1$, where it is possible to obtain the dynamical evolution of the wave function (3.5.5) perturbatively. Due to the ring periodicity the problem of the time-independent Hamiltonian in Eq.(3.5.6) with solutions that obey TBCs is equivalent to the one for a particle in a periodic potential, as we have already pointed out in Sec.II.1. We can therefore expand the solutions of Eq. (3.5.6) in Bloch waves

$$\phi_{j,q}(x) = \frac{e^{-iqx}}{\sqrt{L}} \sum_{p\in\mathbb{Z}} \alpha^{(j)}_{q-2\pi p/L} e^{i2\pi px/L}, \tag{3.5.18}$$

with eigenvalues $E_{j,q}$ and coefficients $\alpha^{(j)}_{q+2\pi p/L}$, j being the band index. Indeed the eigenstates $\phi_{j,q}(x)$ of the Hamiltonian in Eq.(3.5.6) are written as a product of a plane wave $\exp(-iqx)$ and a lattice- (in our case ring-) periodic function and thus obey Bloch's theorem. The parameter q plays the role of the quasi-momentum. It provides a periodic continuous parametric dependence of the states and the energy on the stirring velocity. If the barrier is weak it will only couple two states $2\pi a/L$ and $2\pi b/L$, $a, b \in \mathbb{Z}$ of different angular momentum depending on the concerned avoided level-crossing, see Fig.III.3. Consequently, at fixed avoided level crossings around $q_n = n\pi/L$, n being an odd integer only two elements of the sum in Eq.(3.5.18) contribute and Eq. (3.5.18) reduces to

$$\phi^{(pert)}_{j,q}(x) = \frac{e^{-iqx}}{\sqrt{L}} \left[\alpha^{(j)}_{q-\frac{\pi}{L}(n-j)} e^{i(\frac{\pi}{L}(n-j)x} + \alpha^{(j)}_{q-\frac{\pi}{L}(n+j)} e^{i(\frac{\pi}{L}(n+j)x} \right] \tag{3.5.19}$$

$$\phi^{(pert)}_{j+1,q}(x) = \frac{e^{-iqx}}{\sqrt{L}} \left[\alpha^{(j+1)}_{q-\frac{\pi}{L}(n-j)} e^{i(\frac{\pi}{L}(n-j)x} + \alpha^{(j+1)}_{q-\frac{\pi}{L}(n+j)} e^{i(\frac{\pi}{L}(n+j)x} \right] \tag{3.5.20}$$

for odd values of j. The expansion coefficients $\alpha^{(j)}_{q-2\pi p/L}$ are readily obtained by solution of the effective two-level problem,

$$\alpha^{(j)}_{q-\frac{\pi}{L}(n-j)} = \alpha^{(j+1)}_{q-\frac{\pi}{L}(n+j)} = v^{(j)}_q \tag{3.5.21}$$

$$\alpha^{(j)}_{q-\frac{\pi}{L}(n+j)} = -\alpha^{(j+1)}_{q-\frac{\pi}{L}(n-j)} = -u^{(j)}_q \tag{3.5.22}$$

where

$$\left\{u^{(j)}_q, v^{(j)}_q\right\} = \left[\frac{1}{2} \pm \frac{\frac{\hbar^2}{m}\ \frac{j\pi}{L}\ \delta q}{\sqrt{\left(\frac{2\hbar^2}{m}\ \frac{j\pi}{L}\ \delta q\right)^2 + \left(\frac{2U_0}{L}\right)^2}}\right]^{1/2}, \tag{3.5.23}$$

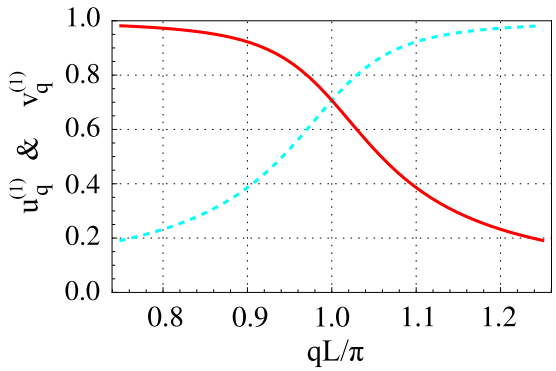

Figure III.4: The expansion coefficients $u_q^{(1)}$ (cyan dashed line) and $v_q^{(1)}$ (red solid line) of the lowest avoided level crossing as a function of q in units of π/L. Adding their squares $(u_q^{(1)})^2 + (v_q^{(1)})^2$, unity is obtained.

the +(-) solution referring to $u_q^{(j)}$ ($v_q^{(j)}$), and we have introduced $\delta q = q - q_n$, the deviation of q from q_n. The coefficients are plotted in Fig.III.4 as a function of q, revealing the proper normalization since $(u_q^{(j)})^2 + (v_q^{(j)})^2 = 1$. Equations (3.5.19) and (3.5.20) also hold for even values of n choosing j even. For even n the first band is in a well defined state of angular momentum and its wave function reads $\phi_{1,q}^{(pert)}(x) = \exp(-iqx)\exp(i\pi nx/L)/\sqrt{L}$.
We finally obtain the full wave function at the avoided level crossing inserting Eq.(3.5.19) and (3.5.20) in Eq.(3.5.5),

$$\psi_l^{(pert)}(x,t) = e^{iqx}e^{-iq^2t/2m}\sum_j{}' \Big(c_{jl}\; e^{iE_{j,q}t/\hbar}\; \phi_{j,q}^{(pert)}(x-vt) + c_{j+1,l}\; e^{iE_{j+1,q}t/\hbar}\; \phi_{j+1,q}^{(pert)}(x-vt)\Big) \quad , \quad (3.5.24)$$

with

$$\{E_{j,q}, E_{j+1,q}\} = \frac{\hbar^2}{2m}\left[(\delta q)^2 + \left(\frac{j\pi}{L}\right)^2\right] \mp \sqrt{\left(\frac{\hbar^2}{m}\,\frac{j\pi}{L}\,\delta q\right)^2 + \left(\frac{U_0}{L}\right)^2} \quad (3.5.25)$$

being the energy of the jth and the $(j+1)$th band. Here the $\sum'$ is over the even j or the odd j only, depending on n. The coefficients c_{jl} are determined using Eq.(3.5.8) where the initial orbitals are plane waves $\phi_l^{(in)} = \exp(ik_lx)/\sqrt{L}$ with $k_l = -\pi(l-1)/L$

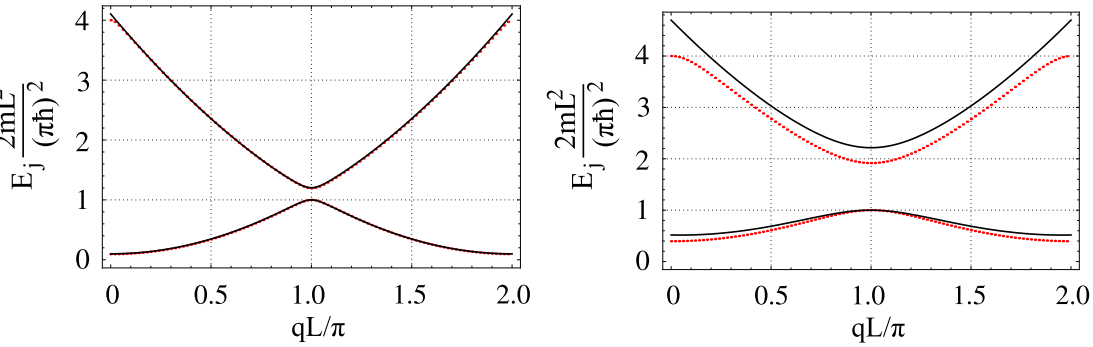

Figure III.5: The energy eigenvalues in units of $(\pi\hbar)^2/(2mL^2)$ as a function of the stirring wave vector q in units of π/L. The dotted red curve represents the exact calculation whereas the solid black line is derived from the perturbative solution. Left panel: A perfect agreement is found between the two solutions for a barrier strength $\lambda L = 0.5$, proving the validity of perturbation theory in the weak barrier limit. Right panel: For a barrier strength $\lambda L = 3$ the perturbative approach deviates from the full solution.

for odd l and $k_l = \pi l/L$ for even l, yielding

$$\begin{aligned} c_{jl} &= v_q^{(j)}\delta_{j,n+l-1} \\ c_{j+1,l} &= u_q^{(j)}\delta_{j,n+l-1} \end{aligned} \quad \text{for} \quad l \text{ odd} \qquad . \tag{3.5.26}$$

$$\begin{aligned} c_{jl} &= v_q^{(j)}\delta_{j,n-l} \\ c_{j+1,l} &= u_q^{(j)}\delta_{j,n-l} \end{aligned} \quad \text{for} \quad l \text{ even}$$

The single-particle energy, obtained from Eq.(3.5.25) for $j = 1$ and $q = \pi/L$ is shown in Fig. III.5 and compared with the single-particle energy obtained from the exact solution in Sec.III.5.1. As expected the perturbative approach deviates significantly from the exact calculation for $\lambda L > 1$.

III.6 The energy bands

With the single-particle energy $E_j = \hbar^2 k_j^2/2m$ shown in Fig.III.3 it is possible to calculate the total energy of the bosons. For ideal bosons, the ground state is obtained if all particles are in the lowest lying orbital $j = 1$. Thus the ground state energy is given by

$$E_{id}^{(0)} = N\frac{\hbar^2 k_1^2}{2m} \; . \tag{3.6.1}$$

For conserved particle number the creation of the first excitation is obtained upon promoting one single boson from the lowest lying state into the next higher orbital.

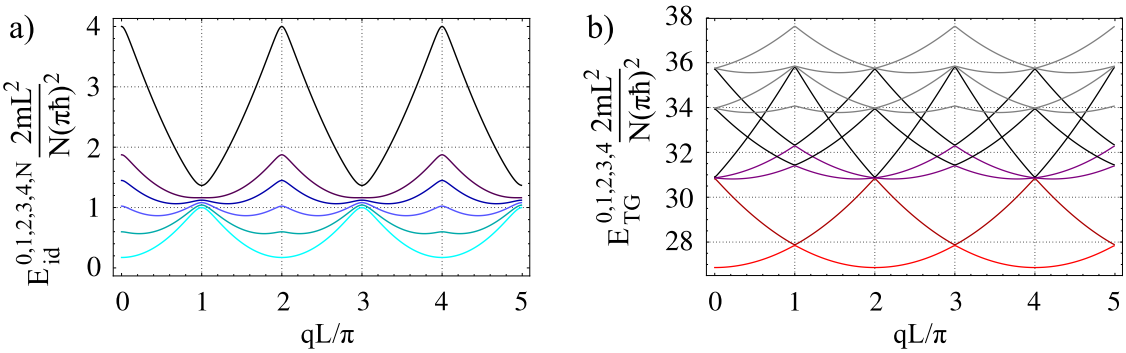

Figure III.6: a) Total energy of the ideal Bose gas E_{id} in units of $N(\pi\hbar)^2/(mL^2)$ as a function of the quasi-momentum q in units of π/L for $N = 9$ bosons. The light blue curve represents the ground state energy followed by the lowest lying excitations from the 1st excited state to the 4th excited state (different blue curves, from light to dark). The black curve represents the Nth excitation, i.e. all particles are promoted into the first excited orbital. b) Total energy of the TG gas E_{TG} in units of $N(\pi\hbar)^2/(mL^2)$ as a function of the quasi-momentum q in units of π/L for $N = 9$ bosons. The light red curve represents the ground state energy and the dark red curve represents the 1st excited state. The second excited state can either be a particle excitation or a hole excitation, represented by the purple curves. They can be distinguished since the hole excitation has lower energy than the particle excitation. All possible 3rd excited states and 4th excited states are represented by the black and gray curves, respectively.

Following this mechanism, any excitation can be created. Fig.III.6 a) shows the total energy for ideal bosons and the energy of the lowest-lying excitations. In the case of the TG gas the creation of excitations becomes somewhat more complicated. The ground state energy is readily obtained upon filling up a Fermi-sea, yielding

$$E_{TG}^{(0)} = \sum_{l=1}^{N} \frac{\hbar^2 k_l^2}{2m} \ . \tag{3.6.2}$$

For conserved particle number there are two possible excitations, i.e. particle-excitations and hole-excitations, that are created by promoting a particle into an empty state above the Fermi level, or creating a hole inside the Fermi-sea. Since there is also the possibility of combining the two different types of excitations there is a variety of higher excitations. In Fig.III.6 b) we show the ground state energy and the energy of the excited states (up to the 4th excitation) as a function of the quasi-momentum q. The first excitation is unique, since in that case the particle excitation coincides with the hole excitation. The second excited state is either a particle excitation or a hole excitation created on the 1st excited state, the particle excitation having an increased energy with respect to the hole excitation. For the third excitation we have the possibility to either create a double particle excitation, a double hole excitation or the combination of a particle and a hole

excitation on the 1st excited state. The higher the excitation, the more possibilities we have to create it. However, for any excitation the pure hole-like excitations give a lower bound on the energy whereas the pure particle-like excitations give an upper bound.

III.7 The square barrier

In a realistic experiment the barrier can be realized by a blue-detuned laser beam, which has of course a finite width. In this section we go beyond the delta barrier model presented in Sec.III.2 by considering a more general case of a square barrier potential. The delta barrier potential is recovered when the width of the barrier tends to zero while the height tends to infinity, keeping the product of height and width constant. We will show that a square barrier potential of width ℓ and height $1/\ell$ of the order of one tenth of the circumference size does not fundamentally change the system's properties, i.e. the particle's wave vectors are only slightly modified compared to the case of a delta barrier potential, thus providing a justification of the delta barrier approach.
We consider the solution of the single-particle Schrödinger equation

$$\left(-\frac{\hbar^2}{2m}\partial_x^2 + U_{barr}(x)\right)\phi_{j,q}^{(s)} = E_{j,q}\phi_{j,q}^{(s)} \ . \tag{3.7.1}$$

with

$$U_{barr}(x) = \begin{cases} U_0^{(s)} & x \in [-\frac{\ell}{2}, \frac{\ell}{2}] \\ \\ 0 & \text{otherwise} \ . \end{cases} \tag{3.7.2}$$

Mathematically, the main difference between a delta barrier potential and the square barrier potential is that the cusp condition in Eq. (3.5.10) for the single-particle wave function is replaced by a continuity condition at the edges of the square barrier, i.e. at $x = \pm\ell/2$. If the single-particle energy $E_{j,q}$ is larger than the barrier potential $U_0^{(s)}$ the solution for the single-particle wave function in the region of the barrier is a plane wave with reduced energy $E_{j,q} - U_0^{(s)}$. If the energy is smaller, then the single-particle wave vector becomes imaginary and an exponentially decaying wave function is obtained. The corresponding transcendental equation reads

$$\frac{2k_j^{(s)}k_j^{(2)}}{(k_j^{(s)} + k_j^{(2)})^2} = \frac{\sin[k_j^{(s)}(L-\ell)]\sin[k_j^{(2)}\ell]}{\cos[(k_j^{(s)} + k_j^{(2)})\ell - k_j^{(s)}L] - \cos[qL]} \ , \tag{3.7.3}$$

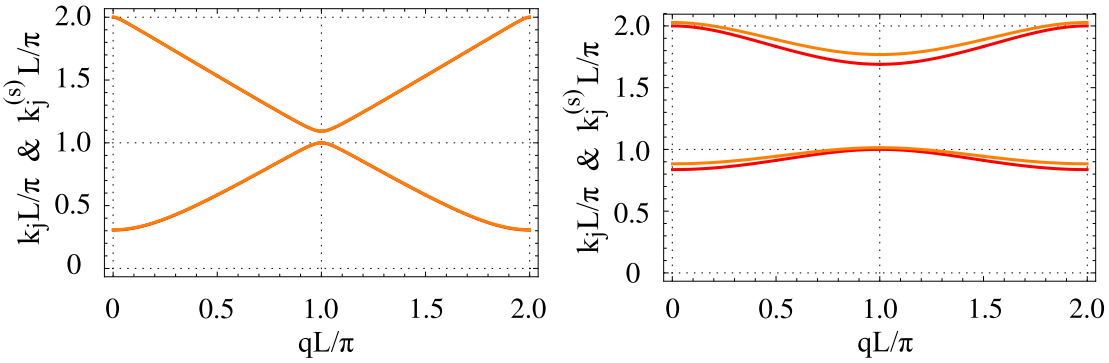

Figure III.7: Single-particle spectrum k_j for a delta barrier and $k_j^{(s)}$ for a square barrier in units of π/L versus the quasi-momentum q in units of π/L for $j = 1, 2$, i.e. the first avoided level-crossing. The red line represents the delta barrier potential and the orange line the square barrier potential. Left panel: a delta barrier potential for $\lambda L = 0.5$ is compared to a square barrier potential of length $\ell = 0.1L$ and barrier strength $\lambda_\ell^{(s)} = 0.5$. No dependence of the single-particle wave vectors on the barrier type is observed. Right panel: a delta barrier potential for $\lambda L = 10$ is compared to a square barrier potential of length $\ell = 0.1L$ and barrier strength $\lambda_\ell^{(s)} = 10$. Between the delta barrier and the square barrier model some deviation is observed in the single-particle wave vector dependence on the quasimomentum.

where $k_j^{(s)}$ and $k_j^{(2)}$ is the single-particle wave vector for $x \neq [-\ell/2, \ell/2]$ and for $x = [-\ell/2, \ell/2]$, respectively. The wave vectors $k_j^{(s)}$ and $k_j^{(2)}$ are not independent, in fact they are linked by the relation

$$k_j^{(2)} = \sqrt{(k_j^{(s)})^2 - 2\lambda^{(s)}} \quad \text{for} \quad (k_j^{(s)})^2 > 2\lambda^{(s)} \tag{3.7.4}$$

$$k_j^{(2)} = i\sqrt{2\lambda^{(s)} - (k_j^{(s)})^2} \quad \text{for} \quad (k_j^{(s)})^2 < 2\lambda^{(s)}\ , \tag{3.7.5}$$

with $\lambda^{(s)} = mU_0^{(s)}/\hbar^2$. Evaluating the transcendental equation, we obtain the wave vector $k_j^{(s)}$ as a function of the quasi-momentum q. The crossover from the weak barrier limit $\lambda^{(s)}\ell L \ll 1$ to the strong barrier limit $\lambda^{(s)}\ell L \gg 1$ both for a delta barrier and a square barrier is displayed in Fig. III.7. The comparison is made by taking the product of length and height of the square barrier equal in magnitude to the delta barrier, i.e. $U_0^{(s)}\ell = U_0$. Since it is most affected by the barrier, we only show the first avoided level crossing in the figures. For weak barriers, no difference between the two types of barriers is observed. However, once the barrier becomes sufficiently strong, i.e. $\lambda L \gg 1$, some deviations are seen. This calculation shows that at intermediate barrier strengths it is necessary to model the exact barrier geometry used in an experiment. At very large barriers, a tunnel model again would be insensible to the details of the barrier. A detailed derivation of the full wave function in the case of the square barrier

potential can be found in Appendix B.

IV Superfluid properties

One of the main motivations for this thesis is the understanding of superfluidity in mesoscopic 1D quantum gases and in particular in the mesoscopic TG gas. In this chapter we recall the fundamental definitions and concepts of superfluidity, i.e. Landau's criterion for superfluidity and the absence of drag-force as well as the Hess-Fairbank effect and the metastability of superflow states. Knowing the exact solution of the many-body wave function derived in the previous chapter, the calculation of the integrated particle current, the particle current fluctuations and the drag force is performed. These physical quantities allow us in turn to address various manifestations of superfluidity in the case of the TG gas and the ideal Bose gas on the 1D ring, respectively. We address both static and dynamic properties and compare them to well-known results given in the literature. Dealing with a mesoscopic system we are further able to distinguish between finite size effects and effects that are visible in the thermodynamic limit.

IV.1 Overview on superfluidity

Since superfluidity has to be understood as an accumulation of several characteristic phenomena its definition is not straightforward. These characteristic phenomena are frictionless flow, the absence of a drag force, quantized circulation and metastable current states. It may very well happen that a system is supposed to be superfluid probing one phenomenon whereas it is non-superfluid looking at another. The phenomenon of superfluidity has been extensively studied in the context of liquid ^{4}He. Placed into a rotating cylinder, the major manifestations of superfluidity in liquid ^{4}He are the Hess-Fairbank effect [77], which is the analog of the Meissner effect in superconductors, and the metastability of superflow states [78]. The Hess-Fairbank effect is an equilibrium property since the fluid stays at rest in a slowly rotating cylinder and therefore in its thermodynamic equilibrium state. In contrast, the metastability of superflow states is a

non-equilibrium property. In a rapidly rotating cylinder the fluid stays in a well defined current state, which is neither the thermodynamic equilibrium state in the laboratory frame nor is it in equilibrium with the rotating cylinder. Therefore the state must be an extremely long-lived metastable state. With the experimental discovery of Bose-Einstein condensation superfluidity became relevant in the context of ultra cold atomic gases. Although, compared to liquids, the latter are extremely rarefied and have a much larger condensate fraction, they display superfluid properties similar to those of liquid ^{4}He. Due to the existence of an order parameter, 3D weakly-interacting BECs show all characteristic phenomena of superfluidity, see e.g. [79]. And indeed, the effect of Bose-Einstein condensation and superfluidity are closely related. The order parameter of the Bose condensate is given by the condensate wave function $\psi = \sqrt{n}e^{i\varphi}$, where the phase φ is similar to the phase in superconductors. If the phase is well defined, the system is in the superfluid state, whereas, if it fluctuates the system does not reveal superfluid properties. The condensate wave function describes the macroscopically occupied ground state and obeys the Gross-Pitaevskii equation. The superfluid velocity can be identified with the gradient of the phase of the order parameter $\vec{v}_s = \hbar\nabla\varphi/m$ and thus ensures the irrotationality of the superfluid [47]. Although BEC and superfluidity are closely related effects, one can exist without the other, giving rise for the hope to find superfluid traces in the 1D regime where BEC does not exist due to the absence of an order parameter.

IV.1.1 Landau's criterion for superfluidity

The first theoretical explanation of superfluidity was given by Landau resulting in Landau's criterion for superfluidity [26]. They considered a liquid moving in a small capillary at a given speed v. If in the frame co-moving with the liquid, the excitation energy is given by $\epsilon(p)$, by using Galileian invariance, in the rest frame of the capillary the excitation energy is given by

$$\epsilon'(p) = \epsilon(p) + \mathbf{p}\cdot\mathbf{v} \ . \tag{4.1.1}$$

Dissipation starts when it becomes then energetically favorable to create excitations in the fluid. i.e. when $\epsilon(p) < 0$. This happens when the momentum of the excitation **p** is antiparallel to the flow velocity **v** and

$$v > \frac{\epsilon}{p} \ . \tag{4.1.2}$$

This is a remarkable result since it states that elementary excitations in the fluid are only possible if the flow velocity exceeds a critical value ϵ/p. The critical velocity v_c of the flow is found by determination of the minimum of ϵ/p. In the case of the quantum liquid considered above the critical velocity is the velocity of sound u_s. If the velocity is smaller than u_s no elementary excitation can be created and the system stays in its ground state. This phenomenon is known under the name of superfluidity. It should be noted that Landau's approach is more general and Eq. (4.1.2) also holds for systems whose low energy excitations differ from the sound modes described in the text.

IV.1.2 Superfluidity in 1D

In recent years, 1D superfluidity has been theoretically studied in various geometries and regimes. In this section we recall important contributions that will help us to place our own contribution in the right frame and to complete the picture of 1D superfluidity. In one dimension the search for superfluid properties becomes particularly interesting due to the presence of strong quantum fluctuations which destroy the BEC. Moreover, in one dimension the presence of a barrier affects the fluid particularly strongly, as particles cannot circumvent it. Both aspects are expected to affect the transport behavior of a one-dimensional (1D) fluid induced by a moving barrier with velocity v. It has been shown that although there is no true long range order, on the time, length and energy scales of realistic experiments superfluid behavior may be detected in some limits. Particularly interesting is the case $K = 1$. In the theory of transport in Luttinger liquids [80] a dramatic change in behavior is expected to occur at this value, known as Schmid transition [81]. This transition can be viewed as a localization-delocalization transition of the relative phase across the barrier: a superfluid has a well-defined, hence localized relative phase, while the insulator has a fluctuating, delocalized phase. Superfluidity is destroyed by quantum or thermal fluctuations which induce phase slips, i.e. jumps of the phase between potential-energy minima.

The effect of finite temperatures was investigated by Kagan et al [27] in the year 2000. In particular, they studied the influence of an impurity moving through a quasi 1D weakly interacting Bose gas, confined to a ring with harmonic trapping potential in the transverse directions. Kagan and co workers found that for temperatures $T \ll 2na_s\omega_\perp$ the decay time of superfluid states becomes very large and by far exceeds experimental times. Thus supercurrent states are very stable during the experiment and superfluidity

is expected in quasi 1D weakly interacting Bose gases at finite temperatures.
The dependence on the trapping geometry has been considered by Büchler et al [10]. Considering a ring geometry, an elongated tube of finite length L and an infinite tube, the effect of a weak link moving through a gas with arbitrary interactions between the particles was studied. In the ring geometry a suppression of quantum phase slips was predicted resulting in a superfluid response of the system to the external perturbation for velocities $v < \hbar\pi/(mL)$. Finite temperatures and large drives of the external potential lead to phase-slips, destroying the superfluid response, confirming the observation of [27] that finite temperatures are harmful for superfluidity. For the infinite tube the Schmid transition [81] is obtained for zero temperature at $K = 1$, leaving the system superfluid for $K > 1$ and non-superfluid for $K < 1$. For $K > 1$ the moving impurity induces phase slips which can be seen in the power law dependence of their nucleation rate $\Gamma_{PS} \propto v^{2K-1}$. Finite temperatures lead to the nucleation of thermally activated phase slips, rendering the system non-superfluid. In the limit of the finite tube, again phase slips lead to a nonsuperfluid behavior. In particular, Bloch oscillations in the chemical potential across the weak link are observed. The results for the infinite tube are recovered for high drives and temperatures.
The dependence on the actual shape of the perturbing potential (obstacle) was investigated by [28, 29] in a system of weakly interacting bosons flowing in a continuous beam. For all kinds of repulsive external potentials a critical velocity smaller than the velocity of sound was found since at the position of the external potential the local fluid velocity is enhanced. The breakdown of superfluidity is linked to the creation of solitons, being the low energy excitations. If the external potential is attractive flow velocities up to the velocity of sound are possible without destroying superfluidity. Differences between the exact shape of the perturbing external potential can however be seen in the supersonic regime, where the drag on the obstacle was calculated.
The stirring of interacting particles on a 1D ring by an external δ-function potential was considered in [30]. Measuring the fraction of stirred particles following a perturbative analysis serves as a probe of the superfluid behavior of the Bose gas. In the weak barrier limit the fraction of stirred particles is found to be a power law of the velocity with the Luttinger parameter $N_{stir}/N \propto v^{2K-2}$ for velocities $v < \hbar\pi/mL$, in agreement with the result found in [10]. In the case of strong interactions this means that ratio N_{stir}/N is constant whereas for weak interactions it tends to zero. In the strong barrier limit $N_{stir}/N \propto 1 - v^{2/K-2}$ is obtained and in the case of strong interactions again the

ratio N_{stir}/N is constant whereas for weak interactions the fraction of stirred particles is increased upon increasing the velocity of the obstacle.

IV.1.3 The drag force as a generalization of Landau's criterion in 1D

A very important quantity enabling to probe the superfluid behavior of a cold atomic gas is the drag force. The drag force F_{drag} is the force exerted by the fluid/gas on an object [31]. This can either be an impurity in the fluid, the walls of a capillary or an external potential. Once this force is nonzero, energy is exchanged between the fluid and the object, leading to transitions in the fluid. The dissipated energy is linked to the drag force via the formula $dE/dt = -F_{drag}v$, where v is the flow velocity.
In 2004 Astrakharchik and Pitaevskii studied the motion of a heavy impurity through a Bose-Einstein condensate at $T = 0$ in dimensions 1,2 and 3 [31]. In the 1D mean-field regime, the drag force on the impurity in an infinite tube was found to be zero and in particular independent of the fluid velocity as long as the fluid velocity is smaller than the velocity of sound u_s. Beyond mean-field, in the case of strong interactions, the drag force was calculated using the knowledge of the dynamic form factor of the system. In the small velocity regime, $v \ll u_s$ a power-law dependence was found,

$$F_{drag} = A(2K)\frac{U_0^2 N^2}{\hbar v L^2}\left(2K\frac{v}{u_s}\right)^{2K} , \tag{4.1.3}$$

where K is the Luttinger parameter and $A(2K)$ is a constant for given K. For weakly interacting Bose gases, i.e. $K \gg 1$, the drag force is vanishingly small for small velocities and the system behaves almost like a 3D superfluid. In contrast, in the strongly interacting regime of Tonks-Girardeau, $K = 1$, the drag force scales linearly with the fluid velocity manifesting the absence of superfluidity in the thermodynamic limit. The behavior of the quantum fluid is then similar to the behavior of a classical fluid, revealing an Ohmic damping behavior.
The effect of temperature was taken into account by Sykes and co-workers [82] probing the superfluidity of a quasi 1D BEC with a delta function impurity moving through it at a constant velocity. They find a non zero drag force at subcritical velocities for all temperatures, different from the results obtained in [31] for $T = 0$. According to their analysis, the finite drag force arises from the scattering of fluctuations and a crossover

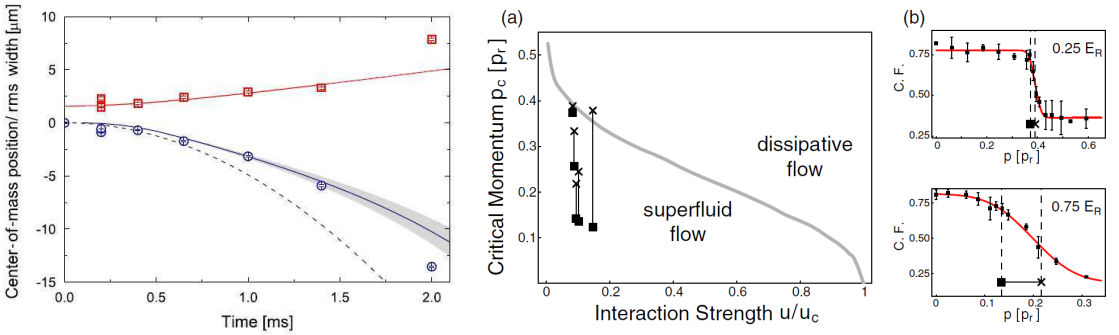

Figure IV.1: Left panel: The non-ballistic motion of the impurity particles due to dissipation as described in the text. The circles show the measured center-of-mass position of the impurity particles and the squares show the increase of the width of the impurity wavepacket for an interaction strength of $\gamma = 7$. The solid line is the prediction according to the theoretical model. The dashed curve indicates the one expected for purely ballistic motion. From [32]. Right panel: (a) Phase diagram for the superfluid to Mott insulator transition as a function of lattice momentum and on-site interaction strength. (b) Condensate fraction as a function of the superflow momentum measured at different lattice depths. The data were fitted with an error function. The squares represent the critical momentum for the transition and the crosses indicate the center of the transition. From [33].

between quantum fluctuations and thermal fluctuations as a source of drag is presented. In a series of papers the 1D Bose gas confined to a ring geometry was studied [83, 84, 85, 86, 87]. The drag force was proposed to be a generalization of the Landau criterion for superfluidity. Besides the critical velocity u_s at which the energy of the impurity suffices to create excited states in the fluid/gas it also accounts for the transition probabilities between the ground state and such an excited state. If the transition probability is largely suppressed the system is supposed to show a superfluid response for flow velocities beyond the critical velocity.

IV.1.4 1D superfluidity in experiments

Due to the fact that it is already challenging to reach the 1D regime, experiments on cold atomic gases do not yet provide quantitative data that allow to address the question of superfluidity. However, most interestingly the propagation of spin impurity atoms through a TG gas in a cigar shaped geometry was studied in [32]. The impurity particles are acceleratd by gravity. Due to dissipation their acceleration is slower than expected, revealing the presence of friction. This is conclusive since due to the strong acceleration, the initially well localized impurity particles reach the speed of sound on a distance shorter than the inter particle distance. A good agreement can be seen for

the center of mass position of the impurity particles between the experimental data and a theoretical model using the 1D drag force, calculated from the dynamic structure factor of the strongly interacting 1D Bose gas, see the left panel of Fig.IV.1. However, it should be noted that the finite mass of the impurity was neglected in the model. Other experiments have investigated the effect of moving optical lattices [88, 33] on a weakly interacting BEC. In [33] the condensate fraction was probed as a function of the lattice depth and momentum, revealing the onset of dissipation at a critical momentum, see the right panel of Fig.IV.1.

IV.2 The time-averaged spatially spatially integrated particle current

The first aspect of superfluidity that we explore is the time-averaged spatially integrated particle current, induced in the system by the rotating barrier. We find a frictionless flow up to a critical velocity (momentum) v_c ($q_c = mv_c/\hbar$) below which no current is induced in the system as predicted by Landau's criterion. As a result of our calculation we find that the qualitative behavior of the particle current depends very much on the type of stirring that is applied, i.e. an adiabatic switching on of the barrier motion or the application of an out-of-equilibrium drive. While in the case of the adiabatic drive a staircase behavior is obtained for the induced current as a function of the stirring momentum, as was predicted in [22], the case of the out-of-equilibrium drive reveals a very peculiar behavior of the current. Only for very special values of the quasi-momentum a non-zero average current is induced in the ring. To our knowledge this behavior has not been predicted in other studies, so far. However, in both cases we obtain the same critical velocity $v_c = \hbar\pi/mL$ in agreement with [10, 30] and we can indeed identify it with the creation of the lowest energy excitation in the system.

IV.2.1 Adiabatic stirring

In the case of an adiabatic stirring mechanism the spatially integrated particle current is readily obtained from the knowledge of the bandstructure. In contrast to the nona-diabatic stirring of the bosons, an adiabatic switching on of the barrier motion leaves the system in its ground manifold $\{k_j\}$ with $j = 1...N$ for the TG-gas and $\{k_1\}$ for the

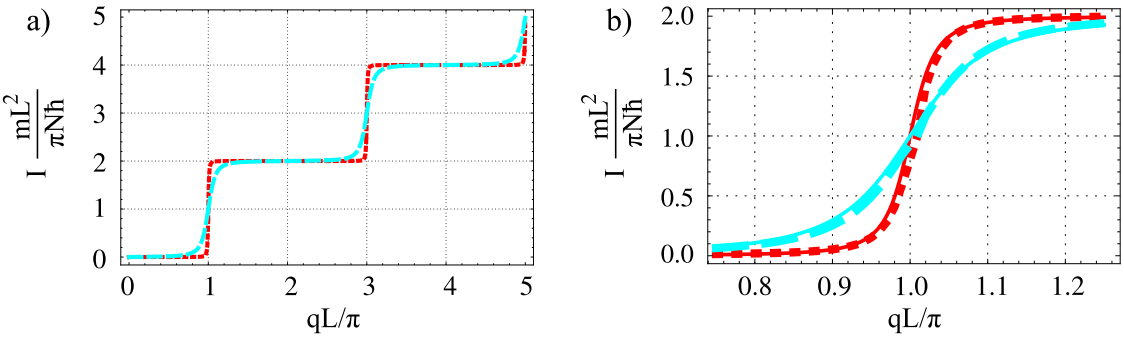

Figure IV.2: The time-averaged, integrated particle current in units of $(\pi N\hbar)/(mL^2)$ for the TG gas (red dotted line) and the ideal Bose gas (cyan dashed line) subjected to the adiabatic stirring described in the text, as a function of the stirring wave vector q in units of π/L, for a barrier strength $\lambda L = 1$ and $N = 9$ particles. The rounding of the current steps is more pronounced in the case of the ideal Bose gas due to the flatter dispersion of the first avoided level crossing. b) Zoom on the 1st step for $N = 3$ particles in order to compare the exact results from Eq.(4.2.10) (dashed lines) to the perturbatively obtained results from Eq.(4.2.11) and (4.2.12) (solid lines).

ideal Bose gas. The corresponding ground state energy $E^{(0)}$ was derived in Sec.III.6 and is given by $E^{(0)}_{TG}(q) = \sum_{j=1}^{N} \hbar^2 k_j^2/2m$ and $E^{(0)}_{id}(q) = N\hbar^2 k_1^2/2m$, respectively. Here we make use of the Hellman-Feynman-theorem [89, 90],

$$\frac{d}{dq}E(q) = \langle\Psi(q)|\frac{d}{dq}H(q)|\Psi(q)\rangle \ , \tag{4.2.4}$$

i.e. the quantum average of the derivative of the Hamiltonian with respect to the stirring momentum $\hbar q$ equals the derivative of the ground state energy with respect to $\hbar q$. Using Hamiltonian (3.2.1) after the transformation $\mathcal{U}_1 = e^{-i\hat{p}vt/\hbar}$ (still in the stationary frame),

$$\mathcal{H}_B(q) = \frac{1}{2m}\sum_l (\hat{p}_l - \hbar q)^2 + U_0\ \delta(x_l) \ , \tag{4.2.5}$$

where $\hat{p}_l = -i\hbar/\ \partial_{x_l}$ is the standard momentum operator we can express the quantum average on the momentum operator in terms of the ground state energy

$$\sum_l \langle\Psi_B|\ \hat{p}_l\ |\Psi_B\rangle = \hbar q - \frac{m}{\hbar}\frac{\partial}{\partial q}E^{(0)}(q) \ . \tag{4.2.6}$$

The particle current density, induced by the rotating barrier, is calculated upon averaging the standard current-density operator

$$\hat{\jmath}(x) = -\frac{i\hbar}{2m}\sum_{l=1}^{N}\left(\delta(x-x_l)\frac{\partial}{\partial x_l} + \frac{\partial}{\partial x_l}\delta(x-x_l)\right) \tag{4.2.7}$$

on the quantum state of the system $\Psi_B(x_1,...x_N,t)$, i.e. $j(x)=\langle\Psi_B|\hat{j}(x)|\Psi_B\rangle$. The particle current density can be written in the form

$$j(x)=\frac{\hbar}{m}N\int dx_1...dx_{N-1}\mathrm{Im}\left[\Psi_B^*(x_1...x_{N-1},x)\frac{\partial}{\partial x}\Psi_B(x_1...x_{N-1},x)\right] \tag{4.2.8}$$

by using Eq.(C.3) of Appendix C. The spatially integrated particle current is obtained upon integrating the current density over space, $I=\frac{1}{L}\int dxj(x)$, and can thus be written in the form

$$I=\frac{N}{Lm}\sum_l\langle\Psi_B|\ \hat{p}_l\ |\Psi_B\rangle\ . \tag{4.2.9}$$

Therefore, the time-averaged integrated particle current for the adiabatic stirring can be obtained from knowledge of the ground state energy by the thermodynamic relation

$$I=\frac{1}{L}\left(N\frac{\hbar q}{m}-\frac{1}{\hbar}\frac{\partial E^{(0)}(q)}{\partial q}\right)\ . \tag{4.2.10}$$

The current has a staircase behavior as a function of the stirring momentum, illustrated in Fig.IV.2. Note that the width of the plateaus of the staircase is $2q_c$ corresponding to the periodicity $2q_c$ found for the ground state energy $E_g(q)$. Since for the ring geometry the current I is proportional to angular momentum, the well-known quantization of angular momentum, introduced in Sec.II.4.1, is observed. The plateaus indicate the metastable superflow states, since the system is in a current-carrying state which is not in equilibrium with the external drive. The resulting critical velocity $v_c=\hbar\pi/mL$ is obtained for the TG gas and the ideal Bose gas, respectively. It coincides with the one predicted in the case of weak interactions [10, 30] suggesting an independence of particle interactions. Moreover, this critical velocity is the analog of the Hess-Fairbank effect, studied for the 1D Bose gas in Ref. [91]. Thus it reveals a superfluid response according to this definition. For weak barriers $\lambda L\leq 1$ we also calculate the integrated time-averaged particle current at the avoided level crossings where a quantum of angular momentum enters the system, i.e. at $q=(2n+1)\pi/L$, using the dispersion obtained from the perturbative analysis of Sec.III.5.2. In the case of the TG gas the perturbatively calculated current reads

$$I_{TG}^{(pert)}=\frac{N\hbar}{mL}\frac{2\pi}{L}\ \left[n+u_q^{(N)}\right] \tag{4.2.11}$$

and for ideal bosons

$$I_{id}^{(pert)}=\frac{N\hbar}{mL}\frac{2\pi}{L}\ \left[n+u_q^{(1)}\right]. \tag{4.2.12}$$

Both curves in Fig.IV.2 show a smearing with respect to the ideal staircase. It is easy to

convince ourself that the ideal staircase behavior is expected in the simplified model of Sec.II.1 where true level crossings occur in the bandstructure. For the ideal Bose gas the smearing is due to the coupling of different states of angular momentum through the external driving potential and its magnitude scales with the barrier strength U_0. In the case of the TG-gas it is due to the combined effect of the coupling and the interactions between the particles. The interactions between the particles lead to the occupation of a Fermi sphere which opens a characteristic gap to the first excited state. Upon increasing the barrier strength the smearing increases until for $\lambda L \gg 1$ the particles cannot circumvent the barrier anymore and only the linear part of the current, i.e. the 1st term in Eq. (4.2.11) and (4.2.12) remains.
A somewhat astonishing feature is that for the ideal Bose gas the width of the jumps is larger, i.e. the smearing of the more pronounced, than the width of the jump for the TG-gas. This apparently surprising result is readily explained by noticing that energetically low lying particles feel the effect of a weak delta-barrier potential more than highly excited states at the Fermi edge.

IV.2.2 Non-adiabatic stirring

In the case of the out-of-equilibrium drive the spatially integrated particle current, induced by the rotating barrier, can be obtained upon evaluating the average of the current-density, $j(x) = \langle \Psi_B | \hat{j}(x) | \Psi_B \rangle$, with the current density operator of Eq.(4.2.7). It turns out that the particle current density can be written in terms of the single-particle wave function of Eq. (3.5.5). In particular it can be shown that the particle current density for the TG gas coincides with the one of the mapped Fermi gas,

$$j_{TG}(x,t) = \frac{\hbar}{m} \mathrm{Im} \sum_{l=1}^{N} \psi_l^*(x,t) \partial_x \psi_l(x,t) \ , \tag{4.2.13}$$

see Appendix C. In the case of the ideal Bose gas the particle current density reads

$$j_{id}(x,t) = \frac{N\hbar}{m} \ \mathrm{Im} \left\{ \psi_1^*(x,t) \partial_x \psi_1(x,t) \right\} \ . \tag{4.2.14}$$

The spatially integrated particle current can thus be written in the form

$$I_{TG}(t) = \frac{N\hbar}{mL}q + \frac{\hbar}{mL}\sum_{l=1}^{N}\left\{-\sum_j |c_{jl}|^2\left(\frac{\partial}{\partial q}\frac{k_j^2}{2}\right) + \mathrm{Im}\sum_{i\neq j} c_{il}^* c_{jl} e^{-i(E_j-E_i)t/\hbar}F_{ij}\right\} \quad (4.2.15)$$

for the TG gas and

$$I_{id}(t) = \frac{N\hbar}{mL}q + \frac{N\hbar}{mL}\left\{-\sum_j |c_{j1}|^2\left(\frac{\partial}{\partial q}\frac{k_j^2}{2}\right) + \mathrm{Im}\sum_{i\neq j} c_{i1}^* c_{j1} e^{-i(E_j-E_i)t/\hbar}F_{ij}\right\} \quad (4.2.16)$$

for the ideal Bose gas. The amplitudes of the last term are given by $F_{ij} = \langle\phi_{i,q}|\partial_x|\phi_{j,q}\rangle$ and in the general case of $q \neq n\pi/L$, where n is an integer, they reduce to

$$F_{ij} = \frac{-ik_ik_jL^2}{\mathcal{N}_i\mathcal{N}_j}J_0[(k_i-k_j)L/2]J_0[(k_i+k_j)L/2] \times \frac{\sin(qL)}{\sin[(k_i-q)L/2]\sin[(k_j-q)L/2]}\ . \quad (4.2.17)$$

Their form at the special points in the wave vector landscape of Fig. III.2, i.e. for barrier momenta $q = n\pi/L$, where n is an integer, is given in Appendix C. The result (4.2.15) for the spatially integrated current displays a time-independent contribution which has the form of a generalized thermodynamic relation $I \propto \partial E/\partial q$ and a time-dependent oscillating term, with several frequency components originating from the multimode nature of the state of the TG gas. For the ideal Bose gas all frequencies but one are suppressed by the coefficients $c_{i1}^* c_{j1}$ since all particles are in the same mode. Here we focus on the time-averaged part of the integrated particle current, the time-dependent contribution will be discussed in detail in Chapter V.

For weak barrier strength $\lambda L \leq 1$ the integrated particle current can be calculated using the perturbative approach of Sec.III.5.2. Close to any level crossing, Eq.(3.5.24) allows to obtain an explicit expression for the integrated particle current,

$$I_{TG}^{(pert)}(t) = \frac{\hbar}{mL}\sum_{l=1}^{N} 4(q_n-k_l)\left(u_q^{(f_{nl})}v_q^{(f_{nl})}\right)^2\left[1-\cos(2\Delta E_q^{(f_{nl})}t)\right] \quad (4.2.18)$$

and

$$I_{id}^{(pert)}(t) = \frac{N\hbar}{mL}\ 4\ q_n\ \left(u_q^{(f_{n1})}v_q^{(f_{n1})}\right)^2\left[1-\cos(2\Delta E_q^{(f_{n1})}t)\right], \quad (4.2.19)$$

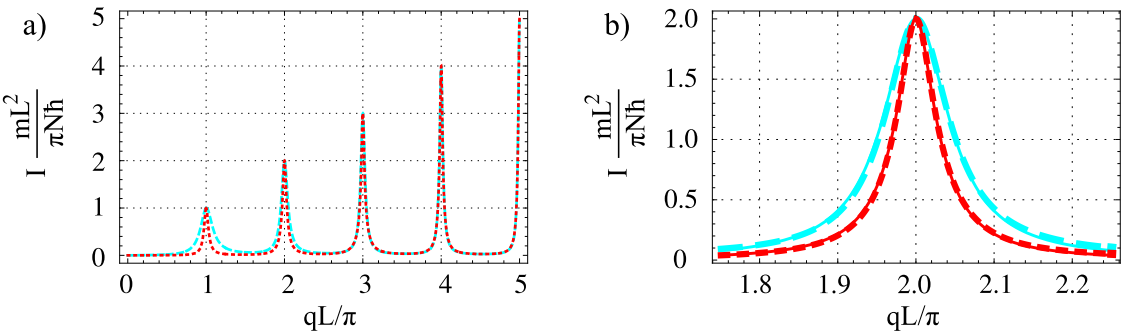

Figure IV.3: a) The time-averaged, integrated particle current in units of $(\pi N\hbar)/(mL^2)$ and for a TG gas (red dotted line) and a noninteracting Bose gas (cyan dashed line) subjected to the non-adiabatic stirring described in the text, as a function of the stirring wave vector q in units of π/L, for a barrier weak strength $\lambda L = 1$ and $N = 3$ particles. b) A zoom on the 2nd current peak. Good agreement is found between the exact calculation (dashed lines) and the results obtained from equation (4.2.18) in the perturbative approach (solid lines).

where we introduced

$$f_{nl} = \begin{cases} |n-l| & \text{for} \quad l \text{ even} \\ (n+l-1) & \text{for} \quad l \text{ odd} \end{cases} . \tag{4.2.20}$$

Here $\Delta E_q^{(l)} = E_{l+1,q} - E_{l,q}$ is the energy splitting of the effective two-level system that governs the time dependence of the current. If averaged over sufficiently long times $t_{av} \gtrsim \hbar/\Delta E_q$, this dependence vanishes.

In Fig.IV.3 we illustrate the resulting time-averaged current for a weak barrier. We find that it displays a narrow maximum for values of the stirring momentum q_n that are equal to integer multiples of $q_c = \pi/L$ corresponding to a critical stirring velocity $v_c = \pi\hbar/mL$. This maximum is well captured in the perturbative approach by the combination $\left(u_q^{(f_{nl})} v_q^{(f_{nl})}\right)^2$, for an illustration of the expansion coefficients $u_q^{(1)}$ and $v_q^{(1)}$ see Fig.III.4. The critical velocity equals the one obtained by adiabatically stirring the particles. The figure shows that it is difficult to stir the mesoscopic TG gas except at velocities that are multiples of v_c. At generic values of the stirring momentum away from q_n the fluid belongs to the zero current branch, which for nonadiabatic stirring momenta $q > q_c$ corresponds to an excited state. The occupation of such highly excited states is due to the instantaneous switching on of the barrier motion and can be seen in Fig.III.2. At the special values of the stirring momentum q_n avoided crossings between single-particle branches with different angular momentum occur. This allows for the occurrence of superpositions of states with different angular momentum which yield a non zero average current. These superpositions are explained in detail in Chapter V.

Figure IV.3 also shows the corresponding time-averaged current of an ideal Bose gas subjected to the same stirring drive. For momenta close to q_n we find that the current induced in an ideal Bose gas is larger than the one of the strongly interacting TG gas. The explanation is the same as in the case of the equilibrium drive. The ideal Bose gas occupies the lowest single-particle level which is most affected by a weak delta-barrier potential. This can also be seen from the fact that $u_q^{(1)}$ and $v_q^{(1)}$ show a very smooth dependence on q, see Fig.III.4. For large stirring momenta $q \gg \hbar k_F$ this effect vanishes since then also the ideal Bose gas is in a very highly excited state. Therefore, the effect of the interactions, which is seen for arbitrary stirring momenta in adiabatic particle current is not observable for large stirring momenta $q > k_F$ in the non-adiabatic current. In Fig.IV.3 panel b) we show that a very good agreement is found at weak barrier strength between perturbation theory and exact calculation for momenta close to q_n. As in the case of the equilibrium drive, for large barriers $\lambda L \gg 1$ only the linear part of the current remains.

Finally, we remark that in the thermodynamic limit, L tending to infinity keeping N/L constant, the critical velocity v_c tends to zero. The observed superfluid effect is truly mesoscopic, i.e. associated with the finite size of the ring. Current experimental realizations of ring traps have a diameter $d \simeq 40\mu$m, resulting in a critical velocity of $v_c \simeq 0.1$mm/s. New experiments on ring traps promise to further reduce the size by an order of magnitude, resulting in a critical velocity of approximately $v_c \simeq 1$mm/s, thus generating an amazing playground for the detection of superfluidity in cold atomic gases.

IV.3 The correlations

To further explore superfluid behavior, we complement the study of the integrated particle current by analyzing its correlations and its fluctuations. The analysis of the correlations allows us to determine if the measured current on the ring at a given position x and a given time t depends on the current measured at another position x' and time t'. The correlations are needed in order to calculate the current fluctuations in the system. The analysis of the fluctuations, i.e. the quantum noise of the system, gives a measure of how well defined the integrated particle current in the previous section is. It is therefore a necessary quantity to know in order to make statements about

superfluidity which requires zero current below the critical velocity. The fluctuations are of pure quantum nature since our model is a zero temperature model and no thermally excited states occur. The analysis of the current fluctuations confirms the findings of the previous section, establishing further the superfluid response of the 1D Bose gas below the critical velocity v_c.

IV.3.1 The current-current correlation function

The strongly non-classical behavior of the particle current in the previous section suggests to study correlations in order to understand the peculiar behavior of the system. The spatially integrated equal-times current-current correlation function is defined as

$$C_2(x,y,t) = \langle \Psi_B | \hat{j}(x,t)\hat{j}(y,t) | \Psi_B \rangle \ , \tag{4.3.1}$$

with the current density operator from Eq.(4.2.7). Evaluating the average on the quantum state of the system the correlation function can be written in term of the single-particle wave functions. For the TG gas it becomes

$$\begin{aligned} C_2^{(TG)}(x,y,t) = \left(\frac{\hbar}{m}\right)^2 \Bigg\{ & \sum_{k=1}^{N} \left(\frac{\partial}{\partial x}\psi_k^*(x)\right)\left(\frac{\partial}{\partial x}\psi_k(x)\right) \\ & - \sum_{k,l=1}^{N} \Bigg[\psi_k^*(x)\left(\frac{\partial}{\partial x}\psi_k(x)\right)\psi_l^*(y)\left(\frac{\partial}{\partial y}\psi_l(y)\right) \\ & - \psi_k^*(x)\left(\frac{\partial}{\partial x}\psi_l(x)\right)\psi_l^*(y)\left(\frac{\partial}{\partial y}\psi_k(y)\right)\Bigg]\Bigg\} \end{aligned} \tag{4.3.2}$$

and for the ideal Bose gas

$$\begin{aligned} C_2^{(id)}(x,y,t) = \left(\frac{\hbar}{m}\right)^2 \Bigg\{ & \left(\frac{\partial}{\partial x}\psi_1^*(x)\right)\left(\frac{\partial}{\partial x}\psi_1(x)\right) \\ & - N(N-1)\psi_1^*(x)\left(\frac{\partial}{\partial x}\psi_1(x)\right)\psi_1^*(y)\left(\frac{\partial}{\partial y}\psi_1(y)\right)\Bigg\} \ . \end{aligned} \tag{4.3.3}$$

The information about the correlations is hidden in the last term of Eq.(4.3.2). The equal-times current-current correlation function for the case of the TG gas is shown in Fig.IV.4 for three different times.

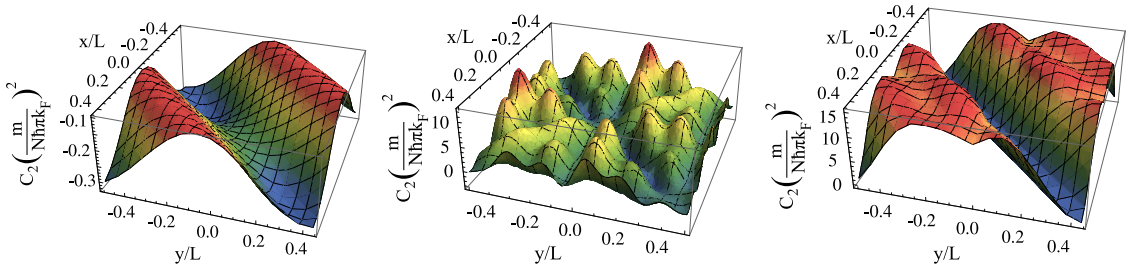

Figure IV.4: The particle current-current correlation function of the TG gas $C_2^{(TG)}(x,y,t)$ in units of $(N\hbar\pi k_F/m)^2$, k_F for $N=3$ particles and a barrier strength $\lambda L=1$ for the out-of-equilibrium drive. The three correlation functions are evaluated at different times for three different times $t=0$, $t=2.5t_0$ and $t=5t_0$ from left to right, with natural time-scale $t_0=mL^2/\pi\hbar$.

IV.3.2 The fluctuations

In order to extract information from the correlation function, useful to explore the peculiar superfluid behavior of the bosons, we calculate the current fluctuations. This quantity measures how well defined the particle current is with respect to unavoidable quantum fluctuations. Therefore it complements the study of the integrated particle current and allows to make a first statement about the superfluid behavior of the 1D Bose gas on a ring. The time-averaged particle current fluctuations are defined as

$$\Delta I = \sqrt{\langle I^2\rangle - \langle I\rangle^2}\,, \tag{4.3.4}$$

where the time-averaged integrated particle current is given by $\langle I\rangle = 1/T\int dt I(t)$. The second moment of particle current is readily obtained upon knowledge of the correlation function

$$\langle I^2\rangle = \frac{1}{L^2}\frac{1}{T}\int_{-T/2}^{T/2}\int_{-L/2}^{L/2} dxdy\; C_2(x,y,t)\;. \tag{4.3.5}$$

With the time-averaged integrated particle current from the previous section, Eq.(4.2.15) and (4.2.16) the square of the fluctuations for the TG gas for the out-of-equilibrium

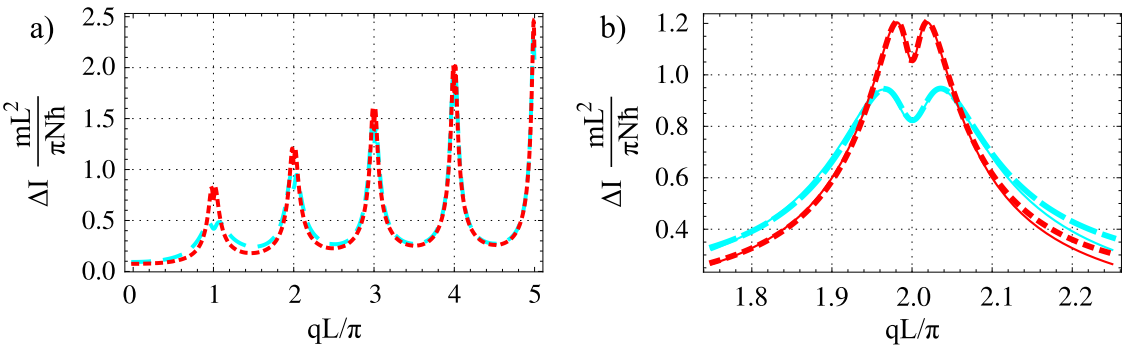

Figure IV.5: a) Time-averaged, integrated particle current fluctuations in units of $(N\hbar k_F)/(mL)$, k_F being the initial wave vector of the Nth particle, for a TG gas (red dotted line) and a noninteracting Bose gas (cyan dashed line) subjected to the nonadiabatic stirring described in the text, as a function of the stirring wave vector q in units of π/L, for a barrier strength $\lambda L = 1$ and $N = 3$ particles. b) Zoom on the second current fluctuation peak. The numerical results are compared with the results of the perturbative approach (thin solid lines).

drive reads

$$(\Delta I)^2_{TG} = \left(\frac{\hbar}{Lm}\right)^2 \left\{ \sum_{k=1}^{N} \sum_j |c_{jk}|^2 \left[q^2 - 2q \left(\frac{\partial}{\partial q} \frac{k_j^2}{2} \right) - \mathcal{F}_{jj} \right] \right.$$
$$\sum_{k,l=1}^{N} \sum_{ij} c^*_{ik} c_{il} c^*_{jl} c_{jk} \left[-q^2 + q \left(\frac{\partial}{\partial q} \frac{k_i^2 + k_j^2}{2} \right) - \left(\frac{\partial}{\partial q} \frac{k_i^2}{2} \right) \left(\frac{\partial}{\partial q} \frac{k_j^2}{2} \right) \right]$$
$$\left. + \sum_{k,l=1}^{N} \sum_{\substack{ij \\ i \neq j}} |c_{ik}|^2 |c_{jl}|^2 F_{ij}^2 \right\} \quad (4.3.6)$$

and

$$(\Delta I)^2_{id} = N \left(\frac{\hbar}{Lm}\right)^2 \left\{ \sum_j |c_{j1}|^2 (-\mathcal{F}_{jj}) \right.$$
$$\left. - \sum_{ij} |c_{i1}|^2 |c_{j1}|^2 \left(\frac{\partial}{\partial q} \frac{k_i^2}{2} \right) \left(\frac{\partial}{\partial q} \frac{k_j^2}{2} \right) + \sum_{\substack{ij \\ i \neq j}} |c_{i1}|^2 |c_{j1}|^2 F_{ij}^2 \right\} \quad (4.3.7)$$

in the case of the ideal Bose gas. The new amplitudes $\mathcal{F}_{ij}$, not to be confused with the F_{ij} are given by $\mathcal{F}_{ij} = \langle \phi_{i,q} | \partial_x^2 | \phi_{j,q} \rangle$ and in the general case of $q \neq n\pi/L$, where n

is an integer, they reduce to

$$\begin{aligned}\mathcal{F}_{ij} = &\frac{-k_i k_j L}{\mathcal{N}_i \mathcal{N}_j \sin[(k_i-q)L/2]\sin[(k_j-q)L/2]} \\ &\times \Big[\cos[(k_i-k_j)L/2]\left(J_0[(k_i-k_j)L/2] - \cos[qL]J_0[(k_i+k_j)L/2]\right) \\ &+ \cos[(k_i+k_j)L/2]\left(J_0[(k_i+k_j)L/2] - \cos[qL]J_0[(k_i-k_j)L/2]\right)\Big] \ . \quad (4.3.8)\end{aligned}$$

In the weak barrier limit the particle current fluctuations can again be derived from the perturbative approach. For the TG gas under the influence of the non-adiabatic drive they read

$$\left(\Delta I^{(pert)}\right)^2_{TG} = \left(\frac{2\hbar}{mL}\right)^2 \sum_{l=1}^{N} 2(q_n - k_l)^2 \left(u_q^{(f_{nl})} v_q^{(f_{nl})}\right)^2 \left[1 - 3\left(u_q^{(f_{nl})} v_q^{(f_{nl})}\right)^2\right] \quad (4.3.9)$$

and for the ideal Bose gas

$$\left(\Delta I^{(pert)}\right)^2_{id} = \left(\frac{2\hbar}{mL}\right)^2 2N q_n^2 \left(u_q^{(f_{nl})} v_q^{(f_{nl})}\right)^2 \left[1 - 3\left(u_q^{(f_{nl})} v_q^{(f_{nl})}\right)^2\right] . \quad (4.3.10)$$

Fig.IV.5 shows the time-averaged particle current fluctuations for a non-adiabatic stirring. For stirring momenta far away from q_n the qualitative behavior of the fluctuations is similar to the one of the current itself. Consequently in the superfluid regime, away from q_n there is neither an induced current nor strong current fluctuations. The quantum state of the system corresponds to a well-defined angular momentum state which explains the smallness of the fluctuations. The calculation confirms what we have already anticipated in the previous section. For stirring momenta $q < q_c$ both the ideal Bose gas and the TG gas show a superfluid response to the external perturbation of the moving barrier. On the other hand, around the current peaks, i.e. for stirring momenta q_n, we observe strong fluctuations. At these special points, the system oscillates between two equally possible angular momentum states, leading to the appearance of strong current fluctuations. At q_n we further observe the formation of a dip in the fluctuations, which can be understood qualitatively as follows. The nonadiabatic current in perturbation theory is given by the weight combination $u_q^{(l)} v_q^{(l)}$ (see Fig.III.4), a structure similar to the *second* cumulant characteristic for the partition noise for particles tunneling across a barrier [92]. Its fluctuations are consequently given by the *fourth* cumulant of the same distribution which gives these splitted peak structures. In order to make precise statements about the meaning of the current the ratio of noise over

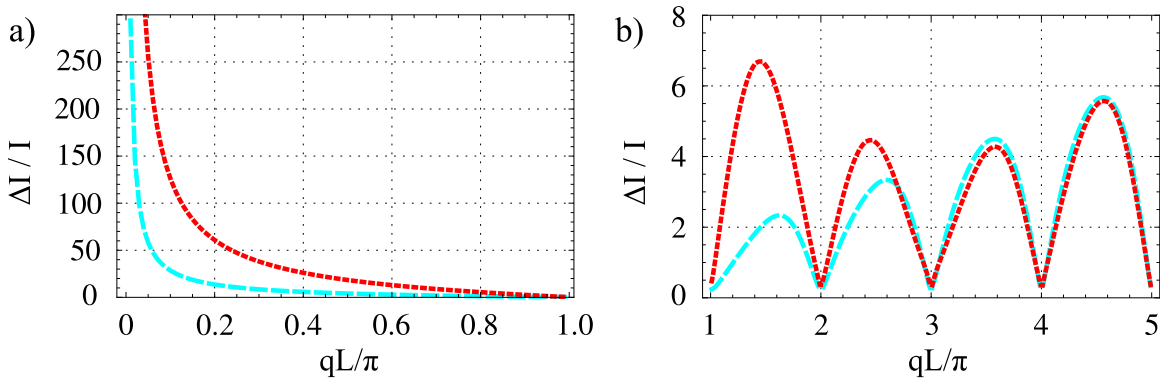

Figure IV.6: The ratio of current fluctuations over the current as a function of the barrier momentum q in units of π/L. At maximum current and fluctuations, i.e. interger multiples of π/L, the current is larger than its fluctuations and hence a well defined quantity. Off resonance the current induced by the out-of-equilibrium drive is negligible and hence the quantum fluctuations dominate the ratio. The large values of the ratio for $q < \pi/L$ are due to the effect of superfluidity.

signal, i.e. $\Delta I/I$ is needed. Fig.IV.6 displays this ratio which allows to quantify the fluctuations around the current peaks with respect to the current itself. At the maximal current values the ration noise over signal is always smaller than unity which means that the particle current fluctuations are smaller than the current itself. In between the current peaks the noise is stronger than the signal which is due to the fact that in these regions the current tends to (almost) zero. This effect becomes obvious for small barrier velocities when no current is induced in the ring while quantum fluctuations are present and the ratio diverges, see Fig.IV.6 a).

In contrast to that the time-averaged particle current fluctuations for the equilibrium drive have a very different shape. Focussing on the odd avoided level crossings, i.e. $q = (2n+1)\pi/L$ the perturbative approach allows us to derive them for both the TG gas

$$\left(\Delta I_{eq}^{(pert)}\right)^2_{TG} = \left(\frac{\hbar}{mL}\right)^2 \left(\frac{2\pi}{L}\right)^2 N \left(u_q^{(N)} v_q^{(N)}\right)^2 \tag{4.3.11}$$

and the ideal Bose gas

$$\left(\Delta I_{eq}^{(pert)}\right)^2_{id} = \left(\frac{\hbar}{mL}\right)^2 \left(\frac{2\pi}{L}\right)^2 N \left(u_q^{(1)} v_q^{(1)}\right)^2 . \tag{4.3.12}$$

Looking at Eq. (4.3.11) and (4.3.12) we observe an interesting feature. The fluctuations are peaked around the odd q_n, which can be seen by the factor $\left(u_q^{(1)} v_q^{(1)}\right)^2$, in the same way as the non-adiabatic particle current is, see Eq. (4.2.18) and (4.2.19) leading to a qualitative behavior as seen in Fig.IV.7. In particular, the fluctuations are

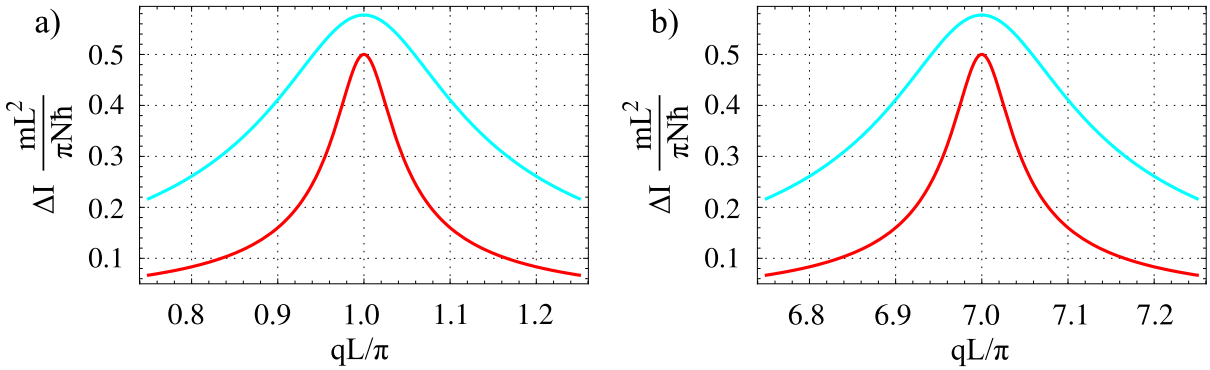

Figure IV.7: Time-averaged, integrated particle current fluctuations obtained from the perturbative formulas Eq.(4.3.9) and (4.3.10) in units of $(N\hbar k_F)/(mL)$, k_F being the initial wave vector of the Nth particle, for a TG gas (red line) and a noninteracting Bose gas (cyan line) subjected to the adiabatic stirring described in the text, as a function of the stirring wave vector q in units of π/L around q_n, for a) $n = 1$ and b) $n = 7$. The barrier strength $\lambda L = 1$ and $N = 3$ particles.

independent of n, meaning that they have exactly the same shape for all peaks. This can be explained by the fact that for the adiabatic stirring the same amount of angular momentum enters into the system at odd q_n, whereas due to the zero current state this is not the case for the out-of-equilibrium drive. The system does not know how many quanta of angular momentum it contains and therefore the same amount of noise is seen for all q_n, i.e. upon the entry of another quantum.

IV.4 The drag force

We finally turn our attention to the study of the drag force, introduced in Sec.IV.4 which quantifies dynamical, complementary, aspects of superfluidity. Being a dynamical property, the drag force is only well defined in the case of the out-of-equilibrium drive. The drag force acting on a barrier potential $V_{barr}(x)$ is defined as $F_{Drag} = -\langle \partial_x V_{barr}(x) \rangle$ where $\langle ... \rangle$ denotes the quantum average with respect to the state of the system. In Ref. [31] this quantity was used to explore superfluid behavior of a 1D Bose gas in an infinite wire. Qualitative differences are found for the case of a mesoscopic ring confirming the critical velocity found in our analysis of the time-averaged integrated particle current. Moreover, qualitative similarities between the TG gas and the ideal Bose gas are found, again in agreement with the already presented results.
For the specific case of a delta barrier potential $U_0\delta(x)$ the drag force is simply related

to the particle density profile $n(x)$, according to

$$F_{Drag} = U_0 \frac{1}{2}[\partial_x n(x)|_{x=0^+} + \partial_x n(x)|_{x=0^-}]. \tag{4.4.1}$$

For a TG gas the density profile is readily calculated within our exactly solvable model, as it coincides with the one of a noninteracting Fermi gas,

$$n(x,t) = \sum_{l=1}^{N} |\psi_l(x,t)|^2 \ . \tag{4.4.2}$$

For the ideal Bose gas the density profile reads

$$n(x,t) = N|\psi_1(x,t)|^2 \ . \tag{4.4.3}$$

The expression for the drag force acting on a delta barrier potential suddenly set into motion across a TG gas in perturbation theory reads

$$(F_{Drag})_{TG}^{(pert)} = \frac{4U_0}{L} \sum_{l=1}^{N} (q_n - k_l) \left(u_q^{(f_{nl})} v_q^{(f_{nl})}\right)^2 \sin(2\Delta E_q^{(f_{nl})} t) \tag{4.4.4}$$

and for the ideal Bose gas

$$(F_{Drag})_{id}^{(pert)} = \frac{4U_0}{L} q_n \left(u_q^{(1)} v_q^{(1)}\right)^2 \sin(2\Delta E_q^{(1)} t) \, . \tag{4.4.5}$$

Fig.IV.8 shows the drag force obtained from both the exact model using the above definition and Eq. (3.5.5) and from perturbation expansion at weak barrier strength using Eq. (4.4.4) and (4.4.5). It is an oscillating function of time with a typical frequency associated with the energy-eigenvalues separations $\Delta E_q^{(l)}$. Notice that since the energy levels depend on the stirring momentum the typical oscillation frequency is also momentum dependent. We find that the behavior of the drag force closely follows the results for the integrated current presented in Sec.IV.2.

In the case of $q < q_c$ the drag force is vanishingly small, confirming the picture of a superfluid mesoscopic TG gas. If the barrier momentum is instead chosen close or equal to q_c, then it is possible to transfer angular momentum to the fluid and the drag force is nonvanishing, illustrating the breakdown of superfluidity. We find the same velocity threshold as the one predicted in our analysis of the particle current and in Ref. [10, 30] using a Luttinger-liquid description of a weakly interacting Bose gas. Finally, for momenta larger than q_c except at the special momenta close to integer multiples of q_c, we find that the drag force vanishes as the system is in a very peculiar, highly excited

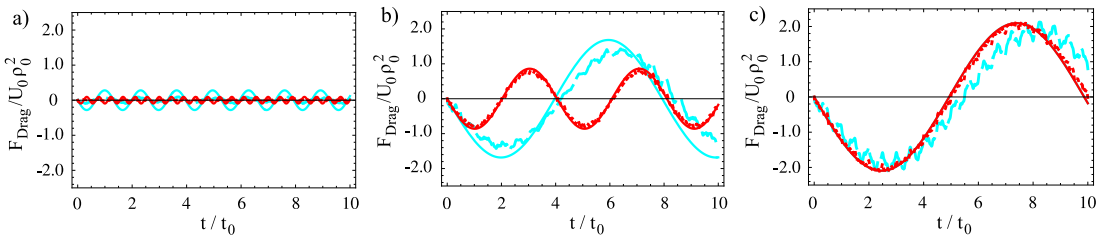

Figure IV.8: The drag force exerted by the fluid on the moving barrier in units of $U_0\rho_0^2$, $\rho_0 = N/L$ being the average density of the fluid, as a function of time in units of $t_0 = mL^2/\pi\hbar$ for a TG gas (red dotted curves) and an ideal Bose gas (cyan dashed curves) for three values of stirring wave vector, $q = 0.25\ q_c$, (a), $q = 0.925\ q_c$(b) and $q = q_c$ (c), for $N = 3$ particles and a barrier strength $\lambda L = 1$. The numerical results are compared with the results of the perturbative approach (thin solid lines). In panel (c) for $q = q_c$ the analytical curves for ideal bosons and the TG gas are identical since $\delta q = 0$ and therefore $\Delta E_q^{(l)}$ and $\left\{u_q^{(l)}, v_q^{(l)}\right\}$ are independent of l.

state which does not couple to the barrier motion. This is again in agreement to what we have found in the calculation of the time-averaged integrated particle current.

In Fig.IV.8 we also show the drag force originating from the stirring of an ideal Bose gas as a function of time. The typical oscillation frequency of the drag force of an ideal Bose gas is fixed by the first energy level splitting $E_{2,q} - E_{1,q}$. Due to the flatter dispersion of the first energy levels as compared to those at the Fermi surface, for the ideal Bose gas the dependence of the drag-force oscillation frequency on the velocity is weaker than the one found for the TG gas. The three panels of Fig.IV.8 correspond to increasing values of the stirring momentum. At small momenta also the ideal Bose gas shows mesoscopic superfluidity. For momenta close to q_c the drag force of the ideal Bose gas is larger in magnitude than the one of the TG gas, illustrating the more important effect of the barrier on the ideal Bose gas. For a stirring momentum equal to q_c the drag force of the TG gas and of the ideal Bose gas are equal in magnitude, as it is the case of the integrated current (see again Fig.IV.3). The vanishing of the drag force for momenta $q < q_c$ is again a mesoscopic effect. Taking the thermodynamic limit of our expression for the drag force we recover a non-zero value at any finite velocity, in agreement with the prediction of nonsuperfluid behavior of a TG gas in an infinitely long wire [31].

The analysis of the drag force complements the study of the superfluid behavior of the mesoscopic 1D Bose gas through the particle current. It confirms the results of the previous sections and in particular the finding of a critical velocity.

IV.5 Conclusions on the superfluid properties of the mesoscopic 1D Bose gas

In order to answer the question about superfluidity in the mesoscopic 1D Bose gas we studied various properties (particle current, particle current fluctuations, drag force) of both the ideal Bose gas and the TG gas. Confining the 1D Bose gas to a ring geometry and subjecting it to a moving repulsive delta barrier potential (drive) our major findings are a superfluid response up to a critical velocity $v_c = \hbar\pi/(mL)$. The same critical velocity is found for the adiabatic and a non-adiabatic external drive and can be identified with Landau's critical velocity marking the point of the lowest energy excitation in the system. Since it scales $v_c \propto 1/L$ it is a truly mesoscopic effect, i.e. in the thermodynamic limit, L tending to infinity keeping N/L constant it vanishes. This is in agreement with previous studies on 1D superfluidity [10, 31]. The qualitative behavior of the 1D Bose gas beyond the critical velocity depends strongly on the external drive. Considering an out-of-equilibrium drive we observe that transfer of angular momentum is only possible at very special velocities of the external drive $v_n = n\hbar\pi/(mL)$, with n being an integer. For all other velocities the system stays in the same branch of angular momentum meanwhile being in a very peculiar excited state. In contrast, for the adiabatic drive, the system always stays in its ground manifold and at $v_n = n\hbar\pi/(mL)$, with n being an odd integer a quanta of angular momentum enters into the system leaving it in a metastable current carrying state. Therefore, the most suitable configuration in order to probe the superfluid behavior of the 1D Bose gas is the adiabatic switching on of the barrier motion.

V Superposition states and entanglement

In this chapter we solely focus on the Tonks-Girardeau limit and the out-of-equilibrium drive. In particular we are going to study the dynamical properties of the TG gas following the sudden switching-on of the barrier motion, instead of taking averages on time as we did in the previous chapter. We focus on the state of the system and analyze its evolution in time. We find that at specific times, the state is a macroscopic superposition of two current states with velocity components 0 and $2v$ for stirring velocities v, multiple of $\pi\hbar/mL$. In terms of occupancies of the mapped Fermi gas, the two components can be identified with two Fermi spheres. Since each Fermi sphere contains many single-particle modes, it is a macroscopic superposition of two multimode states. The chapter is organized as follows. First, we give a brief overview on macroscopic superposition states, emphasizing their importance and prospects for future applications. Second, we analyze the time of formation of this new kind of macroscopic superposition. The exact solution of chapter III allows us to calculate the time-dependent particle current, from which we extract the characteristic time scale. We find that the time evolution for the formation of the superposition state is determined by Rabi oscillations that occur at the avoided level crossings of Fig.III.3 a). Third, in order to study the nature of the superposition state and its degree of entanglement we calculate the one-body density matrix which gives access to the momentum distribution and Wigner quasiprobability distribution function. Comparing the results with the ones obtained for an adiabatic switching-on of the barrier motion we can set constraints on the excitation process, emphasizing the importance of the out-of-equilibrium drive. Since each Fermi sphere has a width in momentum space of the order of the Fermi momentum k_F, we find that an adiabatic drive is unsuitable to resolve the single components of the superposition. The adiabatic drive only couples neighboring states of angular momentum which are spaced by a momentum of $2\pi/L \ll k_F$. Finally, we can simulate

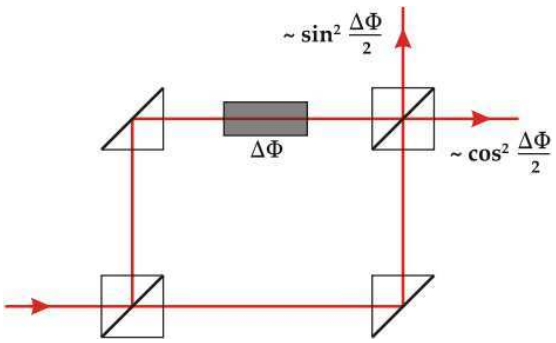

Figure V.1: Schematics of a Mach-Zehnder interferometer. The obstacle in the upper path causes a phase shift in the wave function of the photons with respect to the photons in the lower path which can be read out by the detectors. From [93].

the time-of-flight signal which is the standard probe used in experiments. We find that the TOF images allow to detect this strongly entangled many particle state.

V.1 Overview on macroscopic superposition states

Quantum effects, such as macroscopic quantum superposition states, provide an important playground for the exploration of the transition between quantum mechanics and classical physics. Apart from their scientific relevance quantum superposition states are under investigation due to their promising practical applicability in the fields of high-precision measurements and quantum computation.

V.1.1 High-precision atom interferometry

Ultra high-precision interferometry relies on the measurement of a relative phase (or phase shift) ϕ_{int} between the beams (light or atoms) travelling in the two arms (or paths) of an interferometer. This phase shift is either caused by a change of the pathlength (e.g. due to rotation) in one of the arms of the interferometer or by obstacles (e.g. samples to be measured) in the paths, see Fig.V.1. It has been shown that using entangled states (of light or atoms) as input states in the arms of the interferometer allows for measuring the relative phase with a precision beyond the so-called "shot noise limit" (the precision is limited by the statistics for counting single-particles in the detector) [2, 6]. For the shot noise limit, the uncertainty of the measurement scales $\Delta\phi_{int} \propto 1/\sqrt{N}$, with particle number N [94], and is achieved using a classical input

state in the interferometer. Following a proposal on quantum-enhanced measurements, presenting a variety of possibilities how to surpass the "shot noise limit" and also the "standard quantum limit" (given by the dynamically induced noise in the position measurement of a free mass) [95] two groups, using squeezed states (entangled states), measured relative phases with a precision beyond the shot noise limit [96, 97]. It has been shown that the achieved precision can be further enhanced by using quantum superpositions of macroscopic states instead [34]. Principally, macroscopic quantum superposition states allow for measurements with the ultimate achievable precision, given by the quantum mechanical uncertainty relation (in number phase representation) $\Delta N \Delta\phi_{int} \gtrsim 1$, the so-called "Heisenberg limit". Assuming that $\Delta N \lesssim N$ the limit on phase uncertainty can at best scale $\Delta\phi_{int} \propto 1/N$ [98].

V.1.2 Application to quantum information

Macroscopic quantum superposition states are at the heart of quantum information devices [35] because they realize quantum two-level systems (qubits). Qubits can either be of single-particle nature (single atom, single spin) or realized using collective degrees of freedom whose low-energy spectrum reduces to two discrete states. Experimental realizations of qubits are, e.g. collective internal state transitions for Rydberg atoms [99] and current states in superconducting quantum interference devices (SQUIDs) [100, 101].

V.1.3 Decoherence effects

To date, the realization of quantum superpositions on a macroscopic scale remains challenging for various reasons. They severely suffer from decoherence effects such as coupling to the electromagnetic environment in the case of superconducting circuits (cavity QED) and particle losses or fluctuations in the trapping potential in the case of ultra cold atomic gases. Even worse, for some types of noise, decoherence effects become more efficient upon increasing the number of particles involved in the superposition, an effect known as "superdecoherence". Here, decoherence effects act collectively on excited states and the rate of spontaneous decay scales quadratically with the number of particles [102]. Nevertheless, in recent years experimental progress allowed for the observation of macroscopic superposition states in a variety of systems.

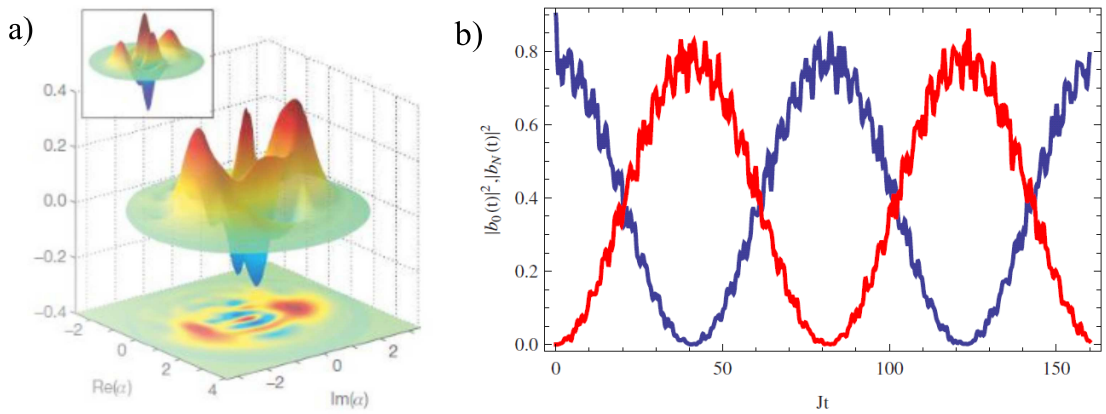

Figure V.2: a) The Wigner quasidistribution function for the superposition of cavity field states. The negative values of the Wigner function indicate the non classical nature of the state. From [36]. b) The population of the two modes of the NOON-state as a function of time. The expected population of unity during the oscillation is not reached due to residual interactions between the particles. This implies that the real state of the system is not the NOON state on which it is projected. From [72]

For example the entanglement of photon states in a cavity [36], manifested in a negative Wigner quasidistribution function, see Fig.V.2 a) or the entanglement of trapped ion states [37, 38]. In the case of entangled ions the superdecoherence was observed upon creating so called Greenberger-Horne-Zeilinger states $|\psi(0)\rangle = 1/\sqrt{2}(|0..0\rangle + |1..1\rangle)$, [103].

Collective-mode superpositions are expected to be better protected against these forms of decoherence, since quantum correlations are spread over several single-particle modes and the loss of one particle does not imply the destruction of the collective mode, hence allowing the superposition to survive. On the other hand, multimode superpositions imply the use of several different single-particle states, and hence typically have a limited degree of entanglement. The mode structure is determined by the interaction strength, i.e. the stronger the interactions are the more modes are populated until in the TG limit every particle is in a different mode. Since the interaction strength also influences the scattering length of the particles it has yet another impact on decoherence processes (particle collisions lead to losses).

V.1.4 Macroscopic superpositions of current states on a ring

Ultracold atomic gases are interesting candidates for the realization of macroscopic superpositions due to their high purity and tunability. Most of the current proposals are based on two-mode Bose-Josephson junctions [104, 105, 106]. Experimental advances in the realization of ring traps [66, 15, 67, 68, 70, 16, 17, 18], as we have seen in Sec.II.3.1, make it realistic to consider the superposition of superflow states carrying different values of angular momentum [107, 108, 109, 23], where the coupling between angular-momentum states is provided by a localized barrier [107, 23] or an optical lattice along the circumference of the ring trap [107, 72]. Both the optical lattice and the barrier break translational invariance and, as it was explained in Sec.II.1, upon setting them into rotation an artificial gauge field is created. Equally weighted superposition states can be realized by tuning the flux Φ near a half-integer value of the Coriolis flux quantum $\Phi_0 = 2\pi\hbar/m$, in correspondence with an avoided level crossing [23, 72]. In the weakly interacting regime they create the maximally entangled NOON-state comprised by a rotating and a non-rotating component as we have seen in Sec.II.4 and can be seen in Fig.V.2 b). The NOON state, being a two-mode superposition of weakly interacting particles, is very sensitive to the particular decoherence processes induced by two- and three-body losses and is also destroyed by the small energy-level splittings. With respect to an ideal Bose gas, weak repulsive interactions induce small energy-level splittings which are harmful to the superpositions. Quite interestingly, in the strongly interacting limit of impenetrable bosons (or the Tonks-Girardeau limit), this drawback is overcome. Due to its fermionized character [13], the Tonks-Girardeau (TG) gas displays the same energy splittings as for noninteracting bosons [23]. Moreover, due to its impenetrability, two- and three-body losses are suppressed in a TG gas [110]. The TG gas is therefore a very promising candidate for the realization of macroscopic superpositions of current states, as can be obtained, for example, by setting into motion the localized barrier potential of the ring. In the TG limit, creation of stationary superposition states with velocity 0 and $2\pi\hbar/mL$, with L being the ring circumference, can be obtained by an adiabatic switching-on of the barrier to a velocity $\pi\hbar/mL$ corresponding to half a Coriolis flux quantum. Such superpositions have been shown to have maximal useful correlations for interferometry [111, 25]. A similar reasoning is expected to hold for the out-of-equilibrium drive which couples the states 0 and $2n\pi\hbar/mL$, for a barrier velocity $n\pi\hbar/mL$. Hence, both set-ups promise to be useful for

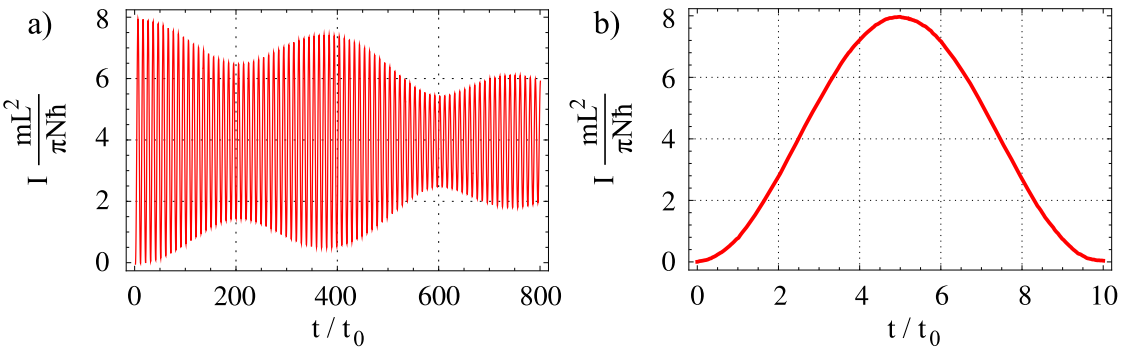

Figure V.3: The time-dependent, integrated particle current in units of $(\pi N\hbar)/(mL^2)$ and for a TG gas subjected to the non-adiabatic stirring described in the text, as a function of the time t in units of $t_0 = mL^2/(\hbar\pi)$, for a barrier strength $\lambda L = 1$, a stirring momentum of $q = 4\pi/L$ and $N = 3$ particles. a) Three frequencies (characteristic frequencies of the concerned avoided level crossings $\Delta E_q^{(2)}$, $\Delta E_q^{(4)}$ and $\Delta E_q^{(6)}$) are involved, indicating the multiple mode nature of the state. b) Zoom on the 1st oscillation, representing an average of the involved frequencies.

applications in ultraprecise atomic gyroscopes, where as we will show the non-adiabatic protocol provides serious advantages over the adiabatic protocol when it comes to the challenge of experimental detection procedures.

V.2 The time-dependence of the system state

So far, we only considered time-averaged quantities in our analysis. However, we have already seen in the previous chapter that all observables calculated for the sudden switching-on of the barrier motion have a time-dependent contribution.

V.2.1 The time-dependent spatially integrated particle current

In this section we investigate the time dependence of the integrated particle current of Eq.(4.2.15). We are particularly interested in the time-dependence at stirring momenta $q = n\pi/L$ with integer n, where a net current is induced into the Bose gas. The out-of-equilibrium drive excites the single-particle states and as can be seen in Fig.III.3 this choice of q corresponds to several avoided level crossings of single-particle states. As a consequence of the sudden quench of the barrier momentum, the single-particle states perform Rabi oscillations at the avoided level crossings with a typical oscillation frequency that is given by their energy splitting, i.e. by $\Delta E_q^{(l)}$.

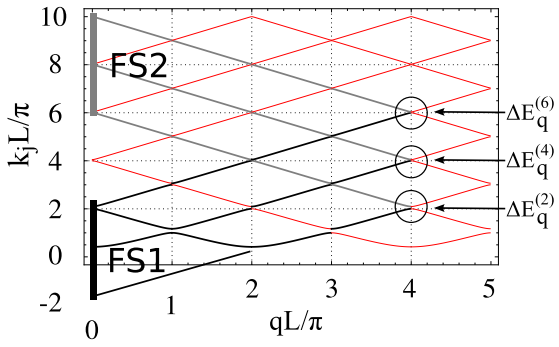

Figure V.4: Schematics of the single-particle excitation spectrum, introduced in Fig.III.2. The figure shows the occupation of $N = 3$ particles, initially occupying the ground state Fermi sphere (FS1), which are excited due to the out-of-equilibrium drive with stirring momentum of $q = 4\pi/L$ (black lines). The concerned avoided level-crossings where the Rabi-oscillations occur are marked by the black circles. At $t = \tau/2$ all particles are in the in the upper state of the concerned avoided level crossing and upon measuring the system state they are projected on the moving Fermi sphere (FS2), indicated by the gray lines. At $t = \tau/4$ the system state is the equal superposition of the two Fermi spheres.

The time-dependent spatially integrated particle current is illustrated in Fig.V.3. In the figure the barrier momentum was set to $q = 4\pi/L$ and an oscillating behavior of the current in time is observed. Panel a) of the figure reveals the contribution of several oscillation frequencies, being an indication for the multi-mode nature of the N-particle state. In panel b) we focus on the short time behavior of the current, thus only looking at the highest involved frequency ω_0, the characteristic frequency for the following studies of the time dependence. It can be identified with the gaps of the involved avoided level-crossings of Fig.III.3, also indicated in Fig.V.4. In fact, for a barrier strength of $\lambda L = 1$ this characteristic frequency is $\omega_0 \backsimeq 0.2\hbar/mL^2$, corresponding to a period of $\tau \backsimeq 10t_0$, and it is an average of the involved characteristic frequencies $\Delta E_q^{(2)}/\hbar$, $\Delta E_q^{(4)}/\hbar$ and $\Delta E_q^{(6)}/\hbar$, as can be seen in the figure. The amplitude of the oscillation reveals a minimal current of value zero, corresponding to zero average particle momentum, and a maximum of $I = 8N\hbar\pi/(mL^2)$, corresponding to an average particle momentum of $k = 8\pi/L \equiv 2q$. The time-averaged integrated particle current is then $I = 4N\hbar\pi/(mL^2)$, corresponding to an average particle momentum of $k = 4\pi/L \equiv q$, in agreement with the results of Fig.IV.3.

V.2.2 The state of the system as superposition of two Fermi spheres

In order to gain insight on the Rabi-like oscillations observed in the current, we proceed by analyzing the occupation numbers of the single-particle states of the mapped Fermi gas as a function of time. We find that the TG gas, which initially occupies the zero-momentum Fermi sphere of the mapped Fermi system, oscillates between two N-particle Fermi spheres, one centered at $k = 0$ and the other at $k = 2q$, realizing at one quarter and three quarters of the oscillation an equally weighted macroscopic superposition of the two Fermi spheres.

The derivation reads as follows. According to the expression for the overlaps c_{jl} in Eqs.(3.5.16) and (3.5.17), the states excited under the effect of the stirring drive are fixed by quasimomentum conservation $k_j = k_l^{(0)} \pm q$ for $q < k_F = N\pi/L$, or $k_j = \pm k_l^{(0)} + q$ for $q > k_F$. In detail, taking for simplicity $q > k_F$ which will turn out to be the most favorable situation, we find that to leading order in λL only four states j are coupled to each single-particle level l of the initial-state Fermi sphere, with coefficients $|c_{jl}| = 1/2$ for $j = n \pm 2\mathrm{Int}[l/2]$ and $j = n + 1 \pm 2\mathrm{Int}[\mathrm{l}/2]$, Int[..] denoting the integer part; with the exception of the lowest state $l = 1$, where $|c_{jl}| = 1/\sqrt{2}$ for $j = n$ and $j = n+1$. For each level k_j we know its momentum (hence angular momentum) components from the analysis of the zero-barrier limit, where a true level crossing occurs of two states of well defined angular momentum. For example, for $v = 4\pi\hbar/mL$ and $N = 3$, the level $l = 1$ is coupled by the stirring barrier to the states with $j = 4$ and 5 which are both an equal-weight superposition of states with momentum $k = 0$ and $k = 8\pi/L$. Similarly, the levels $l = 2$ and 3 yield an equal-weight superposition of states with $k = 2\pi/L$ and $6\pi/L$ for the lowest-energy doublet and of $k = -2\pi/L$ and $10\pi/L$ for the highest-energy doublet. Summing up all the contributions, we find that each momentum state has the same occupation, and the momentum occupation distribution is a superposition of the two Fermi spheres $\{-2\pi/L, 0, 2\pi/L\}$ and $\{6\pi/L, 8\pi/L, 10\pi/L\}$. A similar reasoning holds for arbitrary barrier velocities and particle numbers (chosen odd to ensure proper boundary conditions on the mapped Bose gas), leading to the occupation of two Fermi spheres centered at 0 and $2q$. A schematic drawing, explaining the process is provided in Fig.V.4.

However, it should be noted that the analysis of the particle current cannot prove the existence of a macroscopic superposition and in particular is useless for the detection

of a possible entanglement in the system.

V.3 The one-body density matrix

In order to make statements about the nature of the quantum state and hence about interference effects that lead to entanglement a deeper analysis of the state is needed. The state of the system is represented by its wave function, as we have seen in Sec.III.5.1. Instead of directly using the quantum state of the system for the calculation of observables it is common to use the density matrix, which contains all the information about the state. In general the density matrix is a very complicated object, since its knowledge is directly related to the knowledge of an exact solution for the concerned problem. The knowledge of the many-body wave function allows for the exact calculation of the full density matrix,

$$\rho_B(t) = |\Psi_B(t)\rangle\langle\Psi_B(t)| \ . \tag{5.3.1}$$

In position representation the full density matrix, dependent on all N-particle coordinates $x_1...x_N$, allows for the calculation of the OBDM (see Sec.II.2.2) which is only dependent on one particular particle coordinate x of the many-body wave function $\Psi_{TG}(x, x_2...x_N, t)$. The OBDM is of interest because it enables us to calculate expectation values of single-particle observables. Hence, we obtain the relevant observables for this bosonic problem which is characterized by QODLRO (see Sec.II.2.2) from the analysis of the OBDM. The OBDM is obtained upon integrating the full density matrix over the $N-1$ particle coordinates $x_2...x_N$ of the other particles

$$\rho_B(x, y, t) = N \int dx_2....dx_N \Psi^*_{TG}(x, x_2...x_N, t)\Psi_{TG}(y, x_2...x_N, t) \tag{5.3.2}$$

Following the method of [112] the OBDM can be represented in terms of the single-particle wave functions. This method provides an efficient way for numerical implementation. In essence, using the exact expression (3.4.3) for the many-body wave function, the OBDM can be reduced to the form

$$\rho_B(x, y, t) = \sum_{i,j=1}^{N} \psi^*_i(x, t) A_{ij}(x, y, t) \psi_j(y, t) \ , \tag{5.3.3}$$

where $A_{ij}(x, y, t)$ is a $N \times N$ matrix which is determined by

$$\mathbf{A}(x, y, t) = \Big(\mathbf{P}^{-1}(x, y, t)\Big)^T \det\Big(\mathbf{P}(x, y, t)\Big) \ . \tag{5.3.4}$$

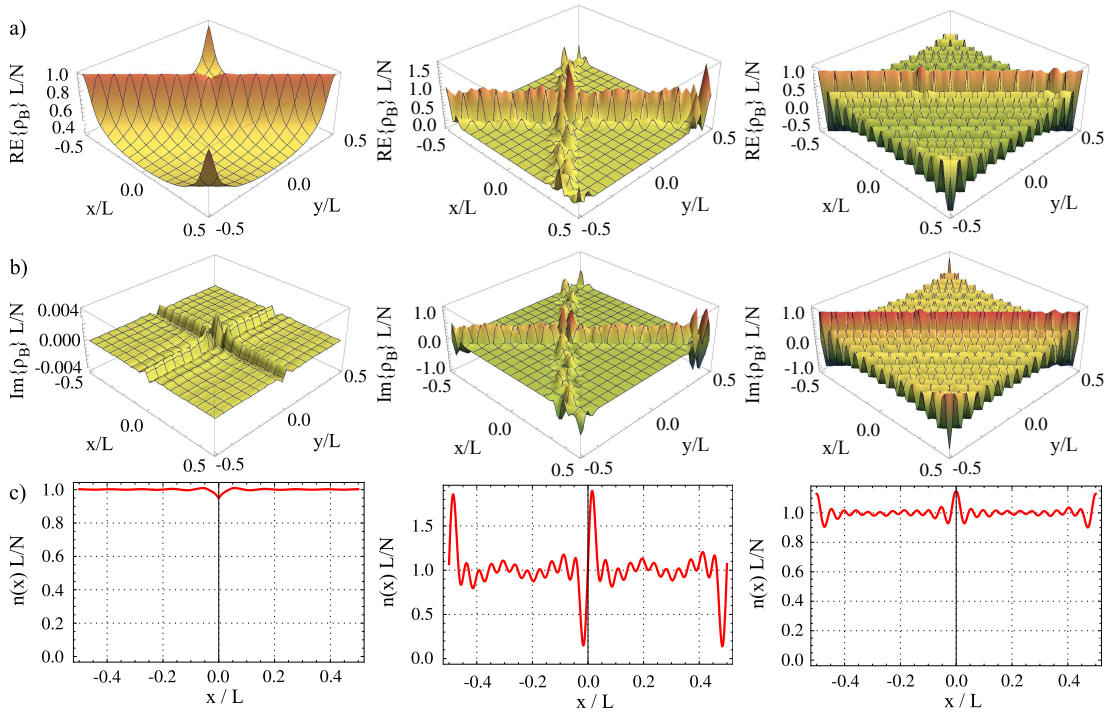

Figure V.5: Real (a) and imaginary (b) part of the OBDM in units N/L at times $t = 0$ (left panel), $t = \tau/4$ (middle panel) and $t = \tau/2$ (right panel) for $N = 9$ bosons stirred by a barrier of strength $\lambda L = 1$ and momentum $q = 14\pi/L$. The corresponding density profiles (c) in the frame co-moving with the barrier. The initial OBDM at $t = 0$ is a real quantity, and the infinitesimal imaginary contribution is due to the limited numerical precision.

The $N \times N$ matrix $P_{ij}(x, y, t)$ only depends on the single-particle wave functions

$$P_{ij}(x, y, t) = \delta_{i,j} - 2 \int_x^y dx' \, \psi_i^*(x', t)\psi_j(x', t) \, , \tag{5.3.5}$$

where we have assumed $x < y$ without loss of generality. It should be noted that the difference between the TG bosons and free fermions is manifested in the matrix $A_{ij}(x, y, t)$, which for free fermions is the unity matrix [113]. A detailed derivation of the above presented method is reviewed in Appendix D.

V.3.1 Numerical calculation of the one-body density matrix

The above presented method allows us to numerically calculate the OBDM. Fig.V.5 displays the result of our calculation for $N = 9$ particles at different times $t = 0$ (the initial state), $t = \tau/4$ (the time of the equally weighted superposition) and $t = \tau/2$ (all particles occupy the shifted Fermi sphere). The diagonal elements of the OBDM

$\rho(x,x,t)$ are purely real and coincide with the density profile of the gas, $n(x,t) = \sum_{l=1}^{N} |\psi_l(x,t)|^2$, also displayed in Fig.V.5. At $t=0$ the density matrix is a real quantity and the infinitesimal imaginary contribution is due to limited numerical precision. At the time of the superposition (middle panel) we can see a shock-wave behavior in the density profile indicating transfer of angular momentum into the TG gas. In contrast, the density profile displays less spatial fluctuations both at $t=0$, when all particles are at rest, and at $t=\tau/2$, when all particles move. The discontinuity at $x=0$ is due to the density suppression caused by the barrier and is best seen in the density profile for $t=0$. Its mathematical origin is the cusp condition of Eq.(3.5.10).

V.3.2 Analytical calculation of the one-body density matrix

In order to gain a better physical understanding of the behavior of the TG-gas, and in particular the observables that are calculated from the OBDM we also found an analytical expression for the OBDM upon making various approximations. It should be noted that the following analysis is more simplified than the perturbative approach presented in Sec.III.5.2, but as we shall see is capable of providing a good understanding of the numerical results. The fundamental assumptions that we have to make in order to perform the analytical calculation of the OBDM are the following. We choose the resonance value, i.e. $q = n\pi/L$, with integer n for the barrier momentum. Moreover,

- we choose $N=3$ bosons.
- the spectrum $k_l(q)$ is linear and therefore for stirring momenta $q = n\pi/L$, with integer n, the single-particle momenta become $k_l = l\pi/L$, with integer l, see Fig.V.4. This assumption is justified for weak barriers $\lambda L \leq 1$ and amounts to neglect the gaps, opened by the barrier in the momentum dispersion.
- in order to account for the Rabi-oscillations at the avoided level crossings, fundamental for the creation of the superposition, we assume the same characteristic level splitting for all avoided level crossings, i.e. $\Delta E_q^{(l)} = \hbar\omega_0$ in Fig.V.4. Here $\Delta E_q^{(l)} = E_{l+1,q} - E_{l,q}$ and $E_{l,q}$ is given by the perturbative expression in Eq.(3.5.25).
- due to the observation that for a barrier strength $\lambda L = 1$ the period is approximately $10t_0$ we further make the assumption that $\tau = 10t_0$ which allows us to drop the time-dependent phases in the single-particle wave functions.

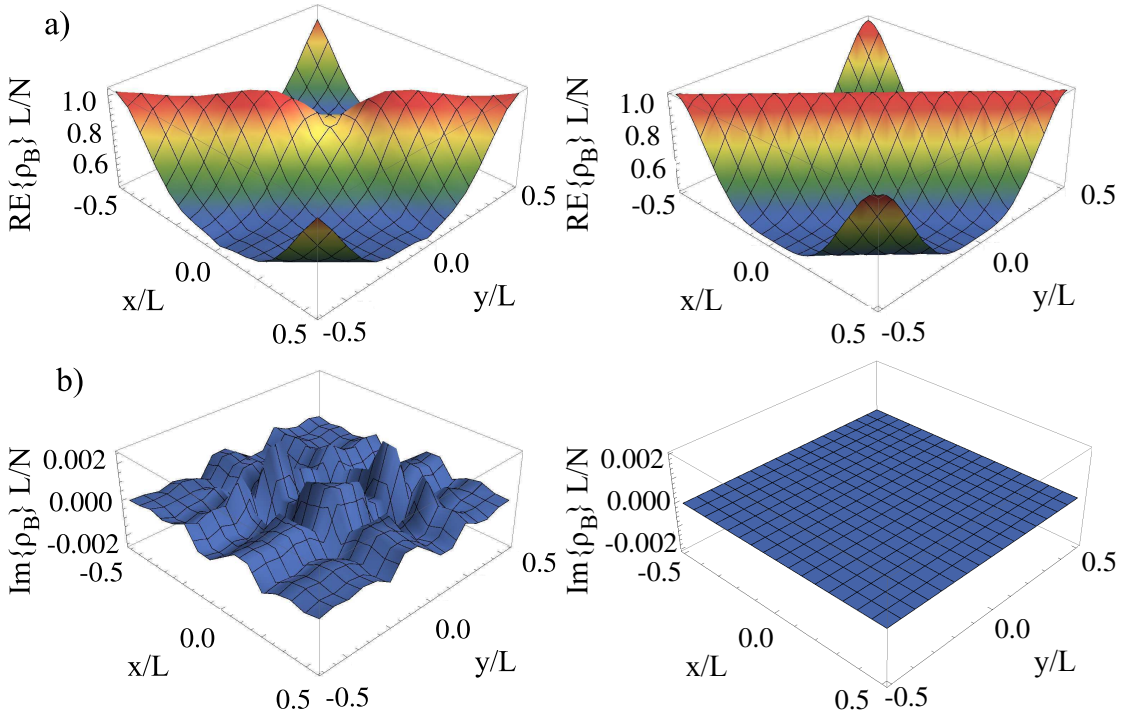

Figure V.6: The density matrix in units of N/L for $t = 0$ and $q = 4\pi/L$ for $N = 3$ bosons. a) Real part of the OBDM derived form an exact numerical computation for $\lambda L = 1$ (left panel) and the analytical approximation as explained in the text (right panel). b) Imaginary part of the same OBDM. The dip (local suppression of the density) in the numerical density profile is due to the presence of the barrier which is absent in the analytical model.

Given these assumptions we calculate the OBDM for $N = 3$ bosons stirred by a weak barrier with $\lambda L = 1$ moving at a velocity $v = 4\hbar\pi/(mL)$. As a basis we use the initial (at $t = 0$) single-particle orbitals, derived in Eq.(3.5.14) and (3.5.15). Given the fact that the single-particle momenta are integer multiples of π/L these orbitals reduce to

$$\phi^{(0)}_{2l+1}(x) = (-)^l \sqrt{\frac{2}{L}} \cos\left[\frac{2l\pi}{L}x\right] \tag{5.3.6}$$

$$\phi^{(0)}_{2l}(x) = i(-)^l \sqrt{\frac{2}{L}} \sin\left[\frac{2l\pi}{L}x\right] , \tag{5.3.7}$$

with $l = 1, 2, 3....$ The lowest-lying orbital reads $\phi^{(0)}_1(x) = 1/\sqrt{L}$ and in particular is independent of the position. Obviously at $t = 0$ the particles occupy the Fermi-sphere FS1 in Fig.V.4, built of the three lowest lying orbitals $\phi^{(0)}_1(x)$, $\phi^{(0)}_2(x)$ and $\phi^{(0)}_3(x)$. At $t = 0^+$ the external drive suddenly excites the particles in higher levels following Eq.(3.5.5). For $q = 4\pi/L$ the barrier drives the single-particle states into the avoided level crossings, indicated by the circles in Fig.V.4, where they perform the already

mentioned Rabi-oscillations. At $t = \tau/4$ the equally weighted superposition of the two Fermi-spheres (FS1) and (FS2) is obtained and the single-particle wave functions read

$$\psi_{1,\frac{4\pi}{L}}(x,\frac{\tau}{4}) = \frac{1}{2}\left[(1+i)\phi^{(+)}_{9/8}(x) - (1-i)\phi^{(0)}_{1}(x)\right] \tag{5.3.8}$$

$$\psi_{2,\frac{4\pi}{L}}(x,\frac{\tau}{4}) = -\frac{1}{\sqrt{2}}\left[\frac{1-i}{2}\sqrt{2}\phi^{(0)}_{2}(x) - \frac{1+i}{2}\phi^{(+)}_{7/6}(x) + \frac{1+i}{2}\phi^{(+)}_{11/10}(x)\right] \tag{5.3.9}$$

$$\psi_{3,\frac{4\pi}{L}}(x,\frac{\tau}{4}) = -\frac{1}{\sqrt{2}}\left[\frac{1-i}{2}\sqrt{2}\phi^{(0)}_{3}(x) - \frac{1+i}{2}\phi^{(+)}_{7/6}(x) - \frac{1+i}{2}\phi^{(+)}_{11/10}(x)\right] , \tag{5.3.10}$$

where $\phi^{(+)}_{i/j}(x) = (\phi^{(0)}_{i}(x)+\phi^{(0)}_{j}(x))/\sqrt{2}$. At $t = \tau/2$ all the particles occupy the Fermi-sphere (FS2), centered around $k = 8\pi/L$, built on the single-particle wave functions

$$\psi_{1,\frac{4\pi}{L}}(x,\frac{\tau}{2}) = -\phi^{(+)}_{9/8}(x) \tag{5.3.11}$$

$$\psi_{2,\frac{4\pi}{L}}(x,\frac{\tau}{2}) = \frac{1}{\sqrt{2}}\left[-\phi^{(+)}_{7/6}(x) + \phi^{(+)}_{11/10}(x)\right] \tag{5.3.12}$$

$$\psi_{3,\frac{4\pi}{L}}(x,\frac{\tau}{2}) = -\frac{1}{\sqrt{2}}\left[\phi^{(+)}_{7/6}(x) + \phi^{(+)}_{11/10}(x)\right] . \tag{5.3.13}$$

These single-particle wave functions can be substituted into Eq.(5.3.3) and (5.3.4) and an entirely analytical expression is found for the OBDM. A very good agreement is obtained upon comparison with the numerically computed (exact) OBDM, as can be seen in Fig.V.6. The numerical OBDM displays the characteristic dip on its diagonal (in the density profile) due to a density suppression caused by the barrier already mentioned in the previous section. The absence of the dip in the density profile of the analytical density matrix is readily explained upon noticing that the linearized spectrum, used for the calculation of the orbitals equals the spectrum for $\lambda L = 0$. This means that the effect of a density suppression, due to the finite barrier, cannot be seen in the analytical OBDM.

V.4 The momentum distribution

The OBDM in the previous section only serves the purpose to calculate physical quantities which in turn allow us to make predictions about the behavior of the system itself.

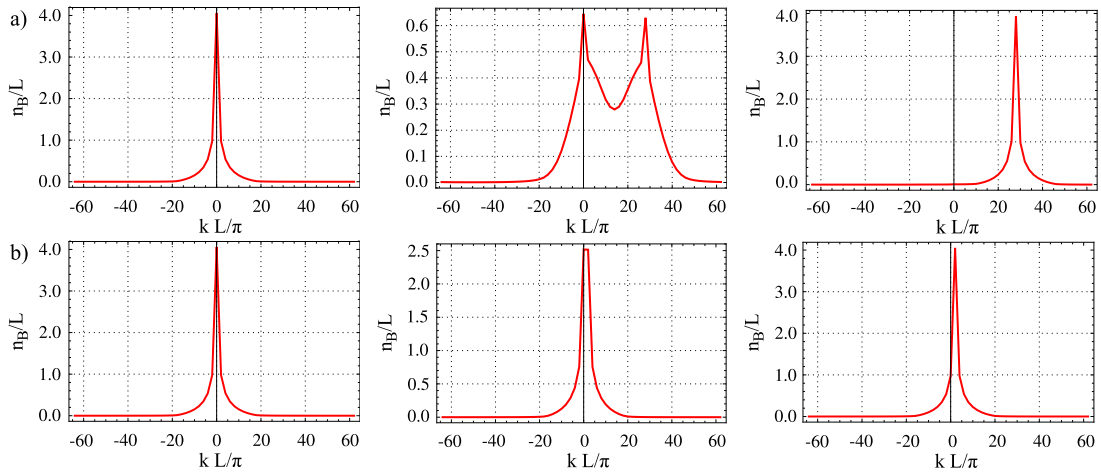

Figure V.7: The momentum distribution function $n_B(k,t)$ in units of L as a function of the particle momentum k in units of π/L at time $t=0$ (left panel), $t=\tau/4$ (middle panel) and $t=\tau/2$ (right panel). a) The momentum distribution obtained from the OBDM of Fig.V.5 for $N=9$ particles ($k_F=8.029\pi/L$), barrier strength $\lambda L=1$ and a barrier momentum $q=14\pi/L$. b) The momentum distribution obtained upon an adiabatic stirring to $q=\pi/L$. The adiabatic mechanism is unsuitable for the detection of the superposition since it cannot resolve the double-peak structure as it is explained in the text.

One of these quantities is the momentum distribution, extracted in experiments on cold atomic gases from the major probing technique, the time-of-flight (TOF) images. The momentum distribution $n_B(k,t)$ is a probability distribution that quantifies the number of particles in phase-space with a given momentum and allows for a "tomographic" information on the distribution of the velocities of the atoms contributing to the total current $I(t)$ presented in Fig.V.3, where

$$I(t)=\int k\; n_B(k,t)\;. \tag{5.4.1}$$

In our case the 1D momentum distribution serves as a measure of the distribution of angular momentum in the system. It provides additional information that cannot be extracted from the induced particle current, presented in the previous chapter. Therefore the 1D momentum distribution allows for a closer inspection of the system state itself. It is defined as the Fourier transform of the OBDM with respect to the particle coordinates,

$$n_B(k,t)=\int_{-L/2}^{L/2}\int_{-L/2}^{L/2} dxdy\; e^{ik(x-y)}\rho_B(x,y,t)\;. \tag{5.4.2}$$

Fig.V.7 a) displays the time evolution of the momentum distribution, induced by a barrier of strength $\lambda L=1$ and momentum close to an integer multiple of π/L. It

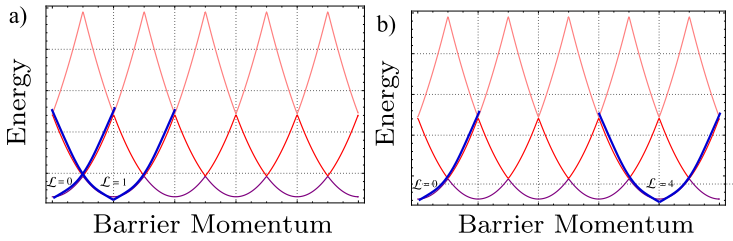

Figure V.8: Schematics for the coupling of different states of angular momentum. The left panel shows a coupling of neighboring states as it would be obtained by an adiabatic stirring mechanism. The right panel represents the coupling of states that lie very far in momentum space and can only be coupled by the out-of-equilibrium drive described in the text.

evolves from a single peak at $k = 0$ to a single peak at $k = 2q$. At intermediate times, a double peak structure is found, reflecting the superposition of the two Fermi spheres of the mapped Fermi gas. The peaks in the momentum distribution, associated with the bosonic nature of the gas, allow to well identify the two components. However, since the width of the TG momentum distribution is the same as the fermionic one, in order to better resolve the superposition one needs stirring momenta larger than the Fermi momentum k_F, i.e. a velocity larger than the sound velocity of the TG gas. Generally, large stirring momenta allow to couple states that are very far in momentum space, as is sketched in Fig.V.8b. It should be noted that an adiabatic stirring mechanism can only couple neighboring states in angular momentum, i.e. that are separated by $k = 2\pi/L$ in momentum space, see Fig.V.8a. Therefore an adiabatic stirring mechanism is not suited for the detection of a macroscopic superposition of the two Fermi-spheres. This is illustrated in Fig.V.7b).

A closer look at the momentum distribution of the superposition, i.e. at $t = \tau/4$, reveals some structure in the region between the two peaks. Apparently, the width of the peaks is enhanced with respect to width of the single peaks at $t = 0$ and at $t = \tau/2$. This structure can be seen as a smoking gun for quantum interference effects between the two components of the superposition. However, this observation is neither sufficient to make precise predictions concerning a possible entanglement of the state nor is it suitable for the observation of correlations between the different modes of the superposition in experiments. Nevertheless, this structure provides a strong motivation to further investigate its origin. Moreover, a kink is observed at the inner side of each peak which is a numerical artefact and due to the reduced number of numerical data points as we will see in the following section. The resolution for the numerical analysis scales with the particle number, i.e. it is restricted. In the case of $N = 9$ particles this

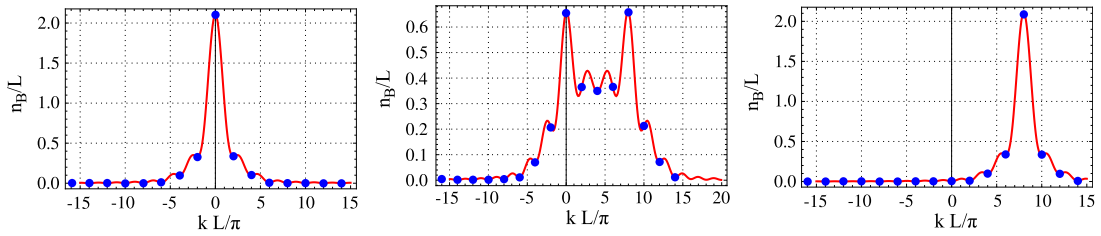

Figure V.9: The analytically calculated momentum distribution function $n_B(k,t)$ (red solid line) in units of L as a function of the particle momentum k in units of π/L for $N = 3$ particles and at times $t = 0$ (left panel), $t = \tau/4$ (middle panel) and $t = \tau/2$ (right panel). The barrier strength is $\lambda L = 1$, its momentum was set to $q = 4\pi/L$ and $k_F \backsimeq 2\pi/L$. For a comparison the numerically computed momentum distribution is displayed (blue dotted line) with the exact Fermi momentum $k_F \backsimeq 2.096\pi/L$.

is displayed in Fig.V.7.

The analytical solution for the OBDM of Sec.V.3.2 allows us to calculate the momentum distribution for $N = 3$ particles by analytical means. Apart from the possibility to compare the analytically calculated results to the ones obtained from the numerical computation it provides the possibility to further investigate the two open questions of the previous section since it is a continuous function of momentum.

The analytical momentum distribution is displayed in Fig.V.9. We observe smooth, overall contineous behavior, including the peaks, and small oscillations, not seen in the numerical analysis. The corresponding numerical momentum distribution is also displayed for comparison (blue dots). We find that the kinks in Fig.V.7 are indeed numerical artefacts and even more pronounced in the $N = 3$ particle case. Additionally we gain further insight in the findings regarding the general structure of the momentum distribution at the time of the superposition $t = \tau/4$. We can indeed relate the broad distribution of particle momentum to possible interference effects upon comparing it with the momentum distribution that is obtained for a statistical mixture of two Fermi spheres centered around $k = 0$ and $k = 2q$, see Fig.V.10. The momentum distribution of the statistical mixture displays enhanced peaks whereas it reveals almost depletion for $0 < k < 2q$, thus suggesting the absence of correlations between particles at rest and particles rotating at $k = 2q$. However, the broad structure seen in the momentum distribution of the assumed macroscopic superposition can at best be an indication for interference effects, and is not a rigorous proof as there might be other classical states which yield the same effect. An exact analysis, allowing us to make precise statements about the state and its nature will be presented in the following section where we

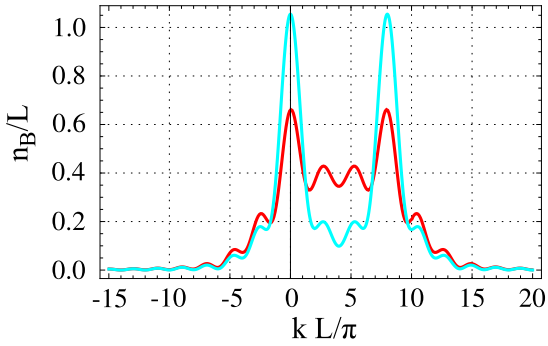

Figure V.10: Analytically calculated momentum distribution function $n_B(k,t)$ for the macroscopic superposition of two Fermi spheres centered at $k = 0$ and $k = 2q$ in units of L as a function of the particle momentum k in units of π/L for $N = 3$ particles and $q = 4\pi/L$ at $t = \tau/4$ (red solid line), and momentum distribution for a statistical mixture of the same Fermi spheres (cyan solid line). The statistical mixture shows very little structure in the region between the two peaks since there are no quantum interference effects. In contrast, the macroscopic superposition shows a very broad distribution of particle momentum which is an indication for interference effects between the two Fermi spheres.

calculate the Wigner distribution function.

Before we turn to the interference effects we want to answer another important question, which can be analyzed from the momentum distribution. It concerns the robustness of the superposition with respect to fluctuations in the external parameters. In view of a possible experimental realization of our system in the near future we consider the effect of noise in the barrier parameters on the superposition state. In particular, a high accuracy in the tuning of the barrier velocity will be decisive for the creation of superposition states. This follows from the time-averaged integrated particle current in Fig.IV.3. For weak barriers $\lambda L < 1$ the time-averaged particle current reveals a very peaked behavior at stirring momenta $q = n\pi/L$, with integer n. Being slightly off-resonant, i.e. $(n-1)\pi/L < q < n\pi/L$ the weak barrier does not transfer angular momentum to the gas and the momentum occupation distribution is a single Fermi sphere centered at $k = 0$. Consequently, no superposition is created. This problem can however be overcome by increasing the barrier strength which broadens the current peaks around $n\pi/L$. This is because a stronger barrier further opens the gaps at the avoided level crossings (smoothening them) and hence allows for transitions that are off-resonant. It should be noted that by setting the barrier momentum slightly off resonance, the oscillation frequency changes. The robustness of the superposition can be seen in Fig.V.11. In the figure we compare the numerically calculated momentum distribution for two different barrier strengths $\lambda L = 1$ and $\lambda L = 10$ in the case of

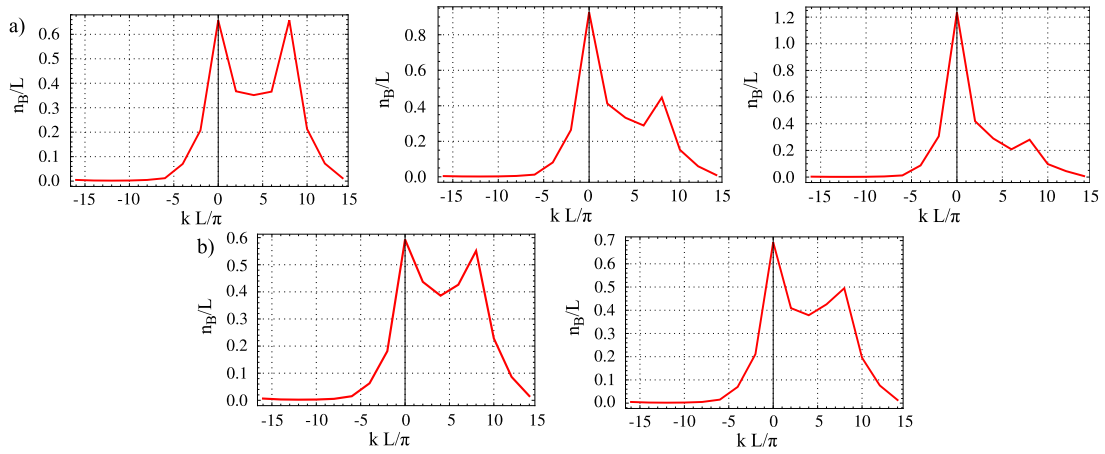

Figure V.11: The robustness of the superposition upon detuning the barrier momentum from $n\pi/L$, with integer n. a) The momentum distribution function $n_B(k,t)$ in units of L as a function of the particle momentum k in units of π/L at time $t = \tau/4$ for a weak barrier $\lambda L = 1$, $N = 3$ particles and barrier momentum $q = 4\pi/L$, $q = 3.99\pi/L$ and $q = 3.98\pi/L$. The superposition already suffers from a detuning of the barrier momentum by 1% and is quasi destroyed by an uncertainty of 2%. b) The momentum distribution at time $t = \tau/4$ for a strong barrier $\lambda L = 10$ and barrier momenta $q = 4\pi/L$ and $q = 3.89\pi/L$. The superposition is robust upon detuning the barrier momentum by 10%.

$N = 3$ particles. For a the weak barrier the superposition already suffers from a detuning of the barrier momentum by 1% off resonance and is quasi destroyed by an uncertainty of 2%. In contrast, increasing the barrier strength by an order of magnitude the superposition becomes relatively robust upon detuning the barrier momentum 10% off resonance. However, as already mentioned, fluctuations in both q and λ cause an uncertainty in τ which renders a possible readout process difficult.

V.5 The Wigner quasiprobability distribution function

The dynamics of the momentum distribution, which were extensively discussed in the previous section, give some hint for the existence of quantum correlations between the two Fermi spheres (FS1) and (FS2) in Fig.V.4. Except for times equal to an integer multiple of $\tau/2$, i.e. when all particles are at rest of moving at twice the barrier speed, we expect an entangled state which has a maximal entanglement at times $t = (2n+1)\tau/4$, with integer n. In particular the comparison between the momentum distribution of the statistical mixture and the momentum distribution of

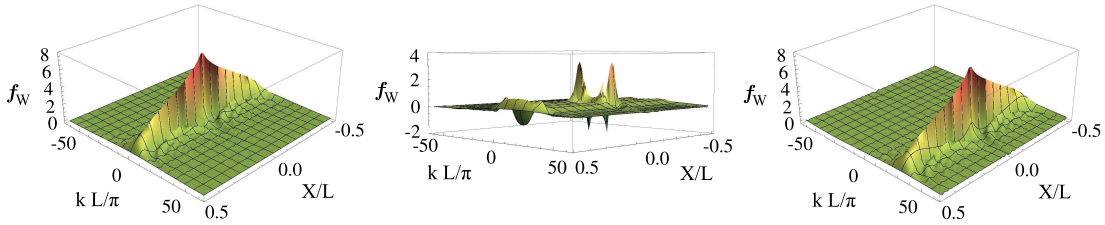

Figure V.12: The Wigner distribution function $f_W(X,k)$ in arbitrary units as a function of the particle momentum k in units of π/L and the center of mass coordinate X in units of L for $N=9$ particles and $q=14\pi/L$ at times $t=0$ (left panel), $t=\tau/4$ (middle panel) and $t=\tau/2$ (right panel). The negative value of the Wigner function at the time of the superposition state prooves the non-classical character of the superposition due to quantum interference effects.

the macroscopic superposition strongly suggests that there are interferences. To show that the state of the system is nonclassical, we calculate the Wigner quasiprobability distribution function [114, 115] of the state at the time of the superposition. For a classical state the Wigner function is a true probability distribution function and hence strictly positive. This however, is not true once the quantum nature of a state becomes visible. Due to the uncertainty principle, position and momentum cannot be resolved on an area in phase space $\Delta x \Delta k < 1$ and the nonclassical nature of a quantum state, e.g. a macroscopic quantum superposition, will be manifested by negative values in the Wigner function on such small areas. Moreover, the Wigner function of a macroscopic quantum superposition will display at least two well separated peaks in between which oscillations, i.e. interference fringes in phase space, are observed. The Wigner quasiprobability distribution function is defined as the Weyl-Wigner transform of the density matrix, i.e. in our case the Fourier transform of the OBDM with respect to the relative particle coordinate $r = x - y$,

$$f_W(X,k,t) = \int dr e^{ikr} \rho_B(X + r/2, X - r/2, t) \ , \tag{5.5.1}$$

where $X = (x+y)/2$ is the center of mass coordinate. As a main result we find that the time of the equal-weight superposition, the Wigner distribution function displays the predicted negative regions with small oscillations inbetween, which can be seen in Fig.V.12. At $t=0$ and at $t=\tau/2$ the Wigner function is positive representing a classical state of the system. This confirms our prediction of quantum correlations between the two Fermi spheres at times $t \neq n\tau/2$, with integer n. However, the Wigner function does not give a possibility to quantify these correlations but just provides a

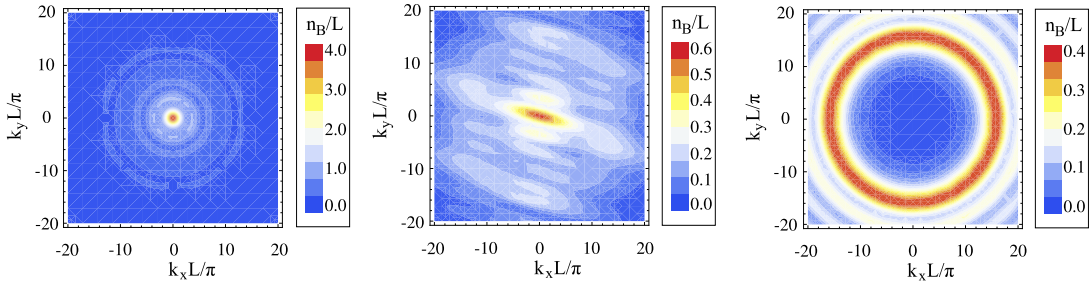

Figure V.13: The TOF images for $N = 9$ particles, a barrier strength $\lambda L = 1$ and barrier momentum $q = 14\pi/L$ at times $t = 0$ (left panel), $t = \tau/4$ (middle panel) and $t = \tau/2$ (right panel). Due to the entanglement of the two Fermi spheres, the time evolution of the TOF images is very complex and at the time of the macroscopic superposition the TOF image is not just the combination of the other two images, displayed in Fig.V.14, but rather a complicated object.

basis for their quantification, which could be done, e.g. following [116] by taking into account both the effective size of the superposition and its degree of coherence. The degree of entanglement of the superposition state could equally be quantified by calculating the quantum Fisher-Information as it was done in [25].

V.6 The time-of-flight images

Current experimental detection techniques are based on time-of-flight (TOF) images, obtained by releasing the confining potential as it was explained in Sec.II.3. The sudden density drop during the expansion enables to describe the spatial distribution of the atomic cloud after expansion as the momentum distribution of the initial state. In the case of the ring we have

$$n_{TOF}(\mathbf{k}) = \int d^3x \int d^3x' e^{i\mathbf{k}\cdot(\mathbf{x}-\mathbf{x}')} \rho_B^{ring}(\mathbf{x}, \mathbf{x}', t) \tag{5.6.1}$$

where the expression in cylindrical coordinates of the 3D one-body density matrix on a tight ring trap of radius R is

$$\rho_B^{ring}(r, \theta, z; r', \theta', z'; t) = \delta(r - R)\delta(r' - R)\delta(z)\delta(z')\rho_B(R\theta, R\theta', t) \ . \tag{5.6.2}$$

Figure V.13 shows the TOF images corresponding to stirring times $t = 0$, $t = \tau/4$ and $t = \tau/2$, illustrating the transition between a zero-current state at initial time to a state of angular momentum $\mathcal{L}/N = 2mvR$. The initial peak at $k = 0$ deforms spirally and

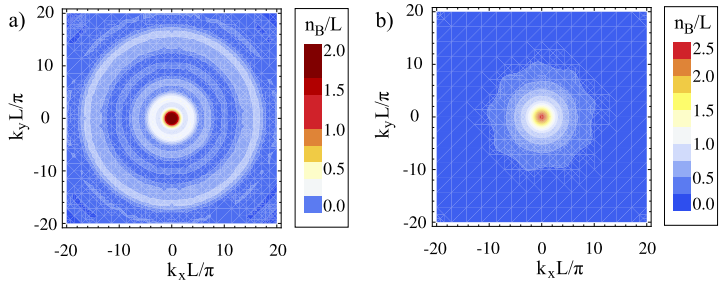

Figure V.14: a) The TOF image of a statistical mixture between the zero-current state and the state at moving at momentum $2q$. The image shows qualitative differences with respect to the TOF image of the macroscopic superposition, displayed in the middle panel of Fig.V.13. The TOF imaging technique thus provides a reliable prediction whether the current states are just superimposed or really strongly correlated. b) The TOF image of a macroscopic superposition created by an adiabatic stirring mechanism is qualitatively indistinguishable form the one of the initial state.

finally tends to a ring, the latter in agreement with the predictions of [108] for a state with well-defined current. Note that the TOF image of the equal-weight macroscopic superposition, represented in the second panel in Fig.V.13, is not simply obtained as a combination of the TOF images of well-defined current states as would be the case for a statistical mixture between the zero-current state and the state at $2q$, displayed in Fig.V.14b. Due to interference between the between the two Fermi spheres the entire time evolution of the state is complicated and the TOF images can be used for the detection of correlations. The time evolution from the zero current state to the state moving at $2q$ is also shown in the sequence of Fig.V.15 for $N = 3$ particles.
Before concluding we would like to compare our results to those obtained from an adiabatic stirring mechanism. The latter leads to the superposition of two neighboring states of angular momentum which are unresolvable in the TOF images as can be seen in Fig.V.14. We already encountered this problem upon analyzing the momentum distribution in the case of the adiabatic switching on of the barrier motion in Sec.V.4. It is due to the fact that the momentum difference of the two components is much smaller than the Fermi momentum.

V.7 Conclusions on macroscopic superposition states

In this chapter we studied the dynamical properties of the strongly interacting (Tonks-Girardeau limit) quasi-one dimensional Bose gas on a tight ring trap subjected to a

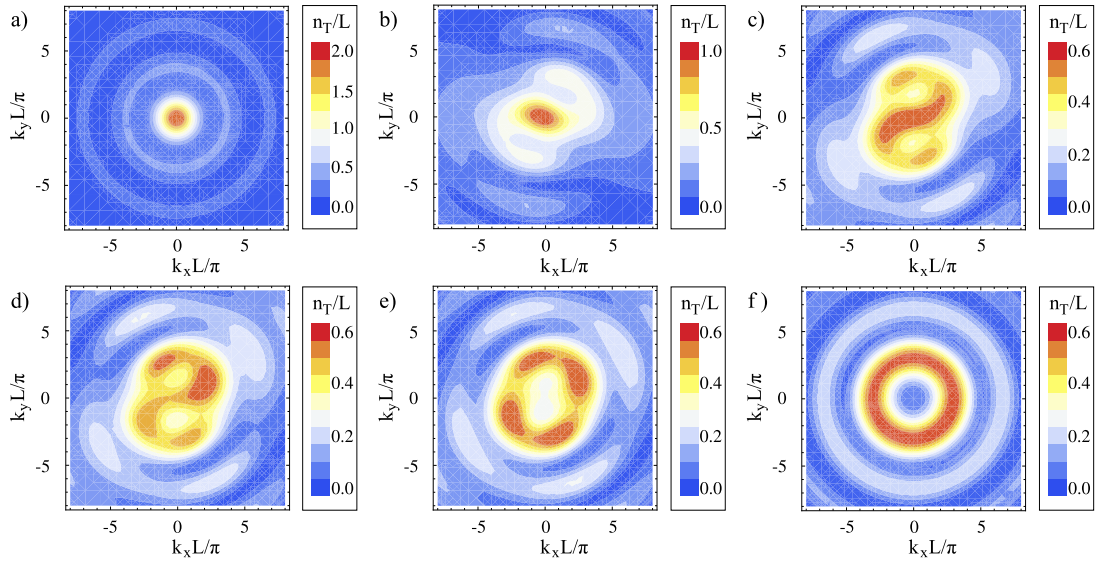

Figure V.15: The TOF images for $N = 3$ particles, barrier strength $\lambda L = 1$ and barrier momentum $q = 4\pi/L$ at times (a) $t = 0$, (b) $t = \tau/4$, (c) $t = 0.3\tau$, (d) $t = \tau/3$, (e) $t = 0.38\tau$ and (f) $t = \tau/2$.

moving δ-barrier potential which is suddenly set into motion. Using the exact solution for the dynamical evolution of the many-body wave function, derived in Chapter III, allowed us to calculate the momentum-distribution, the Wigner quasi-distribution function and the time-of-flight images. We predict the formation of a macroscopic superposition of a rotating and a nonrotating Fermi sphere of the mapped Fermi gas upon evolving in time. We find that the barrier velocity should be tuned close to multiples of integer or half-integer number of Coriolis flux quanta, i.e. to stirring momenta $q = n\pi/L$, with interger n, to maximize the nonadiabatic excitation. This choice of the stirring momentum also fixes the characteristic time scale of the Rabi-like oscillation that is observed in the state, and can be identified with the characteristic frequencies of the concerned avoided level-crossings. We find that the stirring momentum should be larger than the the Fermi momentum $k_F = N\pi/L$ in order to better discriminate the two components of the superposition, in the momentum distribution. The Wigner function of the Bose gas allowed us to identify quantum interferences in the superposition, manifesting the non-classical nature of the system state at the time of the superposition. Finally, the analysis of the time-of-flight images allows us to make precise predictions for the detectability of the macroscopic superposition in future experiments.

VI Conclusion and Outlook

In the context of this thesis we have studied the 1D Bose gas confined to a toroidal geometry and under the influence of a rotating delta barrier potential. Our theoretical model is valid for arbitrary barrier strength and we have focussed on the strongly interacting regime in the impenetrable boson limit. The barrier potential is either set into motion adiabatically, leaving the system in its ground manifold or it is suddenly set into motion (out-of equilibrium drive), hence creating high excitations. In order to obtain an exact solution for the many-body wavefunction and its evolution we use, as theoretical method, the time-dependent Bose-Fermi mapping of M. D. Girardeau and E. M. Wright [14]. The exact solution allows us to answer questions concerning mesoscopic superfluidity as well as the existence and formation of entangled states.
Our main findings are the following:

a. **Superfluid properties**

- We have calculated the single particle spectrum which is periodic behavior in the barrier velocity v, with periodicity $2\hbar\pi/(mL)$. At integer multiples of $\hbar\pi/(mL)$ avoided level crossings are observed in the single particle spectrum
- Both for the ideal Bose gas and the TG gas, analyzing the time averaged spatially integrated particle current, we have found a critical value for the barrier velocity $v_c = \hbar\pi/(mL)$ below which the system displays a superfluid response. This critical value is similar to the one found for weak interactions between the particles [10, 30].
- The behavior of the time averaged spatially integrated particle current for barrier velocities $v > v_c$ depends very much on the type of stirring mechanism that is applied.
  - An adiabatic drive causes a staircase behavior of the current as a function of the stirring velocity, at each step a quantum of angular momentum enters into the system. Due to the adiabaticity of the drive the

system is left in its energy ground state.

  - An out-of equilibrium drive highly excites the system and leaves it in its initial state of angular momentum. Only at special values of the barrier velocity, being integer multiples of the critical velocity, angular momentum can be transferred to the system. Hence the current displays a peaked structure similar to the comb function with the height of the peaks being propotional to the barrier velocity.

- The width of the steps/peaks is broader for the ideal Bose gas than for the TG gas since all particles occupy the lowest-lying state. The lowest-lying states are more effected by the barrier, thus causing a bigger width of the steps/peaks.
- Analyzing the drag force for the out-of equilibrium drive we have found a vanishingly small drag force for $v \neq nv_c$, with integer n, confirming the results found in the analysis of the time averaged spatially integrated particle current that no current is induced for these values of the barrier velocity.
- The critical velcity v_c found in the analysis of the drag force coincides with the one found in the analysis of the time averaged spatially integrated particle current.
- At barrier velocities close to integer multiples of the critical velocity the drag force displays an oscillating behavior in time. The characteristic time-scale is given by the inverse of the Rabi-frequencies of the avoided level crossings in the spectrum

b. **Macroscopic superposition**

- Focussing on the out-of-equilibrium drive and the TG gas, we have computed the one-body density matrix in order to access the momentum distribution, the Wigner quasiprobability distribution function and the time-of-flight signal.
- We have analyzed the particle momentum distribution which for barrier velocities $v = nv_c$, with integer n, displayes the same oscillating behavior in time as the drag force. At intermediate times we could distinguish two seperate peaks belonging to particles at rest (not moving) and particles moving at twice the barrier velocity. Between the peaks, some structure was seen, indicating interferences.

- In order to resolve the two peaks the barrier velocity needs to be larger than the Fermi velocity of the mapped Fermi gas.
- Comparing the momentum distribution of the created state with the momentum distribution obtained for a statistical mixture of non-rotating particles and particles rotating at twice the barrier velocity reveales qualitative differences, again a signature for interferences.
- We have calculated the Wigner quasiprobability distribution function for barrier velocities $v = nv_c$, with integer n. It displays negative regions and small oscillations between its two main peaks. The state of the system is hence non-classical and the existence of an entangled macroscopic superposition could be confirmed.
- We have simulated the time-of-flight images. A sequence of the TOF signal exactly shows how angular momentum gets transferred which have been found to be appropriate to detect the macroscopic superposition.

In conclusion, we have provided an analysis of the driven 1D Bose gas confined to a toroidal geometry. With the presented model we studied two very important limits concerning the inter-particle interaction, i.e. the ideal Bose gas and the TG gas and two types of stirring mechanisms, i.e. adiabatic and out-of-equilibrium. Both the analyzed interaction strengths and the driving mechanisms represent very important limits and can be used as references for further studies. Nevertheless, there are still many open questions

- In experiments the interaction between the particles will always be finite. This regime cannot be treated with the theoretical tools used in the context of this thesis. Future investigations in the framework of Gross-Pitaevskii theory, Bogoliubov's theory and Luttinger-Liquid theory will allow to access the behavior of the 1D Bose gas for weak/intermediate interaction strength.
- The out-of-equilibrium drive assumed a Landau-Zener tunneling probability $P_{LZ} = 1$ whereas the adiabatic drive assumes $P_{LZ} = 0$. Assuming a tunneling probability different form $P_{LZ} = 0$ and $P_{LZ} = 1$ could be treatable for small particle numbers.
- We have shown that the real structure of the barrier for a square barrier of length ℓ and height $1/\ell$ can well be approximated by a delta barrier. More realistic for an

experiment would be a barrier of gaussian or lotentzian shape. The WKB method could provide a mean to be treating the tunneling through such a barrier.

- An interesting question, yet to be answered, concerns the quantification of the amount of entanglement of the superposition. An evaluation of the quantum Fisher-Informantion as described in, e.g. [76], would provide one possibility. Using the Wigner representation a quantification of the degree of entanglement could be achieved following the proposal of [116]

VII Acknowledgements

Après avoir été invité pendant quelques semaines pour la préparation du concours pour la bourse ministérielle j'ai joint le LPMMC en Septembre 2009. Maintenant, on est le 9 août 2012, je peux dire sans doute que c'était un des meilleurs choix de ma vie. J'ai passé trois ans de ma vie dans un environment fabuleux, du point de vue scientifique ainsi que personnel. Trois ans dans un pays qui au début était un pays étranger et qui est devenu le pays où je me sens chez moi. C'est pour ça, que je veux remercier tout l'équipe du LPMMC qui est devenue une petite famille pour moi. Si j'avais des problèmes, soit dans la physique ou avec la bureaucratie, il y avait toujours quelqu'un qui m'a aidé.

Particulièrement je voudrais remercier Anna et Frank, ma directrice/ mon directeur de thèse, "Grazie mille" et "Hartelijk Dank". Vous m'avez appris beaucoup de choses, aussi au-delà de la physique. J'ai bien aimé les heures devant le tableau et votre approche à la science m'a toujours impressionné. Votre disponibilité était extraordinaire et votre façon de surveiller le progrès d'un thésard était de manière exemplaire. Votre excellence et vos idéaux scientifiques m'ont ouvert une porte dans un monde de la recherche parfaite, qui n'est pas du tout évident. Vous êtes des chercheurs comme il faudrait en avoir plus. Encore une fois, MERCI BEAUCOUP!

Le fait que ma vie scientifique était si agréable est aussi à cause de mes collègues du bureau (Gianluca, Arthur, Vitalie, James, Thomas, Andrej et Alexander) et le groupe expérimental de Wiebke Guichard et Olivier Buisson. Particulièrement je voudrais remercier Gianluca qui était mon voisin pendant ces trois années et avec lequel j'ai aussi travaillé sur le projet des jonctions de Josephson.

Également je voudrais remercier les secretaires Michèle, Laurence et Sandrine, qui se sont occupées de moi quand ils y avaient des problèmes avec la bureaucratie. Puisque mon francais n'était pas parfait au début de ma thèse vous étiez une grande aide pour moi. Bien sûr, tous mes amis à Grenoble qui m'ont soutenu et tous les gens que j'ai oubliés en ce moment.

VIII Appendix

A The exact solution

In this section we detail the solution of the stationary single-particle Schrödinger equation (3.5.6). The solution for $x \neq 0$ is a combination of incoming and outgoing plane waves, which should be suitably matched at $x = 0$ using the cusp condition (3.5.10). We search then for a solution $\phi_{j,q}(x) = \phi^{\pm}_{j,q}(x)$ for $x \gtrless 0$ which has the form

$$\begin{array}{rcll} \phi^{-}_{j,q}(x) & = & \frac{1}{\mathcal{N}^{-}}\left(e^{ik_j x} \; + \; \gamma^{-}_j \; e^{-ik_j x}\right) & x \in [-\frac{L}{2}, 0) \\ \phi^{+}_{j,q}(x) & = & \frac{1}{\mathcal{N}^{+}}\left(e^{ik_j x} \; + \; \gamma^{+}_j \; e^{-ik_j x}\right) & x \in [0, \frac{L}{2}] \end{array} \quad . \tag{A.1}$$

The unknowns $k_j, \mathcal{N}^{+}_j, \mathcal{N}^{-}_j, \gamma^{+}_j, \gamma^{-}_j$ are determined fixing the following conditions: TBCs upon an entire rotation around the ring, cusp condition at the position of the barrier and the proper normalization of the single-particle wave function

$$\phi^{-}_{j,q}\left(-\frac{L}{2}\right) = e^{iqL}\phi^{+}_{j,q}\left(\frac{L}{2}\right) \qquad \text{(TBC)} \tag{A.2}$$

$$\frac{\partial}{\partial x}\phi^{-}_{j,q}(x)\Big|_{-\frac{L}{2}} = e^{iqL}\frac{\partial}{\partial x}\phi^{+}_{j,q}(x)\Big|_{\frac{L}{2}} \qquad \text{(TBC)} \tag{A.3}$$

$$\phi^{-}_{j,q}(0) = \phi^{+}_{j,q}(0) \qquad \text{(Cusp Cond.)} \tag{A.4}$$

$$\frac{\partial}{\partial x}\phi^{+}_{j,q}(x)\Big|_{0} - \frac{\partial}{\partial x}\phi^{-}_{j,q}(x)\Big|_{0} = 2\lambda\phi_{j,q}(0) \qquad \text{(Cusp Cond.)} \tag{A.5}$$

$$\int_{-L/2}^{L/2} dx|\phi_{j,q}(x)| = 1 \qquad \text{(Normalization)}\ , \tag{A.6}$$

where $\lambda = \frac{m\ U_0}{\hbar^2}$. We find

$$\begin{aligned}
\phi^{-}_{j,q}(x) &= e^{iq\frac{L}{2}}\left(e^{ik_j(x+\frac{L}{2})} + A(k_j,q)\, e^{-ik_j(x+\frac{L}{2})}\right) \qquad x\in[-\tfrac{L}{2},0) \\
\phi^{+}_{j,q}(x) &= e^{-iq\frac{L}{2}}\left(e^{ik_j(x-\frac{L}{2})} + A(k_j,q)\, e^{-ik_j(x-\frac{L}{2})}\right) \qquad x\in[0,\tfrac{L}{2}]
\end{aligned} \quad , \tag{A.7}$$

with

$$k_j = \lambda\frac{\sin(k_jL)}{\cos(qL)-\cos(k_jL)} \tag{A.8}$$

$$A(k_j,q) = \frac{\sin\left((k_j+q)\frac{L}{2}\right)}{\sin\left((k_j-q)\frac{L}{2}\right)} \tag{A.9}$$

$$\mathcal{N}_j = \sqrt{L\left(1+A^2(k_j,q)+2A(k_j,q)\frac{\sin(k_jL)}{k_jL}\right)}\,. \tag{A.10}$$

These orbitals form a complete set for the case $q \neq \frac{\pi\, n}{L}$, where n is an integer. The wave vectors are determined by the transcendental equation Eq. (A.8). For the other two cases, i.e., a stirring velocity of $q = \frac{2\pi n}{L}$ and $q = \frac{(2n+1)\pi}{L}$, these orbitals are purely even functions and thus form only half of the full set. For the two special cases a seperate analysis is needed.

- $q = \frac{2\pi n}{L}$

$$\begin{aligned}
\phi^{e}_{j,q}(x) &= \begin{cases} \phi^{-,e}_{j,q}(x) = \frac{(-)^n}{\mathcal{N}_j}\left(e^{ik_j(x+\frac{L}{2})} + e^{-ik_j(x+\frac{L}{2})}\right) & x\in[-\frac{L}{2},0] \\ \phi^{+,e}_{j,q}(x) = \frac{(-)^n}{\mathcal{N}_j}\left(e^{ik_j(x-\frac{L}{2})} + e^{-ik_j(x-\frac{L}{2})}\right) & x\in[0,\frac{L}{2}] \end{cases} \\
&= (-)^n\frac{2}{\mathcal{N}_j}\cos\left(k_j(|x|-\frac{L}{2})\right)
\end{aligned} \tag{A.11}$$

with

$$k_j = \lambda\frac{\cos\left(k_j\frac{L}{2}\right)}{\sin\left(k_j\frac{L}{2}\right)} \tag{A.12}$$

$$\mathcal{N}_j = \sqrt{2L\left(1+\frac{\sin(k_jL)}{k_jL}\right)} \tag{A.13}$$

$$\phi^{o}_{l}(x) = i(-)^{l+n}\sqrt{\frac{2}{L}}\sin\left(\frac{2\pi l}{L}x\right) \qquad \text{where} \qquad l=1,2,3... \tag{A.14}$$

We have thus a set of odd wave functions that fulfill the cusp-condition by construction since they vanish at the position of the barrier. Therefore, there is neither a dependence on the barrier strength λ nor on the quasi-momentum q. The lowest-lying orbital is the even orbital with $j = 1$. One can successively fill up the Fermi-sea by placing particles into the next higher state, alternating between even and odd states. For $n = 0$ we obtain the initial state of the problem, i.e. a stationary barrier localized at $x = 0$.

In the case of the non-adiabatic set into motion of the barrier it is possible to obtain the overlap coefficients (3.5.8) for the single-particle wave functions using Eq.(A.11) and Eq.(A.14) and respectively Eqs.(3.5.14) and (3.5.15), similar to the calculation presented in the main text. Since a distiction between even and odd orbitals is necessary there are four overlap coefficients instead of only two

$$\begin{aligned} c_{jl}^{ee} &= \frac{L}{\mathcal{N}_j \mathcal{N}_l} \left\{ J_0 \left[(k_j + k_l + q)\frac{L}{2} \right] + J_0 \left[(k_j - k_l + q)\frac{L}{2} \right] \right. \\ &\quad \left. + J_0 \left[(k_j + k_l - q)\frac{L}{2} \right] + J_0 \left[(k_j - k_l - q)\frac{L}{2} \right] \right\} \end{aligned} \tag{A.15}$$

$$\begin{aligned} c_{jl}^{oo} &= \frac{(-)^{j+l+n}}{2} \left\{ J_0 \left[(\frac{2\pi j}{L} - \frac{2\pi l}{L} - q)\frac{L}{2} \right] + J_0 \left[(\frac{2\pi j}{L} - \frac{2\pi l}{L} + q)\frac{L}{2} \right] \right. \\ &\quad \left. - J_0 \left[(\frac{2\pi j}{L} + \frac{2\pi l}{L} - q)\frac{L}{2} \right] - J_0 \left[(\frac{2\pi j}{L} + \frac{2\pi l}{L} + q)\frac{L}{2} \right] \right\} \end{aligned} \tag{A.16}$$

$$\begin{aligned} c_{jl}^{eo} &= \frac{1}{\mathcal{N}_j} \sqrt{\frac{L}{2}} \left\{ J_0 \left[(k_j - \frac{2\pi l}{L} + q)\frac{L}{2} \right] + J_0 \left[(k_j + \frac{2\pi l}{L} - q)\frac{L}{2} \right] \right. \\ &\quad \left. - J_0 \left[(k_j + \frac{2\pi l}{L} + q)\frac{L}{2} \right] - J_0 \left[(k_j - \frac{2\pi l}{L} - q)\frac{L}{2} \right] \right\} \end{aligned} \tag{A.17}$$

$$\begin{aligned} c_{jl}^{oe} &= \frac{1}{\mathcal{N}_l} \sqrt{\frac{L}{2}} \left\{ J_0 \left[(\frac{2\pi j}{L} + k_l + q)\frac{L}{2} \right] + J_0 \left[(\frac{2\pi j}{L} - k_l + q)\frac{L}{2} \right] \right. \\ &\quad \left. - J_0 \left[(\frac{2\pi j}{L} + k_l - q)\frac{L}{2} \right] - J_0 \left[(\frac{2\pi j}{L} - k_l - q)\frac{L}{2} \right] \right\} \end{aligned} \tag{A.18}$$

with with the integers $j, l, n = 1, 2, 3....$

- $q = \frac{(2n+1)\pi}{L}$

$$\begin{aligned}\phi^{e}_{j,q}(x) &= \begin{cases} \phi^{-,e}_{j,q}(x) = \frac{i(-)^n}{\tilde{\mathcal{N}}_j}\left(e^{i\tilde{k}_j(x+\frac{L}{2})} - e^{-i\tilde{k}_j(x+\frac{L}{2})}\right) & x \in [-\frac{L}{2}, 0] \\ \phi^{+,e}_{j,q}(x) = -\frac{i(-)^n}{\tilde{\mathcal{N}}_j}\left(e^{i\tilde{k}_j(x-\frac{L}{2})} - e^{-i\tilde{k}_j(x-\frac{L}{2})}\right) & x \in [0, \frac{L}{2}] \end{cases} \\ &= i(-)^n \frac{2}{\tilde{\mathcal{N}}_j} \sin\left(\tilde{k}_j(|x| - \frac{L}{2})\right) \end{aligned} \tag{A.19}$$

with

$$\tilde{k}_j = -\lambda \frac{\sin\left(\tilde{k}_j \frac{L}{2}\right)}{\cos\left(\tilde{k}_j \frac{L}{2}\right)} \tag{A.20}$$

$$\tilde{\mathcal{N}}_j = \sqrt{2L\left(1 - \frac{\sin(\tilde{k}_j L)}{\tilde{k}_j L}\right)} \tag{A.21}$$

$$\phi^{o}_{l}(x) = i(-)^{l+n+1}\sqrt{\frac{2}{L}} \sin\left(\frac{(2l+1)\pi}{L}x\right) \qquad \text{where} \qquad l = 0, 1, 2... \tag{A.22}$$

The lowest-lying orbital is the odd orbital with $l = 1$. One can successively fill up the Fermi-sea by placing particles into the next higher state, alternating between odd and even states.

In the case of the non-adiabatic stirring it is possible to obtain the overlap coefficients (3.5.8) for the single-particle wave functions using Eq.(A.19) and Eq.(A.22) and respectively Eqs.(3.5.14) and (3.5.15) read

$$\begin{aligned} c^{ee}_{jl} &= \frac{L}{\tilde{\mathcal{N}}_j \mathcal{N}_l}\left\{ J_0\left[(\tilde{k}_j + k_l + q)\frac{L}{2}\right] + J_0\left[(\tilde{k}_j - k_l + q)\frac{L}{2}\right] \right. \\ &\left. - J_0\left[(\tilde{k}_j + k_l - q)\frac{L}{2}\right] - J_0\left[(\tilde{k}_j - k_l - q)\frac{L}{2}\right]\right\} \end{aligned} \tag{A.23}$$

$$\begin{aligned} c^{oo}_{jl} &= \frac{(-)^{j+l+n+1}}{2}\left\{ J_0\left[(\frac{(2j+1)\pi}{L} - \frac{2\pi l}{L} + q)\frac{L}{2}\right] \right. \\ &+ J_0\left[(\frac{(2j+1)\pi}{L} - \frac{2\pi l}{L} - q)\frac{L}{2}\right] - J_0\left[(\frac{(2j+1)\pi}{L} + \frac{2\pi l}{L} + q)\frac{L}{2}\right] \\ &\left. - J_0\left[(\frac{(2j+1)\pi}{L} + \frac{2\pi l}{L} - q)\frac{L}{2}\right]\right\} \end{aligned} \tag{A.24}$$

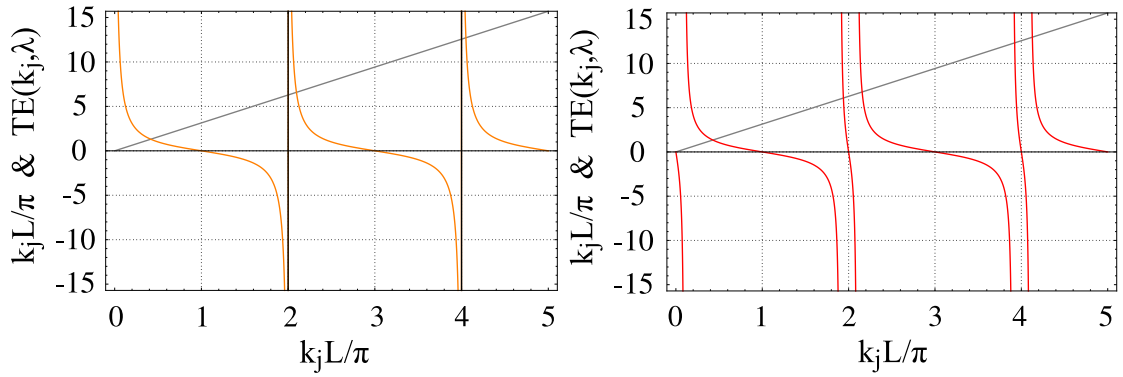

Figure VIII.1: Left panel: The function $\mathrm{TE}(k_j, q) = \lambda \cos(k_j L/2) / \sin(k_j L/2)$ (yellow curve) given by Eq. (A.12) and k_j (gray curve) as a function of k_j at $q = n\pi/L$ and for $\lambda L = 1$. The crossing points of the gray and the yellow curve yield the solution of the transcendental equation, i.e. the even eigenstates are found. The crossing points of the gray curve with the black vertical lines yield the odd eigenstates. It can be seen that the lowest energy eigenstate (the ground state) is a solution of the transcendental equation which means an even state. Right panel: The function $\mathrm{TE}(k_j, q) = \lambda \sin(k_j L)/\Big(\cos(qL) - \cos(k_j L)\Big)$ (red curve) given by Eq. (A.8) and k_j (gray curve) as a function of k_j at $q = n\pi/L + 0.1\pi/L$ and for $\lambda L = 1$. The crossing points of the gray and the red curve yield the solution of the transcendental equation, representing a full set of eigenstates. In this general case it is not possible to distinguish between purely even and purely odd states. Here, the ground state is close to an even state, since q is very close to $n\pi/L$.

$$
\begin{aligned}
c_{jl}^{eo} &= \frac{1}{\tilde{\mathcal{N}}_j}\sqrt{\frac{L}{2}}\Bigg\{ J_0\left[(\tilde{k}_j - \frac{2\pi l}{L} + q)\frac{L}{2}\right] + J_0\left[(\tilde{k}_j - \frac{2\pi l}{L} - q)\frac{L}{2}\right] \\
&\quad - J_0\left[(\tilde{k}_j + \frac{2\pi l}{L} - q)\frac{L}{2}\right] - J_0\left[(\tilde{k}_j + \frac{2\pi l}{L} + q)\frac{L}{2}\right]\Bigg\} \qquad \text{(A.25)} \\
c_{jl}^{oe} &= \frac{1}{\mathcal{N}_l}\sqrt{\frac{L}{2}}\Bigg\{ J_0\left[(\frac{(2j+1)\pi}{L} + k_l + q)\frac{L}{2}\right] \\
&\quad + J_0\left[(\frac{(2j+1)\pi}{L} - k_l + q)\frac{L}{2}\right] + J_0\left[(\frac{(2j+1)\pi}{L} + k_l - q)\frac{L}{2}\right] \\
&\quad + J_0\left[(\frac{(2j+1)\pi}{L} - k_l - q)\frac{L}{2}\right]\Bigg\} \qquad \text{(A.26)}
\end{aligned}
$$

with with the integers $j, l, n = 1, 2, 3....$

The transition from an even ground state for $q = 2\pi n/L$ to a ground state that is neither even nor odd for $2\pi n/L < q < (2n+1)\pi/L$ and further to an odd ground state for $q = (2n+1)\pi/L$ can be seen in Figs. VIII.1 and VIII.2, where the graphical solution of the transcendental equation is plotted. The dependence of the wave vector k_j on the barrier momentum q can be seen in Fig. III.2, including both even and odd

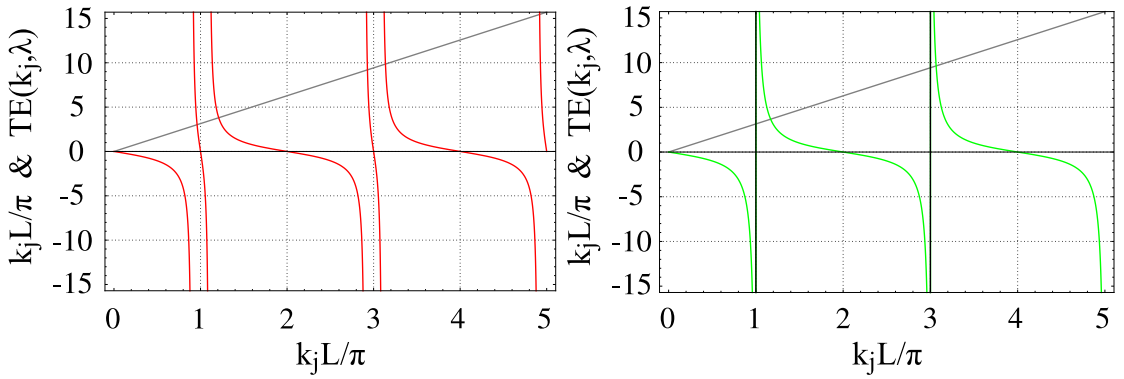

Figure VIII.2: Left panel: The function $\mathrm{TE}(k_j, q) = \lambda \sin(k_j L) / \Big(\cos(qL) - \cos(k_j L)\Big)$ (red curve) given by Eq. (A.8) and k_j (gray curve) as a function of k_j at $q = n\pi/L + 0.9\pi/L$ and for $\lambda L = 1$. The crossing points of the gray and the red curve yield the solution of the transcendental equation, representing a full set of eigenstates. In this general case it is not possible to distinguish between purely even and purely odd states. Here, the ground state is close to an odd state, since q is very close to $(2n+1)\pi/L$. Right panel: The function $\mathrm{TE}(k_j, q) = -\lambda \sin(k_j L/2) / \cos(k_j L/2)$ (green curve) given by Eq. (A.20) and k_j (gray curve) as a function of k_j at $q = (2n+1)\pi/L$ and for $\lambda L = 1$. The crossing points of the gray and the green curve yield the solution of the transcendental equation, i.e. the even eigenstates are found. The crossing points of the gray curve with the black vertical lines yield the odd eigenstates. It can be seen that the lowest energy eigenstate (the ground state) is a the crossing of the gray line with the first vertical black line, i.e. the odd eigenstate with $k_l = \pi/L$.

states for the special case when q is an integer multiple of π/L.

B The square barrier

In a similar approach as presented in Appendix A it is possible to find the solution of the stationary single-particle Schrödinger equation when the delta-barrier potential is replaced by a square-barrier potential $U_{barr}(x) = U_0^{(s)}$ for $|x| < \ell/2$ and zero otherwise. The solution in the three regions is a combination of incoming and outgoing plane waves, which should be suitably matched at $x = \pm\ell/2$. We search then for a solution $\phi_{j,q}(x) = \phi_{j,q}^{(1),(2),(3)}(x)$ for $x < -\ell/2$, $-\ell/2 < x < \ell/2$ and $x > \ell/2$ which has the form

$$\phi_{j,q}(x) = \begin{cases} \phi_{j,q}^{(1)}(x) = \frac{1}{\mathcal{N}^{(1)}} \left(e^{ik_j^{(s)}x} \; + \; \gamma_j^{(1)} \; e^{-ik_j^{(s)}x} \right) & x \in [-\frac{L}{2}, -\frac{\ell}{2}) \\ \phi_{j,q}^{(2)}(x) = \frac{1}{\mathcal{N}^{(2)}} \left(e^{ik_j^{(2)}x} \; + \; \gamma_j^{(2)} \; e^{-ik_j^{(2)}x} \right) & x \in [-\frac{\ell}{2}, \frac{\ell}{2}) \\ \phi_{j,q}^{(3)}(x) = \frac{1}{\mathcal{N}^{(3)}} \left(e^{ik_j^{(s)}x} \; + \; \gamma_j^{(3)} \; e^{-ik_j^{(s)}x} \right) & x \in [\frac{\ell}{2}, \frac{L}{2}) \end{cases} . \quad \text{(B.1)}$$

The single-particle wave vector in the region of the barrier is directly determined from the knowledge of the single-particle wave vector in the region without barrier. Moreover, depending on the energy of the particle it is either real or imaginary, resulting in a plane wave with reduced energy or an exponentially decaying wave function, respectively. Its value is determined through

$$k_j^{(2)} = \sqrt{(k_j^{(s)})^2 - 2\lambda^{(s)}} \qquad \text{for} \qquad (k_j^{(s)})^2 > 2\lambda^{(s)} \quad \text{(B.2)}$$

$$k_j^{(2)} = i\sqrt{2\lambda^{(s)} - (k_j^{(s)})^2} \qquad \text{for} \qquad (k_j^{(s)})^2 < 2\lambda^{(s)} \; . \quad \text{(B.3)}$$

Applying TBCs at $x = \pm L/2$, a continuity condition at $x = \pm\ell/2$ for both orbitals and their derivative and a proper normalization, the unknowns $\mathcal{N}^{(1)}$, $\mathcal{N}^{(2)}$, $\mathcal{N}^{(3)}$, $\gamma^{(1)}$,$\gamma^{(2)}$, $\gamma^{(3)}$ and $k_j^{(s)}$ are readily obtained. The single-particle wave vector $k_j^{(s)}$ is, similar to the delta-barrier potential, determined by a transcendental equation

$$\frac{2k_j^{(s)}k_j^{(2)}}{(k_j^{(s)} + k_j^{(2)})^2} = \frac{\sin[k_j^{(s)}(L-\ell)]\sin[k_j^{(2)}\ell]}{\cos[(k_j^{(s)} + k_j^{(2)})\ell - k_j^{(s)}L] - \cos[qL]} \quad \text{(B.4)}$$

and again depends both on the barrier strength and the quasi-momentum q. The weights of the plane waves in Eq.(B.1) and the normalization yield

$$\gamma^{(1)} = \gamma^{(s)} e^{-ik_j^{(s)}L} \tag{B.5}$$

$$\gamma^{(2)} = \frac{4k_j^{(s)}k_j^{(2)}}{(k_j^{(s)})^2-(k_j^{(2)})^2}\frac{\sin[(k_j^{(s)}-q)L/2-(k_j^{(s)}+k_j^{(2)})\ell/2]}{\sin[k_j^{(s)}(L-\ell)]} \times e^{i(k_j^{(s)}+q)L/2}e^{-i(k_j^{(s)}+k_j^{(2)})\ell/2} - \frac{k_j^{(s)}+k_j^{(2)}}{k_j^{(s)}-k_j^{(2)}}e^{-ik_j^{(2)}\ell} \tag{B.6}$$

$$\gamma^{(3)} = \gamma^{(s)} e^{ik_j^{(s)}L} \tag{B.7}$$

$$\gamma^{(s)} = \frac{k_j^{(s)}+k_j^{(2)}}{k_j^{(2)}-k_j^{(s)}}\left[\frac{\sin[k_j^{(s)}(L-\ell)]}{\sin[(k_j^{(s)}-q)L/2-(k_j^{(s)}+k_j^{(2)})\ell/2]} \times e^{-i(k_j^{(s)}-q)L/2}e^{i(k_j^{(s)}+k_j^{(2)})\ell/2} - e^{ik_j^{(s)}L}e^{ik_j^{(s)}\ell}\right] \tag{B.8}$$

$$\mathcal{N}^{(1)} = \mathcal{N}^{(s)} e^{-i(k_j^{(s)}+q)L/2} \tag{B.9}$$

$$\mathcal{N}^{(2)} = \mathcal{N}^{(s)}\frac{2k_j^{(2)}}{k_j^{(s)}+k_j^{(2)}}\frac{\sin[(k_j^{(s)}-q)L/2-(k_j^{(s)}+k_j^{(2)})\ell/2]}{\sin[k_j^{(s)}(L-\ell)]} \tag{B.10}$$

$$\mathcal{N}^{(3)} = \mathcal{N}^{(s)} e^{i(k_j^{(s)}+q)L/2} \tag{B.11}$$

$$\mathcal{N}^{(s)} = \left[\left(1+|\gamma^{(s)}|^2\right)(L-\ell) + \frac{2\mathsf{Re}[\gamma^{(s)}]}{k_j^{(s)}}\sin(k_j^{(s)}(L-\ell)) + \frac{(k_j^{(s)}+k_j^{(2)})^2}{4(k_j^{(2)})^2}\frac{\sin^2[k_j^{(s)}(L-\ell)]}{\sin^2[(k_j^{(s)}-q)L/2-(k_j^{(s)}+k_j^{(2)})\ell/2]} \times\left(1+|\gamma^{(s)}|^2\ell + \frac{2\mathsf{Re}[\gamma^{(2)}]}{k_j^{(2)}}\sin(k_j^{(2)}\ell)\right)\right]^{1/2} \tag{B.12}$$

C The particle current

In this appendix we show that the particle-current density for the TG gas coincides with the particle-current density of the mapped Fermi gas. In order to improve readability we leave out the time-dependence in the derivation. Starting from the current density operator

$$\hat{j}(x) = -\frac{i\hbar}{2m}\sum_{l=1}^{N}\left(\delta(x-x_l)\frac{\partial}{\partial x_l} + \frac{\partial}{\partial x_l}\delta(x-x_l)\right) \ , \tag{C.1}$$

the particle current density is given by the quantum average on the system state, i.e.

$$j(x) \ = \ \langle\Psi_B|\hat{j}(x)|\Psi_B\rangle = \int dx_1...dx_N \Psi_B^*(x_1...x_N)\hat{j}(x)\Psi_B(x_1...x_N) \ . \tag{C.2}$$

Partial integration gives

$$\begin{aligned} j(x) \ &= \ -\frac{i\hbar}{2m}N\int dx_1...dx_{N-1} \\ &\quad \times\left[\Psi_B^*(x_1...x_{N-1},x)\frac{\partial}{\partial x}\Psi_B(x_1...x_{N-1},x)\right. \\ &\quad \left. -\left(\frac{\partial}{\partial x}\Psi_B^*(x_1...x_{N-1},x)\right)\Psi_B(x_1...x_{N-1},x)\right] \ . \end{aligned} \tag{C.3}$$

Using the TG many-body wave function of Eq.(3.4.3),

$$\begin{aligned} \Psi_{TG}(x_1,...x_N) \ &= \ \mathcal{A}(x_1,...x_N)\frac{1}{\sqrt{N!}}\det[\psi_l(x_m)] \\ &= \ \frac{1}{\sqrt{N!}}\prod_{1\le j<\ell\le N}\mathrm{sign}(x_j-x_\ell)\sum_{\mathcal{P}\in S_N}\epsilon(\mathcal{P})\prod_{j=1}^{N}\psi_j(x_{\mathcal{P}(j)}) \ , \end{aligned} \tag{C.4}$$

where S_N is the group of all permutations on N objects and $\epsilon(\mathcal{P})$ is the signature of the permutation $\mathcal{P}$, the particle current density reduces to

$$\begin{aligned} j(x) \ &= \ -\frac{i\hbar}{2m}\frac{N}{N!}\int dx_1...dx_{N-1}\sum_{\mathcal{P},\mathcal{Q}\in S_N}\epsilon(\mathcal{P})\epsilon(\mathcal{Q})\left(\prod_{j=1}^{N-1}\psi_{\mathcal{P}(j)}^*(x_j)\psi_{\mathcal{Q}(j)}(x_j)\right) \\ &\quad \times\prod_{k=1}^{N-1}\left[\mathrm{sign}(x_k-x)\psi_{\mathcal{P}(N)}^*(x_N)\left(\frac{\partial}{\partial x}\mathrm{sign}(x_k-x)\psi_{\mathcal{Q}(N)}(x_N)\right)\right. \\ &\quad \left. -\left(\frac{\partial}{\partial x}\mathrm{sign}(x_k-x)\psi_{\mathcal{P}(N)}^*(x_N)\right)\mathrm{sign}(x_k-x)\psi_{\mathcal{Q}(N)}(x_N)\right] \\ &= \ -\frac{i\hbar}{2m}\sum_{k=1}^{N}\left[\psi_k^*(x)\left(\frac{\partial}{\partial x}\psi_k(x)\right)-\left(\frac{\partial}{\partial x}\psi_k^*(x)\right)\psi_k(x)\right] \\ &= \ \frac{\hbar}{m}\ \mathrm{Im}\ \sum_{l=1}^{N}\psi_l^*(x)\ \frac{\partial}{\partial x}\ \psi_l(x) \ . \end{aligned} \tag{C.5}$$

Here we used that $\int dy\delta(x-y)\mathrm{sign}(x-y)=0$.
Moreover we also want the give the expressions for the amplitudes $F_{ij}=\langle\phi_i|\partial_x|\phi_j\rangle$ occurring in Eq.(4.2.15) and (4.2.16) for the special case of $q=n\pi/L$, with integer n, using Eqs.(A.11) and (A.14) as single praticle orbitals for $q=2n\pi/L$. They read

$$F_{jl}^{eo} = \frac{(-1)^{n+l}2\pi l}{\mathcal{N}_j}\sqrt{\frac{2}{L}}\left\{J_0\left[(k_j+\frac{2\pi l}{L})\frac{L}{2}\right]+J_0\left[(k_j-\frac{2\pi l}{L})\frac{L}{2}\right]\right\} \quad \text{(C.6)}$$

$$F_{jl}^{oe} = \frac{(-1)^{n+j}k_l}{\mathcal{N}_l}\sqrt{2L}\left\{J_0\left[(k_l+\frac{2\pi j}{L})\frac{L}{2}\right]-J_0\left[(k_l-\frac{2\pi j}{L})\frac{L}{2}\right]\right\}\ . \quad \text{(C.7)}$$

For $q=(2n+1)\pi/L$ we use Eqs.(A.19) and (A.22) as single praticle orbitals and obtain

$$F_{jl}^{eo} = \frac{(-1)^{n+l}(2l+1)\pi}{\tilde{\mathcal{N}}_j}\sqrt{\frac{2}{L}}\left\{J_0\left[(\tilde{k}_j+\frac{(2l+1)\pi}{L})\frac{L}{2}\right]\right. \\ \left. -J_0\left[(\tilde{k}_j-\frac{(2l+1)\pi}{L})\frac{L}{2}\right]\right\} \quad \text{(C.8)}$$

$$F_{jl}^{oe} = \frac{(-1)^{n+j}\tilde{k}_l}{\tilde{\mathcal{N}}_l}\sqrt{2L}\left\{J_0\left[(\tilde{k}_l+\frac{(2j+1)\pi}{L})\frac{L}{2}\right]\right. \\ \left. +J_0\left[(\tilde{k}_l-\frac{(2j+1)\pi}{L})\frac{L}{2}\right]\right\} \quad \text{(C.9)}$$

with with the integers $j,l,n=1,2,3....$ For the combination of two even or two odd orbitals the amplitudes $F_{ij}=\langle\phi_i|\partial_x|\phi_j\rangle$ equally vanish.

D The one-body density matrix

In this appendix we calculate the OBDM for the TG gas in terms of the single-particle wave functions of Eq.(3.5.5), following the derivation of [112]. For simplicity we omit the explicite time dependence of the state since we may easily plug it back if needed. The OBDM was defined upon integrating out $N-1$ particle coordinates from the density matirx $\rho_B(t) = |\Psi_B\rangle\langle\Psi_B|$. The OBDM reads

$$\rho_B(x,y) = N \int dx_1....dx_{N-1} \Psi^*_{TG}(x_1...x_{N-1},x)\Psi_{TG}(x_1...x_{N-1},y) \ , \tag{D.1}$$

with the TG many-body wave function of Eq.(C.4). Substituting this into Eq.(D.1) one obtains

$$\begin{aligned}
\rho_B(x,y) &= \frac{N}{N!}\int dx_1....dx_{N-1} \prod_{j=1}^{N-1} \mathrm{sign}(x-x_j)\mathrm{sign}(y-x_j) \\
&\qquad \times \sum_{\mathcal{P}\in S_N} \epsilon(\mathcal{P})\psi^*_{\mathcal{P}(N)}(x)\left(\prod_{j=1}^{N-1}\psi^*_{\mathcal{P}(j)}(x_j)\right) \\
&\qquad\qquad \times \sum_{\mathcal{Q}\in S_N} \epsilon(\mathcal{Q})\psi_{\mathcal{Q}(N)}(y)\left(\prod_{j=1}^{N-1}\psi_{\mathcal{Q}(j)}(x_j)\right) \\
&= \frac{1}{(N-1)!}\sum_{\substack{\mathcal{P}\in S_N \\ \mathcal{Q}\in S_N}} \epsilon(\mathcal{P})\epsilon(\mathcal{Q})\psi^*_{\mathcal{P}(N)}(x)\psi_{\mathcal{Q}(N)}(y) \\
&\qquad \times \left(\prod_{j=1}^{N-1}\mathscr{J}_{\mathcal{P}(j),\mathcal{Q}(j)}(x,y)\right) \ ,
\end{aligned} \tag{D.2}$$

with

$$\begin{aligned}
\mathscr{J}_{\mathcal{P}(j),\mathcal{Q}(j)}(x,y) &= \int_{-L/2}^{L/2} dx_j \ \mathrm{sign}(x-x_j)\mathrm{sign}(y-x_j)\psi^*_{\mathcal{P}(j)}(x_j)\psi_{\mathcal{Q}(j)}(x_j) \\
&= \delta_{\mathcal{P}(j),\mathcal{Q}(j)} \mp 2\int_x^y dx_j \ \psi^*_{\mathcal{P}(j)}(x_j)\psi_{\mathcal{Q}(j)}(x_j) \ .
\end{aligned} \tag{D.3}$$

The upper sign is for $x<y$ and the lower one for $x>y$. Without loss of generality we will assume that $x<y$ since the density matrix is hermitian and hence fully determined.

The OBDM thus becomes

$$\begin{aligned}\rho_B(x,y) &= \frac{1}{(N-1)!}\sum_{k,\ell=1}^{N}(-)^{k+\ell}\psi_k^*(x)\psi_\ell(y) \\ &\quad\times\sum_{\substack{\mathcal{P}\in S_{N-1}\\ \mathcal{Q}\in S_{N-1}}}\epsilon(\mathcal{P})\epsilon(\mathcal{Q})\left(\prod_{\substack{j=1\\ \mathcal{P}(j)\neq k,\mathcal{Q}(j)\neq\ell}}^{N-1}\mathscr{J}_{\mathcal{P}(j),\mathcal{Q}(j)}(x,y)\right) \\ &= \sum_{k,\ell=1}^{N}\psi_k^*(x)\psi_\ell(y)(-)^{k+\ell}\det[M_{k,\ell}(x,y)] \qquad \text{(D.4)}\end{aligned}$$

where $M_{k,\ell}(x,y)$ is a minor of matrix

$$P_{ij}(x,y)=\delta_{i,j}-2\int_x^y dx\,'\;\psi_i^*(x\,')\psi_j(x\,')\;, \qquad \text{(D.5)}$$

after crossing the kth row and the ℓth column. In combination with the prefactor $(-)^{k+\ell}$ the determinant of matrix $M_{k,\ell}(x,y)$ gives the cofactor, $(-)^{k+\ell}\det[M_{k,\ell}]$ of matrix $\mathbf{P}$. Defining matrix $A_{k,\ell}(x,y)$ by

$$\mathbf{A}(x,y)=\Big(\mathbf{P}^{-1}(x,y)\Big)^T\det\Big(\mathbf{P}(x,y)\Big)\;, \qquad \text{(D.6)}$$

the OBDM can thus be written in the form

$$\rho_B(x,y)=\sum_{i,j=1}^{N}\psi_i^*(x)A_{ij}(x,y)\psi_j(y)\;. \qquad \text{(D.7)}$$

Bibliography

[1] G. Sagnac. The demonstration of the luminiferous aether by an interferometer in uniform rotation. *C.R. Acad. Sci. 157 708*, 1913.

[2] J. Dowling. Correlated input-port, matter-wave interferometer: Quantum-noise limits to the atom-laser gyroscope. *Phys. Rev. A 57, 4736*, 1998.

[3] http://www.deutsches-museum.de/sammlungen/ausgewaehlte-objekte/meisterwerke-iv/pendel.

[4] http://hyperphysics.phy-astr.gsu.edu/hbase/gyr.html.

[5] http://www.optique-ingenieur.org/en/courses/OPI_ang_M02_C05/co/Contenu_26.html.

[6] M. O. Scully and J. P. Dowling. Quantum-noise limits to matter-wave interferometry. *Phys. Rev. A 48, 3186*, 1993.

[7] T. Kinoshita, T. Wenger and D. S. Weiss. Observation of a One-Dimensional Tonks-Girardeau Gas. *Science 305, 1125*, 2004.

[8] B. Paredes et al. Tonks-Girardeau gas of ultracold atops in an optical lattice. *Nature 429, 277*, 2004.

[9] M. F. Andersen et al. Quantized Rotation of Atoms from Photons with Orbital Angular Momentum. *Phys. Rev. Lett. 97, 170406*, 2006.

[10] H. P. Buchler, V. B. Geshkenbein and G. Blatter. Superfluidity versus Bloch Oscillations in Confined Atomic Gases. *Phys. Rev. Lett. 87 100403*, 2001.

[11] E. H. Lieb and W. Liniger. Exact Analysis of an interacting Bose Gas I, The General Solution and the Ground State. *Phys. Rev 130, 1605*, 1963.

[12] E. H. Lieb. Exact Analysis of an interacting Bose Gas II, The Excitation Spectrum. *Phys. Rev 130, 1616*, 1963.

[13] M. D. Girardeau. Relationship between Systems of Impenetrable Bosons and Fermions in One Dimension. *J. Math. Phys. 1, 516*, 1960.

[14] M. D. Girardeau and E. M. Wright. Dark Solitons in a One-Dimensional Condensate of Hard Core Bosons. *Phys. Rev. Lett. 84 5691*, 2000.

[15] S. Gupta et al. Bose-Einstein Condensation in a Circular Waveguide. *Phys. Rev. Lett 95, 143201*, 2005.

[16] A. Ramanathan et al. Superflow in a Toroidal Bose-Einstein Condensate: An Atom Circuit with a Tunable Weak Link. *Phys. Rev. Lett. 106, 130401*, 2011.

[17] B. E. Sherlock et al. Time-averaged adiabatic ring potential for ultracold atoms. *Phys. Rev. A 83, 043408*, 2011.

[18] S. Moulder et al. Quantised superflow glitches in an annular Bose-Einstein condensate. *arXiv:1112.0334v2*, 2012.

[19] R. Kanamoto, L. D. Carr and M. Ueda. Topological Winding and Unwinding in Metastable Bose-Einstein Condensates. *Phys. Rev. Lett 100, 060401*, 2008.

[20] R. Kanamoto, L. D. Carr and M. Ueda. Metastable quantum phase transitions in a periodic one-dimensional Bose gas: Mean-field and Bogoliubov analysis. *Phys. Rev. A 79 063616*, 2009.

[21] R. Kanamoto, L. D. Carr and M. Ueda. Metastable quantum phase transitions in a periodic one-dimensional Bose gas: II Many-body theory. *Phys. Rev. A 81 023625*, 2010.

[22] R. Kanamoto, L. D. Carr and M. Ueda. Metastable quantum phase transitions in a one-dimensional Bose gas. *arXiv:1005.0656v1*, 2010.

[23] D. W. Hallwood, T. Ernst and J. Brand. Robust mesoscopic superposition of strongly correlated ultracold atoms. *Phys. Rev. A 82 063623*, 2010.

[24] D. W. Hallwood and J. Brand. Engineering mesoscopic superpositions of superfluid flow. *Phys. Rev. A 84 043620*, 2011.

[25] J. J. Cooper et al. Robust Quantum Enhanced Phase Estimation in a Multimode Interferometer. *Phys. Rev. Lett 108 130402*, 2012.

[26] E. M. Lifshitz and L. P. Pitaevskii. *Statistical Physics, Part II*. Butterworth-Heinemann, Oxford 1980.

[27] Yu. Kagan, N. V. Prokof'ev and B. V. Svistunov. Supercurrent stability in a quasi-one-dimensional weakly interacting Bose gas. *Phys. Rev. A 61 045601*, 2000.

[28] P. Leboeuf and N. Pavloff. Bose-Einstein beams: Coherent propagation through a guide. *Phys. Rev. A 64 033602*, 2001.

[29] N. Pavloff. Breakdown of superfluidity of an atom laser past an obstacle. *Phys. Rev. A 66 013610*, 2002.

[30] R. Citro, A. Minguzzi and F. W. J. Hekking. Quantum stirring as a probe of superfluidlike behavior in interacting one-dimensional Bose gases. *Phys. Rev. B 79 172505*, 2009.

[31] G. E. Astrakharchik and L. P. Pitaevskii. Motion of a heavy impurity through a Bose-Einstein condensate. *Phys. Rev. A 70, 013608*, 2004.

[32] S. Palzer et al. Quantum Transport through a Tonks-Girardeau Gas. *Phys. Rev. Lett. 103 150601*, 2009.

[33] J. Mun et al. Phase Diagram for a Bose-Einstein Condensate Moving in an Optical Lattice. *Phys. Rev. Lett. 99 150604*, 2009.

[34] L. Pezzé and A. Smerzi. Entanglement, Nonlinear Dynamics, and the Heisenberg Limit. *Phys. Rev. Lett. 102 100401*, 2009.

[35] M. A. Nielsen and I. L. Chuang. *Quantum Computation and Quantum Information*. Cambridge University Press, Cambridge 2000.

[36] S. Deléglise et al. Reconstruction of non-classical cavity field states with snapshots of their decoherence. *Nature 455 510*, 2008.

[37] D. Leibfried et al. Creation of a six-atom Schrodinger cat state. *Nature 438 639*, 2005.

[38] H. Häffner et al. Scalable multiparticle entanglement of trapped ions. *Nature 438 643*, 2005.

[39] Y. Aharonov and D. Bohm. Significance of Electromagnetic Potentials in the Quantum Theory. *Phys. Rev. 115, 485*, 1959.

[40] M. Olshanii. Atomic Scattering in the Presence of an External Confinement and a Gas of Impenetrable Bosons. *Phys. Rev, Lett 81, 938*, 1998.

[41] G. E. Astrakharchik et al. Quasi-One-Dimensional Bose Gases with a Large Scattering Length. *Phys. Rev. Lett 92, 030402*, 2004.

[42] E. P. Gross. Structure of a quantized vortex in boson systems. *Nuovo Cimento 20 454*, 1961.

[43] L. P. Pitaevskii. Vortex Lines in an Imperfect Bose Gas. *Sov. Phys. JETP 13 451*, 1961.

[44] S. Tomonaga. Remarks on Bloch's Method of Sound Waves applied to Many-Fermion Problems. *Prog. Theor. Phys 5, 544*, 1950.

[45] J. M. Luttinger. An Exactly Soluble Model of a ManyFermion System. *J. Math. Phys 4, 1154*, 1963.

[46] F. D. M. Haldane. 'Luttinger Liquid Theory' of one-dimensional quantum fluids: I. Properties of the Luttinger model and their extension to the general 1D interacting spinless Fermi gas. *J. Phys. C 14*, pages 2585–2609, 1981.

[47] L. Pitaevskii and S. Stringari. *Bose-Einstein Condensation*. Oxford University Press, New York 2003.

[48] C. Menotti and S. Stringari. Collective oscillations of a one-dimensional trapped Bose-Einstein gas. *Phys. Rev. A 66, 043610*, 2002.

[49] V. Dunjko, V. Lorent and M. Olshanii. Bosons in Cigar-Shaped Traps: Thomas-Fermi Regime, Tonks-Girardeau Regime, and In Between. *Phys. Rev, Lett 86, 5413*, 2001.

[50] C. N. Yang. Concept of Off-Diagonal Long-Range Order and the Quantuma Phases of Liquid He and of Superconductors. *Rev. Mod. Phys. 34, 694*, 1962.

[51] N. D. Mermin and H. Wagner. ABSENCE OF FERROMAGNETISM OR ANTIFERROMAGNETISM IN ONE- OR TWO-DIMENSIONAL ISOTROPIC HEISENBERG MODELS. *Phys. Rev. Lett 17, 1133*, 1966.

[52] P. C. Hohenberg. Existence of Long-Range Order in One and Two Dimensions. *Phys. Rev 158, 383*, 1967.

[53] L. P. Pitaevskii and S. Stringari. Uncertainty Principle, Quantum Fluctuations, and Broken Symmetries. *J. Low Temp. Phys 85, 377*, 1991.

[54] P. J. Forrester et al. Finite one-dimensional impenetrable Bose systems: Occupation numbers. *Phys. Rev. A 67, 043607*, 2003.

[55] M. Khodas, A. Kamenev and L. I. Glazman. Photosolitonic effect. *Phys. Rev. A 78, 053630*, 2008.

[56] A. Lenard. Momentum Distribution in the Ground State of the One-Dimensional System of Impenetrable Bosons. *J. Math. Phys. 5, 930*, 1964.

[57] H. G. Vaidya and C. A. Tracy. One-Particle Reduced Density Matrix of Impenetrable Bosons in One Dimension at Zero Temperature. *Phys. Rev. Lett. 42, 3*, 1979.

[58] T. Papenbrock. Ground-state properties of hard-core bosons in one-dimensional harmonic traps. *Phys. Rev. A 67, 041601*, 2003.

[59] A. Minguzzi, P. Vignolo and M. P. Tosi. High-momentum tail in the Tonks gas under harmonic confinement. *Phys. Lett. A 294, 222*, 2002.

[60] I. Bloch, J. Dalibard and W. Zwerger. Many-body physics with ultracold atoms. *Rev. Mod. Phys 80, 885*, 2008.

[61] R. Folman et al. Controlling Cold Atoms using Nanofabricated Surfaces: Atom Chips. *Phys. Rev. Lett 84, 4749*, 2000.

[62] J. Esteve et al. Observations of Density Fluctuations in an Elongated Bose Gas: Ideal Gas and Quasicondensate Regimes. *Phys. Rev. Lett 96, 130403*, 2006.

[63] M. H. Anderson et al. Observation of Bose-Einstein Condensation in a Dilute Atomic Vapor. *Science 269, 198*, 1995.

[64] K. B. Davis et al. Bose-Einstein Condensation in a Gas of Sodium Atoms. *Phys. Rev. Lett 75, 3969*, 1995.

[65] W. Ketterle, D. S. Durfee and D. M. Stamper-Kurn. Making, probing and understanding Bose-Einstein condensates. *Proceedings of the International School of Physics Enrico Fermi, Course CXL, edited by M. Inguscio, S. Stringari and C.E. Wieman (IOS Press, Amsterdam, 1999) pp. 67-176.*, 1999.

[66] J. A. Sauer, M. D. Barrett and M. S. Chapman. Storage Ring for Neutral Atoms. *Phys. Rev. Lett 87, 270401*, 2001.

[67] A. S. Arnold, C. S. Garvie and E. Riis. Large magnetic storage ring for Bose-Einstein condensates. *Phys. Rev. A 73, 041606*, 2006.

[68] O. Morizot et al. Ring trap for ultracold atoms. *Phys. Rev. A 74, 023617*, 2006.

[69] C. Ryu et al. Observation of Persistent Flow of a Bose-Einstein Condensate in a Toroidal Trap. *Phys. Rev, Lett 99, 260401*, 2007.

[70] K. Henderson et al. Experimental demonstration of painting arbitrary and dynamic potentials for Bose-Einstein condensates. *New J. Phys. 11, 043030*, 2009.

[71] R.P. Feynman. Chapter II Application of Quantum Mechanics to Liquid Helium. *Prog. Low Temp. Phys. 1, 17*, 1955.

[72] A. Nunnenkamp, A. M. Rey and K. Burnett. Generation of macroscopic superposition states in ring superlattices. *Phys. Rev. A 77, 023622*, 2008.

[73] J. R. Grover . Shell-Model Calculations of the Lowest-Energy Nuclear Excited States of Very High Angular Momentum. *Phys. Rev. 157, 832*, 1967.

[74] G. F. Bertsch and T. Papenbrock. Yrast Line for Weakly Interacting Trapped Bosons. *Phys. Rev. Lett 83, 5412*, 1999.

[75] C. W. Helstrom. *Quantum Detection and Estimations Theory*. Academic Press, New York 1976.

[76] G. Ferrini, D. Spehner, A. Minguzzi and F. W. J. Hekking. Effect of phase noise on quantum correlations in Bose-Josephson junctions. *Phys. Rev. A 84 043628*, 2011.

[77] G. B. Hess and W. M. Fairbank. Measurements of Angular Momentum in Superfluid Helium. *Phys. Rev. Lett. 19 216*, 1967.

[78] A. J. Leggett. Bose-Einstein condensation in the alkali gases: Some fundamental concepts. *Rev. Mod. Phys. 73 307*, 2001.

[79] C. Raman et al. Evidence for a Critical Velocity in a Bose-Einstein Condensed Gas. *Phys. Rev. Lett. 83 2502*, 1999.

[80] W. Schottky. Transport in a One-Channel Luttinger liquid. *Phys. Rev. Lett. 68 1220*, 1992.

[81] A. Schmid. Diffusion and Localization in a Dissipative Quantum System. *Phys. Rev. Lett. 51 1506*, 1983.

[82] Yu. Kagan, N. V. Prokof'ev and B. V. Svistunov. Drag Force on an Impurity below the Superfluid Critical Velocity in a Quasi-On-Dimensional Bose-Einstein Condensate. *Phys. Rev. Lett. 103 085302*, 2009.

[83] J. Brand and A. Y. Cherny. Dynamic structure factor of the one-dimensional Bose gas near the Tonks-Girardeau limit. *Phys. Rev. A 72 033619*, 2005.

[84] A. Y. Cherny and J. Brand. Polarizability and dynamic structure factor of the one-dimensional Bose gas near the Tonks-Girardeau limit at finite temperatures. *Phys. Rev. A 73 023612*, 2006.

[85] A. Y. Cherny and J. Brand. Dynamic and static density-density correlations in the one-dimensional Bose gas: Exact results and approximations. *Phys. Rev. A 79 043607*, 2009.

[86] A. Y. Cherny, J-S. Caux and J. Brand. Decay of superfluid currents in the interacting one-dimensional Bose gas. *Phys. Rev. A 80 043604*, 2009.

[87] A. Y. Cherny, J-S. Caux and J. Brand. Drag Force and Hess-Fairbank Effect in the One-Dimensional Bose Gas. *J. Sib. Fed. Univ. Math. Phys. 3 289*, 2011.

[88] L. Fallani et al. Observation of Dynamical Instability for a Bose-Einstein Condensate in a Moving 1D Optical Lattice. *Phys. Rev. Lett. 93 140406*, 2004.

[89] H. Hellmann. *Einfhrung in die Quantenchemie*. Franz Deuticke, Leipzig 1937.

[90] R. P. Feynman. Forces in Molecules. *Phys. Rev. 56 340*, 1939.

[91] A. Y. Cherny, J-S. Caux and J. Brand. Theory of superfluidity and drag force in the one-dimensional Bose gas. *arXiv:1106.6329v1*, 2011.

[92] Ya. M. Blanter and M. Büttiker. SHOT NOISE IN MESOSCOPIC CONDUCTORS. *Phys. Rep. 336 1*, 2000.

[93] http://de.wikipedia.org/wiki/Mach-Zehnder-Interferometer.

[94] W. Schottky. Über spontane Stromschwankungen in verschiedenen Elektrizitätsleitern. *Ann. d. Phys. 57, 541*, 1918.

[95] V. Giovannetti, S. Lloyd and L. Maccone. Quantum-Enhanced Measurements: Beating the Standard Quantum Limit. *Science 306 1330*, 2004.

[96] C. Gross et al. Nonlinear atom interferometer surpasses classical precision limit. *Nature 464 1165*, 2010.

[97] M. F. Riedel et al. Atom-chip-based generation of entanglement for quantum metrology. *Nature 464 1170*, 2010.

[98] A. S. Lane, S. L. Braunstein and C. M. Caves. Maximum-likelihood statistics of multiple quantum phase measurements. *Phys. Rev. A 47, 1667*, 1993.

[99] E. Brion, K. Moelmer and M. Saffman. Quantum Computing with Collective Ensembles of Multilevel Systems. *Phys. Rev. Lett. 99 260501*, 2007.

[100] J. E. Mooij et al. josephson Persistent-Current Qubit. *Science 285 1036*, 1999.

[101] J. R. Friedman et al. Quantum superposition of distinct macroscopic states. *Nature 406 43*, 2000.

[102] R. H. Dicke. Coherence in Spontaneous Radiation Processes. *Phys. Rev. 93, 99*, 1954.

[103] T. Monz et al. 14-Qubit Entanglement: Creation and Coherence. *Phys. Rev. Lett. 106, 130506*, 2011.

[104] A. Micheli et al. Many-particle entanglement in two-component Bose-Einstein condensates. *Phys. Rev. A 67 013607*, 2003.

[105] F. Piazza, L. Pezzé and A. Smerzi. Macroscopic superpositions of phase states with Bose-Einstein condenstates. *Phys. Rev. A 78 051601*, 2008.

[106] G. Ferrini, A. Minguzzi and F. W. J. Hekking. Number squeezing, quantum fluctuations, and oscillations in mesoscopic Bose Josephson junctions. *Phys. Rev. A 78 023606*, 2008.

[107] D. W. Hallwood, K. Burnett and J. A. Dunningham. Macroscopic superpositions of superfluid flows. *New J. Phys. 8, 180*, 2006.

[108] D. Solenov and D. Mozyrsky. Metastable States and Macroscopic Quantum Tunneling in a Cold-Atom Josephson Ring. *Phys. Rev. Lett. 104 150405*, 2010.

[109] D. Solenov and D. Mozyrsky. Macroscopic two-state systems in trapped atomic condensates. *Phys. Rev. A 82 061601*, 2010.

[110] D. M. Gangardt and G. V. Shlyapnikov. Stability and Phase Coherence of Trapped 1D Bose Gases. *Phys. Rev. Lett. 90, 010401*, 2003.

[111] J. J. Cooper, D. W. Hallwood and J. A. Dunningham. Entanglement-enhanced atomic gyroscope. *Phys. Rev. A 81, 043624*, 2010.

[112] R. Pezer and H. Buljan. Momentum Distribution Dynamics of a Tonks-Girardeau Gas: Bragg Reflections of a Quantum Many-Body Wave Packet. *Phys. Rev. Lett. 98 240403*, 2007.

[113] H. Buljan et al. Single-particle density matrix and momentum distribution of dark 'solitons' in a Tonks-Girardeau gas. *Phys. Rev. A 76 043609*, 2007.

[114] E. Wigner. On the Quantum Correction For Thermodynamic Equilibrium. *Phys. Rev. 40 749*, 1932.

[115] H. Weyl. Quantenmechanik und Gruppentheorie. *Z. Phys. 46 1*, 1927.

[116] C-W. Lee and H. Jeong. Quantification of Macroscopic Quantum Superpositions within Phase Space. *Phys. Rev. Lett. 106 220401*, 2011.